# Modeling the Future Space Debris Population and Orbital Capacity

by

## Daniel Jang

B.S. Electrical Engineering, Massachusetts Institute of Technology (2010)
M.Eng Electrical Engineering and Computer Science, Massachusetts Institute of
Technology, (2012)

Submitted to the Department of Aeronautics and Astronautics
in partial fulfillment of the requirements for the degree of

Doctor of Philosophy in Aeronautics and Astronautics

at the

MASSACHUSETTS INSTITUTE OF TECHNOLOGY

April 2024

Authored by: Daniel Jang
                     Departmnent of Aeronautics and Astronautics, April 01, 2024
Certified by: Richard Linares
                     Associate Professor of Aeronautics and Astronautics
                     Thesis Supervisor
Certified by: Olivier L. de Weck
                     Professor of Aeronautics and Astronautics
                     Thesis Committee Member
Certified by: Daniel E. Hastings
                     Professor of Aeronautics and Astronautics
                     Thesis Committee Member
Certified by: John-Scott Smokelin
                     Technical staff, MIT Lincoln Laboratory
                     Thesis Committee Member
Certified by: Zachary Folcik
                     Technical staff, MIT Lincoln Laboratory
                     Thesis Committee Member
Accepted by: Jonathan P. How
                     R. C. Maclaurin Professor of Aeronautics and Astronautics
                     Chair, Graduate Program Committee

# Modeling the Future Space Debris Population and Orbital Capacity

by

Daniel Jang

## Abstract

Increased investments and technological advances in satellite manufacturing and launch services have led to a newly vitalized Low Earth Orbit (LEO) environment. Megaconstellations consisting of hundreds to hundreds of thousands of satellites have been proposed, with SpaceX's Starlink satellite constellation now reaching more than 5400 operational satellites. This denser LEO environment underscores the urgent need for models to predict and manage the risk of collisions and the sustainable use of space. Many models have been proposed over the years to quantify the risk of collisions between resident space objects, including the seminal paper by Kessler that described the runaway conditions for which LEO could become unusable.

In this thesis, the development of the MIT Orbital Capacity Analysis Tool (MOCAT) is described along with conclusions and insights. MOCAT is a novel open-source approach to evaluating the LEO environment and comprises of a Source Sink Evolutionary Model (SSEM) and a Monte Carlo (MC) method. The SSEM simplifies the complex dynamics of space-object interactions into deterministic equations, focusing on the long-term evolution of orbital populations across different altitude shells. The simplified nature of the SSEM allows for computational efficiency, which enables optimization routines such as the exploration of equilibrium solutions for LEO carrying capacity. The improvements to the SSEM in this work through binning in the physical dimension as well as inclusion of Delta-V dynamics from the collision dynamics increases the fidelity of the SSEM.

In comparison, MOCAT-MC offers a comprehensive means to simulate the individual interactions between RSOs. The MOCAT-MC tool propagates the orbits of low-earth orbit objects and models their interactions including collisions and explosions, and provides insights into the evolving trends of the LEO population. Of particular note is the computational efficiency of the model, which is essential for managing the complexities inherent in orbital dynamics and the potential large number of objects centuries into the future. Validation results and a range of simulations, including no-future launch scenarios and the launch of proposed megaconstellations totaling more than 80,000 active payloads are explored, resulting in millions of trackable objects. Despite the much fewer megaconstellations planned at the higher altitudes, even a small fraction of failures in post-mission disposal or collision avoidance maneuvers result in an outsized effect on orbital debris accumulation. MOCAT-MC is able to simulate Lethal Non-Trackable (LNT) objects, which comprise the vast majority of the orbital population today. These lethal non-trackable object population will only grow as more payloads and debris are launched into orbit and increase the collision rate. The effect of these objects are modeled and discussed.

These two models offer different approaches to modeling the future orbital environment each with its strengths and weaknesses. Validation against existing models in literature shows the utility of MOCAT in informing future space traffic management and constellation design. The MOCAT tool has been created such that researchers can use a common model that is validated, robust, and efficient, allowing for advancement in our ability to forecast and mitigate the risks associated with the increasing density of LEO while advocating for a more sustainable approach to space exploration and utilization.

# Acknowledgments

I've been fortunate to be part of the MIT community for over a decade. I still remember visiting MIT's Campus Preview Weekend where I got to taste a little bit of the unique atmosphere and vibe. I did not realize then that I would finish multiple degrees here, be part of some amazing communities, get married on campus and learn to become a better and more capable person here. I thank God for allowing me this opportunity and for his unfailing love and encouragement. *Give thanks to the Lord, for He is good. His love endures forever.* - Psalm 136:1

I would also not have been able to complete this work without the care and support of my family. I thank my parents whose support has been such a constant force and always pushing me to be the best version of myself. My wife Grace, who has sacrificed so much and supported me with endless love. Your wisdom, love, and care have already sustained me so much, and I am so blessed to be able to build our lives together. Thank you to my brother Sam and his family Minjun, Ian, and Ethan for their constant support and curiosity. I thank the thesis committee for their guidance and encouragement throughout my research. My advisor Professor Richard Linares has been so gracious, patient, and inspiring - your insight and enthusiasm into so many of the open problems have encouraged me to keep pushing. Professor Dan Hastings, you have truly cultivated this department into a place where iron sharpens iron, and your presence and smile have been such a staple in my graduate education. Professor Oli de Weck, your enthusiasm for reaching out to the students and being the bridge between so many people and fields has been such an encouragement. Thank you to my thesis readers Dr. John-Scott Smokelin and Zach Folcik - your encouragement during my thesis journey and on-point comments have been immensely helpful.

I thank the ARCLab members for all their brilliance and kindness. Prof. Linares, you have truly brought together an exceptional group of people in your lab and I'm thankful for allowing me to be part of it. The post-doctoral researchers, research scientists and visiting professors at ARCLab have had an immense impact in shaping the lab culture and on me. David Gondelach, David Arnas, Bryce Doerr, Peng Mun Siew, Andrea D'Ambrosio, Pablo Machuca, Giovanni Lavezzi and Di Wu - you all have not only shown your brilliance and expertise but also just how kind and willing to teach you are and help at a moments notice. Thank you for always being willing to be available and to guide us with such enthusiasm. Thomas - you have injected so much life into everyone around you; your thoughtfulness in our lab and to our students at Simmons Hall always put a smile on my face and challenged me to do better personally and professionally. Miles - your expertise and passion for understanding and influencing sound policy for space management is seriously contagious, and I am so glad I got to work along side of you and absorb some of that capacity for highly impactful work. Adriana - thank you for your constant bright energy and for caring for every person in our group. Thank you Daniel Miller for all the fun conversations and lessons/lamentations over good and bad research topics at all hours of the day and sharing your honest take in all things. Axel - you've shown me what it means to pursue your heart and make things happen. Michael Luu - you've cared for so many folks around you from undergrads to the veteran community at MIT and I am fortunate to have learned about

so many things from cars to board games to the defense industry and upcoming fusion revolution. A special thank you to Corrine and Marilyn for keeping our lab running smoothly at all times. Fran, Robin, Pam, and Erinn thank you for keeping our department running so well and willing to put out fires as they seemed to pop up regularly. I thank all my supportive colleagues in Group 95 at Lincoln Laboratory and all of the mentors at the lab who have watched my work with enthusiasm.

There are many more truly wonderful people in my life I'd like to thank, but the margin is not large enough to contain. I pray that I can give back as much as you have given me.

# Contents

# List of Figures

# List of Tables

# Nomenclature

**Acronyms**

AMR    Area to Mass Ratio

CARA   Conjunction Assessment Risk Analysis

ECI     Earth Centered Inertial Coordinate System

ESA     European Space Agency

FCC     Federal Communications Commission

GEO    Geosynchronous Orbit

ISS     International Space Station

ITU     International Telecommunication Union

LEO    Low Earth Orbit (LEO)

LNT    Lethal Non-Trackable

MASTER   ESA's Meteoroid And Space debris Terrestrial Environment Reference

MC      Monte Carlo

MOCAT   MIT Orbital Capacity Analysis Tool

NASA   National Aeronautics and Space Administration

RSO    Resident Space Objects

SGP4   Simplified General Perturbations Satellite Orbit Model 4

SSEM   Source Sink Evolutionary Model

TLE     Two-Line Element

**Variables**

$\alpha$         Collision avoidance failure rate between active and non-active objects

$\alpha_a$        Collision avoidance failure rate between active objects

$\Delta t$        Simulation time step

$\Omega$         Right Ascension of the Ascending Node (RAAN)

$\omega$         Argument of Perigee

$\rho$         Atmospheric density

$\sigma$         Cross sectional area between collision objects

$\sigma$         Cross sectional area

$\tilde{E}_p$        Specific energy in a collision

$A$         Area

$a$         Semi-major axis

$A_p$        Geomagnetic planetary index

$B^*$        $B^*$ or Bstar parameter

$C_d$        Drag coefficient

$dU$        Inverse of the volume of cube

$e$         Orbit eccentricity

$f$         True Anomaly

$i$         Inclination

$J_2$        Earth's oblateness

$L_C$        Characteristic length

$M$        Mean anomaly

$m$        Mass

$P_C$        Probability of collision

$P_{PMD}$     Probability of succesful PMD

$r$         Radius of object

18

$R_E$    Earth radius

$r_{x,y,z}$    ECI position vector

$s_i$    Spatial density of objects of type $i$

$t$    Time

$v_c$    Collision velocity

$v_{x,y,z}$    ECI velocity vector

T    Temperature

# Chapter 1

# Introduction

Since the dawn of the Space Age in 1957, the number of space objects residing in space has increased exponentially. Especially in the last decade, there has been an abrupt increase in space activity also due to the increasing presence of the private companies. This general growth of space economy has led to the overcrowding of specific orbital regions around the Earth, such as the Low Earth Orbit (LEO) region, intensified by the presence of a considerable number of space debris.

Several challenges, first and foremost the increasing density of objects in orbit, is threatening the ability of space activities of benefit of Earth and its people. Some experts predict the population will reach a level at which it becomes self-sustaining, the so-called "Kessler syndrome" [60], where collisions would continue to increase the amount of debris in orbit, even without any new launches. The orbital environment around Earth is a limited resource just as the Earth's non-renewable resources. Various guidelines and policies to minimize the creation of debris have been developed within and between governments.

Over the years, with the purpose of assessing the criticality of individual objects with respect to their contribution to the space debris environment, several formulations of space debris indices have been developed. They are defined in such a way as to start from the knowledge of high-level information about the space object, such as its mass and the orbital parameters, in order to evaluate their potential detrimental effects on the debris environment over both the short-term and the long-term. The space debris indices could be used to scale the requirements for a mission such that a certain environment criticality is not achieved. However, this is not sufficient to control the overall environmental effect.

## 1.1   Motivation

The topic of sustainability of limited resources has been a topic of importance, though viewing the space environment as a limited resource and research into this has been relatively recent. As the recent investments and technological advances in satellite manufacturing and launch services have ushered in a newly vitalized Low Earth Orbit (LEO) environment, the need for a better understanding of this resource is paramount.

Megaconstellations consisting of hundreds to hundreds of thousands of satellites have been proposed, with SpaceX's Starlink satellite reaching more than 5000 satellites launched since 2018.

The resident space objects (RSO) orbiting the Earth consist of not only active payload but also debris objects. These objects consist of derelict satellites that are intact but uncontrollable and often incommunicable payloads, rocket bodies that are spent stages of a launch vehicle, and other smaller debris that may come from the launch process or from fragmentation events. With the increased launch cadence and more satellites and masses put up into LEO, the debris population has grown significantly in the recent years.

With the increased number of LEO objects so does the collision risk. Uncontrollable derelict satellites and debris objects force active satellites to maneuver to avoid conjunction. When such measures fail, collisions, such as the Iridium-Cosmos collision in 2009, can occur with higher frequency, causing more debris pieces, many of which are too small to be tracked by space surveillance sensors. It is critical to reduce the number of uncontrolled objects in LEO to avoid saturating the sensor capacity and to reduce orbital conjunction risk; however, many obstacles exist. The new space age has brought with it a congested LEO, where new commercial and government mega constellations are being proposed at a faster rate that require strict management of the orbital architecture along with deorbiting measures to remove payloads that are past their lifetimes. ASAT tests such as the destruction of Cosmos-1408 in 2021 produced thousands of debris pieces and led the crew of the International Space Station to take emergency measures due to the risk of collision with an approaching debris cloud. Around 300 on-orbit fragmentation events have occurred to date, many of them from natural conjunction between orbiting objects. In the year 2021 alone, there have been several fragmentation events, which are organized in Table 1.1 with data from DISCOSweb [62]. The November 18 and 26 fragmentation events occurred soon after the ASAT test on November 15, allowing for some possibility that a chain collision event took place. This also shows the difficulty in confirming collisions after the fact, and understanding the source of such objects.

| Date | Object Name | Altitude | Event Type | SATNO | Int. designator |
|------|-------------|----------|------------|-------|-----------------|
| 3/10 | NOAA 17 | 800 km | Battery | 27453 | 2022-032A |
| 3/18 | Yunhai 1-02 | 780 km | Collision | 44547 | 2019-063A |
| 10/24 | Cosmos-2499 | 1300 km | Unknown | 39765 | 2014-028E |
| 11/15 | Cosmos-1408 | 480 km | ASAT | 13552 | 1982-092A |
| 11/18 | Orbcomm FM05 | 760 km | Unknown | 25114 | 1997-084F |
| 11/26 | ORION 38 (Pegasus XL) | 570 km | Unknown | 45877 | 2020-046E |

Table 1.1: LEO fragmentation events in 2021 as reported on DISCOSweb

A runaway phenomenon of collisions that create debris that cause more collisions to a point where the space environment is no longer usable for payloads was first described in the seminal paper [2]. The Department of Defense originally performed the tracking and conjunction assessment of space objects with data from the Space Surveillance Network for Space Situational Awareness (SSA). Since 2005, the NASA Conjunction

| Name | Int. designator | Breakup epoch | Fragments |
|---|---|---|---|
| Fengyun 1C | 1999-025A | 11 Jan 2007 | 3431 |
| Cosmos-2251 | 1993-036A | 10 Feb 2009 | 1667 |
| HAPS | 1994-029B | 03 Jun 1996 | 753 |
| Iridium 33 | 1997-051C | 10 Feb 2009 | 627 |
| Cosmos-2421 | 2006-026A | 14 Mar 2008 | 509 |
| H8 | 1986-019C | 13 Nov 1986 | 497 |
| Cosmos-1275 | 1981-053A | 24 Jul 1981 | 478 |
| Titan Transtage | 0-000None | 15 Oct 1965 | 473 |
| NOAA 16 | 2000-055A | 25 Nov 2015 | 458 |
| Centaur-5 SEC | 2014-055B | 30 Aug 2018 | 455 |

Table 1.2: Top 10 fragmentation events by number of fragments

Assessment Risk Analysis (CARA) program has been performing routine on-orbit satellite conjunction risk analysis.

Another challenge to the space-debris problem is the existence of lethal non-trackable (LNT) objects. Several organizations and institutions around the world track objects in orbit, focusing primarily on larger objects such as satellites and space debris. Tracking resident space objects (RSOs) in orbit typically involves using a combination of ground-based radar systems and optical telescopes. Radar systems can provide precise measurements of an object's position, velocity, and trajectory by detecting the radar signals reflected off the object. Optical telescopes, on the other hand, rely on capturing light reflected by the object to track its position. Advancements in technology have enabled better tracking capabilities. Radar systems have improved in sensitivity and resolution, allowing the detection and tracking of smaller objects. Optical telescopes have also benefited from more advanced imaging techniques and larger telescope sizes, aiding in the detection of faint objects.

Additionally, organizations such as the U.S. Space Surveillance Network (SSN) and other international space agencies work toward cataloging and monitoring objects in space. They maintain extensive databases that contain information on known objects in orbit, including their orbital parameters and characteristics. These databases help track and predict the movements of objects in space, helping to avoid collisions with operational satellites.

Although there have been considerable improvements in technology to support searching and tracking of orbital objects, tracking small objects remains a challenging task. Tracking smaller objects, such as fragments or debris that measure a few centimeters or less, remains difficult because of their size and limited reflectivity in the visible spectrum as well as radar frequencies.

From in situ measurements and terrestrial testing of orbital collision dynamics, it is understood that every collision event causes fragments that can be vanishingly small even down to the micrometer level.

There has been a greater understanding that the space environment is a common good and that all stakeholders have a vested interest in mitigating the space debris problem. Commercial companies of mega-constellations such as SpaceX and OneWeb have incorporated debris mitigation strategies such as launching

a batch of payloads into a lower launch, whereby the individual payloads would perform checkout then raise their orbits to insert into the final operational orbit. The derelict satellites will then decay much faster than had they initially been placed in the higher operational orbit. Such a traffic pattern is something unique to the megaconstellations, and the steady-state traffic pattern due to these maneuvering satellites will need to be modeled along with the associated risks due to the increased volume that is traversing through multiple altitude regimes.

Space debris has emerged as a critical environmental and political issue because of the substantial increase in objects orbiting Earth, especially in the Low Earth Orbit (LEO). Several factors contribute to this recent increase in the number of objects, including cost-efficient launches, increased commercial activity, and many debris-creating events in space, such as explosions and collisions, including antisatellite weapon tests. In particular, recent advances in orbital launch technologies and growth of the commercial launch providers have made launches to LEO much cheaper and more reliable leading to a new space age. Until recently, the increase in object number in space was around 300 objects per year; however, increased launch cadence and the rise of large LEO constellations (LLC) has led to a marked increase in LEO population. For example, from 2019 to 2023, SpaceX alone has launched more than 5,500 satellites. The US Federal Communications Commission (FCC) and the United Nation International Telecommunication Union (ITU) filings show that companies or governments are getting approvals for constellations that are greater than the current number of objects in space. Although now defunct, in 2021 the government of Rwanda filed with the ITU a constellation of 327,230 satellites, and a Canadian company Aether filed for a constellation with 115,000 satellites [5, 4].

The accumulation of these operational payloads and uncontrolled debris poses a growing collision risk to operational satellites and disrupts crucial communication, weather forecasting, navigation, and scientific observation capabilities, as well as human space-flight missions. As the debris from fragmentation events create much more debris from collisions, it may be possible to create a cascading effect of chain reaction, which is a phenomenon known as the Kessler syndrome, which may render certain altitudes unusable and threaten the sustainability of space operations. The only natural sink to remove space debris from LEO is the upper atmosphere's low density; there is a limit to how many collisions can be tolerated in LEO, which is highly dependent on the orbital altitude.

Recent advances in technologies and policies addressing the space debris problem encompass several key areas. Active Debris Removal (ADR) technologies are being developed, including systems such as harpoons, nets, robotic arms, and space tugs, to capture, deorbit, or mitigate the effects of space debris [75, 88, 150, 43, 127, 23]. Several international organizations have established guidelines and standards for debris mitigation, with the aim of minimizing debris generation and improving spacecraft design. Efforts in space traffic management (STM) seek to enhance situational awareness, collision avoidance, and coordination among satellite operators [11, 86, 84]. Improved tracking and surveillance technologies have helped to monitor and catalog space debris, improving space situational awareness. International collaboration and agreements are crucial for promoting information sharing, joint research efforts, and coordinated actions on a global scale.

These technologies and policies collectively aim to mitigate space debris growth, minimize collision risks, and ensure the sustainability of space activities. Continued advances in technology, international cooperation, and regulatory frameworks are essential to effectively address the challenges posed by space debris. Multi-national studies have shown the dangers of this increased population, and policies and metrics have been proposed to counteract the increased risk in the space environment [7, 54, 131, 133, 36, 34]. Recently, debris-mitigation policies such as the '5-year rule' [37] have been enacted, and tesolutions to limit debris-causing antisatellite tests have come from the UN as well as the commercial space industry [141, 8].

Orbital environment modeling shares several similarities with environmental modeling in fields such as global warming. Complex systems with numerous interconnected variables and interactions need to be modeled and predictions must be made with the best estimate of future inputs from controllable factors such as human activity and mitigation efforts, as well as natural phenomena such as sequestration. Modeling is heavily based on data collection, analysis, and simulation. For data on space debris, numerous in-situ measurements and observational techniques have been deployed over the years. These methods include space-based sensors, laser ranging, radar observations, spacecraft inspections and retrieval missions, impact studies on spacecraft surfaces, particle detectors, and laboratory analysis of collected debris. These techniques play a vital role in understanding the characteristics, distribution, and behavior of space debris, significantly contributing to efforts aimed at mitigating risks and managing the space environment. Continuous advancements in observational technologies and missions remain critical for further improving our understanding of the space debris environment.

Ultimately, these models are often used to create sustainable policy and can have significant policy implications. Such modeling efforts and global consensus led to the Paris Accord, an international treaty developed within the United Nations Framework Convention on Climate Change to address climate change by limiting global warming to well below 2 degrees Celsius. Similarly, addressing the space debris problem will require global collaboration, responsible space practices, effective debris mitigation strategies, and the advancement of technologies for active debris removal and improved space situational awareness. Space debris models guide policies and strategies for space traffic management, debris mitigation, and spacecraft design to ensure sustainability of space activities.

### 1.1.1 Modeling the LEO environment

Ever-increasing launch-rate due to proposed LLCs pose an unprecedented increase in the risk of conjunction, as collision probability scales as $N^2$ where $N$ is the number of orbital objects. To understand the complex dynamics of space debris, multiple sophisticated modeling approaches have been developed. Kessler's paper in 1978 originally described the potential for runaway growth of orbital debris due to debris that causes more debris through collisions, which could lead to an unusable orbital environment [60]. Since then, several analytical methods have been proposed in the literature to better quantify this risk, which can be divided into a few categories. There are largely two methods to model the evolution of the LEO RSO population

and collision risk: statistical sampling methods such as Monte Carlo methods, and source-sink models, also known as particle-in-box models. There are also heuristic metrics to quantify the risk per object for any particular composition of the LEO environment.

The sensitivity analysis performed through these models evaluates the efficacy of the proposed mitigation measures. They examine the impact of debris removal strategies, spacecraft design alterations, and operational changes on reducing debris generation and collision risks. These modeling efforts serve the critical purpose of enhancing our understanding of the space debris environment, facilitating predictions of future scenarios, evaluating risks posed to space assets, and guiding policymakers in formulating effective mitigation strategies. Given the increasing concern surrounding space debris, continuous advancements in modeling techniques are imperative to develop robust strategies that mitigate its adverse effects on space operations and sustainability.

**Heuristic-based metrics**

Space agencies and organizations often use heuristic methods and metrics for decision making when planning missions or strategies to ensure space sustainability. These indexes are a metric used to assess the potential danger posed by an orbital object and help prioritize the management and mitigation of space debris by assessing the risk associated with individual debris objects. In the literature, some indexes have been proposed to quantify this risk.

The Criticality of Spacecraft Index (CSI) ranks the environmental criticality of abandoned objects in LEO [123]. It takes into account the physical characteristics of a given object, its orbit and the environment where this is located. Environmental Consequences of Orbital Breakups (ECOB) is based on the evaluation of the consequences of the fragmentation of the studied object in terms of the increase in the collision probability for operational satellites. This index considers the likelihood and consequence of fragmentation and end-of-life mitigation strategies [67].

The concept of environment capacity has been proposed as an index where the number and type of missions that are compatible with a stable evolution of the orbital environment are quantified by considering the evolution of the environment [64]. The yearly average number of fragments above an assigned size threshold expected as a result of accidental collisions.

In [108] numerous international space organizations contributed lists of the top 50 concerning objects, which were compared using multiple algorithms to create a ranked composite list. Factors such as mass, encounter rates, orbital lifetime, and proximity to operational satellites were shown to be crucial. This list aims to improve space safety and long-term sustainability by highlighting the most hazardous objects in LEO that need to be removed. Similarly, MITRI is an index to help identify the most dangerous debris that can be removed considering the requirements of the chaser spacecraft and the constraints of the mission [127]. The index considers the proximity of the debris to highly populated regions, its persistence in orbit, its likelihood to collide, and the estimated number and mass of debris it can generate.

By combining these factors, the criticality index aims to prioritize which debris objects need immediate attention for removal or mitigation strategies. Objects with a higher criticality index are typically targeted for potential remediation or collision avoidance maneuvers to reduce the risk they pose to active satellites and spacecraft.

Using the modeling technique listed above, two types of orbital capacity can be defined: *deterministic* capacity as well as *probabilistic* capacity. Deterministic capacity refers to the orbital capacity without unknown and uncontrolled objects. This is analogous to the theoretical maximum capacity of the environment, given some minimum permitted separation distance between objects. In this case, no collisions are assumed.

Probabilistic capacity refers to the opposite end of the spectrum, where collisions are modeled as a Poisson random process, and the capacity is determined with some criteria with regard to stability or number of collisions. Some examples include [140, 59, 72].

Indexing the debris environment has also been considered as a possible measure to enact policies or levy economic incentives. These range from giving some metric on the critical orbits for debris [22, 67, 56] to measuring individual RSO's contribution to the debris risk [71, 113, 123, 70, 56, 42]. Such criticality indexes can serve as a good validation for any capacity definitions and analysis of the trade-off between cumulative environmental criticality to maximum capacity. Similarly, the effect of physically repositioning key debris and its effect on the risk of orbital collisions was analyzed in [16]. The effect of the quality of SSA data on the Space Sustainability Rating has also been analyzed [73]. Many policy-level analysis on capacity building ranging from SSA data sharing to debris mitigation tech development and legal hurdles are described also in the book [98].

## Constellation design and slotting methods

Geosynchronous Earth orbit (GEO) has long been a highly coveted yet scarce real estate. Starting as a measure for spectrum management, the international community agreed in the 1960s to regulate the assignment of slots in the GEO belt through the International Telecommunications Union (ITU) such that any company or nation planning to launch a satellite to GEO must apply to the ITU for an orbital slot. The slotting mechanism for such a low-inclination and specific altitude orbit has been easy to understand and implement.

In the LEO environment, however, the RSOs span many intersecting orbits with a wide range of altitudes, inclinations, and eccentricities. The complexity of staking a particular orbit in LEO has meant that no internationally recognized governing body administers the LEO regime. This has also meant that the burden of predicting collisions between objects is much more complex and often falls on the payload owner. This has given rise to commercial Space Situational Awareness (SSA) companies that sell high-fidelity ephemeris data to the satellite owners.

Other slotting schemes for LEO has been proposed. Sun-synchronous Orbit (SSO) is a type of LEO orbit that is useful for remote sensing, and slotting architectures for those particular set of orbits has been

proposed [15, 111, 147]. Lattice Flower Constellation (LFC) theory has been applied to efficiently stack constellations for constellations with varying eccentricities and inclinations [11, 84]. The typical FCC filings for LEO often claim ±30 km orbital tolerances, although with slotting methods, a 5 km or less spacing may be possible, allowing for a denser use of LEO. Note that all slotting methods require reasonable knowledge of the spacecraft orbital state as well as controllability. These attributes will guarantee a passively-safe RSO population within the constellation.

## Source-Sink Models

Source-Sink evolutionary models describe the interactions between populations of objects with ordinary differential equations. These types of models are based upon predator-prey models, also known as Lotka–Volterra Dynamical Systems [95, 145], in which a pair of first-order nonlinear differential equations are used to describe the dynamics of biological or ecological systems. In the case of space debris, all space objects of interest could be categorized as payloads, derelict satellites, or debris, three ordinary differential equations can describe the interaction between these populations. Average values are often used to describe the population's characteristics, such as a population's size, velocity, rate of launch and failure-rate. This simplification removes the need for computationally expensive propagation of individual object states to estimate a future debris environment. Gross populations are propagated forward according to the governing differential equations, which allows for fast solutions even far into the future. The exploration of a wide set of initial conditions and parameters is much more approachable using such methods. These methods are also usually deterministic in that given a set of input variables, a consistent output can be expected as the variables interact in a formalized manner.

Kessler and Cour-Palais first described the feedback runaway phenomena and identified the risk of an exponential increase in the number of space debris, and since then, a few evolutionary models have been proposed in the literature. Talent introduces the particles-in-box (PIB) model where a population within an orbital shell is assumed to have some average characteristic and interactions. Fast Debris Evolution (FADE) used simplified first-order differential equations to describe the population interaction. JASON describes a three-population model for one shell and a given launch cadence [75]. Many models have expanded the evolutionary model to analyze multiple shells, optimal control schemes and economic equilibrium for maximum policy intake. The MIT Orbital Capacity Tool Source-Sink Evolutionary Model (MOCAT-SSEM) is able to create a flexible and modular multi-fidelity model to model the evolution of the LEO population quickly [83]. The low computational cost demonstrates the ability to optimize over user-defined cost functions for policy-making and governance, and calculate the risk-based space-environment capacity [26].

## Monte-Carlo Methods

Statistical sampling methods propagate every RSO's orbital states with high fidelity propagators to estimate the future space environment at some small time steps, much like a particle filter. This method allows accurate

near-future predictions of potential collisions and is used operationally today for conjunction avoidance. Several such sampling-based models have been developed by space agencies and private entities due to the large-scale development needed. Examples include NASA's Orbital Debris Engineering Model (ORDEM) and LEO to Geosynchronous Orbit Debris model (LEGEND)[89], European Space Agency's Orbital Debris Evolutionary Model (ODEM), Chinese Academy of Sciences' SOLEM (Space Objects Long-term Evolution Model), University of Southampton and United Kingdom Space Agency's Debris Analysis and Monitoring Architecture for the Geosynchronous Environment (DAMAGE)[76, 80], MEDEE model from Centre National d'Etudes Spatiales [30], DELTA model from European Space Agency [100], LUCA model from Technische University at Braunschweig [116], NEODEEM model from Kyushu University and the Japan Aerospace Exploration Agency, IMPACT [130], and others [146, 31, 121].

For each of these models, the debris population and densities are outputted given some input initial conditions and assumptions. Computing a debris environment with different sets of assumptions, however, requires high computational cost, as each object must be propagated. Sampling over a distribution of uncertainties on the states and parameters would require an exponential number of propagations. The high cost is due to the small time steps required to accurately model a collision and semi-analytical propagators requiring high compute cost to propagate far into the future. For each collision or fragmentation event, some breakup model such as NASA Standard Breakup Model is used to model the debris cloud generation. Although the outputted debris distribution for some assumed initial condition and future traffic model exist, all of these models are closed-source and inputting arbitrary assumptions is difficult if not impossible.

Collision detection is an essential part of modeling the future growth of debris. It can also become the most computationally taxing part of any model. To model the long-term evolution of the space environment, there is a spectrum of methods to determine whether a collision has occurred. In general, they can be divided into deterministic methods and stochastic sampling-based methods. Deterministic methods calculate the actual point of closest approach for each pair of satellites that are nearby. Adaptive propagation time steps are needed to calculate the precise moment and distance between two objects, which imposes a significantly higher computational cost, and typically the computational scaling of these PCA methods to $n$ objects would be $\mathcal{O}(n^2)$; however, methods that filter pairs of comparisons have been proposed in the literature that allow for complexity of $\mathcal{O}(n^{1.5})$ [10, 41, 96].

Though the collision and atmospheric sink dynamics as well as various orbital perturbation forces can be modeled well, propagation of tens of thousands of orbital objects and a high-dimensional parameter space make these calculations untenable for centennial scale modeling of the debris environment. For example, in [121] a set of roughly 19 million orbits was propagated for 120 years, which took an equivalent of 24 years of CPU time.

These deterministic methods are used mainly by operational groups such as the NASA Conjunction Assessment Risk Analysis (CARA) team and the 18th Space Control Squadron (18 SPCS) to perform routine on-orbit satellite conjunction assessment [44, 46, 53]. These collision probabilities are calculated for each close

encounter, and as an example, NASA CARA calculates the probability of collision ($P_c$) as

$$P_c = \frac{1}{2\pi\sqrt{C}} \iint\limits_{A} e^{-\frac{1}{2}r^T C^{-1} r} dx dz, \tag{1.1}$$

where $A$ is the cross-sectional with the defined hard body radius, $r$ is the distance between objects at the point of closest approach, and $C$ is the total covariance between the two objects.

An example of the stochastic sampling-based method is the Cube method, which has been proposed to estimate collision rates using sampling methods to reduce the computational complexity at the expense of fidelity [87]. This method has been used in numerous MC tools due to its scalability and simple implementation [92, 89], although some care is needed to tune the algorithm parameters for realistic collision probability [78]. The computational scaling of Cube to $n$ objects is $\mathcal{O}(n)$. These stochastic methods are typically used for long-term modeling that requires enough fidelity to scale with the population of the orbiting objects.

The creation of debris objects after an on-orbit collision is done through the fragmentation model. On-orbit collisions typically have very high energy content, and most historic approaches modeled the mass distribution that followed the power law, starting with [14]. The propagation of debris clouds has also been an active area of research. Nominally, a covariance propagation model may be adapted, though the log-normal distribution of the number of objects and imparted $\Delta V$ in a collision is ill-suited to the multivariate Gaussian assumption for covariances. The evolution of the debris cloud and its effect on key LEO orbits have been formulated and analyzed in [45, 24, 39]. Efficient cloud propagation has been explored using DAMAGE and other MC approaches [122, 74, 66]. The specific contribution of explosion and future collision fragments to the orbital debris environment showed the importance of mitigating fragmentation events [135, 125]. The probabilistic uncertainty of debris lifetime was analyzed in [28, 97, 77]. The effect of thomospheric contraction on debris reentry has been modeled [80]. Emperical modeling from fragmentation events such as the Iridium-Cosmos collision and the 2013 ASAT test has validated some models [149, 58, 134]. As such, many fragmentation models have existed since the early days of the Space Age, many of which are detailed in [49].

NASA's Standard Breakup Model (SBM) [55, 63] is a semiempirical model based on evidence compiled from historical orbital data and terrestrial hypervelocity tests such as the Satellite Orbital Debris Characterization Impact Test (SOCIT). With updates to the model from many tests and on-orbit data, it has become a popular choice as a fragmentation model. The model is deterministic and sample-based, and the samples are described by $L$ the characteristic length, $A/m$ the area-to-mass ratio, and $\Delta v$ the ejection velocity in a random direction from the parent velocity.

The SBM specifies that the impact energy per target mass is

$$\epsilon = \frac{1}{2}\frac{m_c}{m_t}v_c^2, \tag{1.2}$$

where $m_c$ is the mass of the chaser and $m_t$ is the mass of the target, and impact velocity is $v_c$. The mass of

the target is assumed to be greater than the mass of the chaser. A collision is considered to be *catastrophic* where the chaser and the target are completely fragmented when $\epsilon > 40$ J/g and *non-catastrophic* if not. A completely fragmented object follows the SBM in creating debris down to the given minimum $L_C$ size and follows the power-law distribution up to 1 meter size. During a noncatastrophic collision, only the smaller object completely fragments, while the mass of the larger parent object stays intact as one object. In this case, the intact parent object may lose some mass or gain some mass, depending on the closing velocity and mass of the projectile.

Although many of the long-term evolutionary models are proprietary, the Inter-Agency Space Debris Coordination Committee (IADC) routinely compares several models and has published comparisons [94, 12]. As noted, most of these models use the same assumptions, break-up models, etc. which may contribute to bias on the results, but it is also seen that even for very simple scenarios such as *No Future Launches* (NFL) or *business as usual* (BAU) the models can vary in their outputs. The randomized initial sampling of the initial distribution of Resident Space Objects (RSOs) used by these MC methods proves to be important, as seen by the fact that, for all of the models, the results span a wide range.

## 1.2 MOCAT

The establishment of a common, validated, and open-source model for space debris is imperative for several reasons. Firstly, such a model ensures standardization and consistency between stakeholders, creating a shared language and methodology for analyzing space debris. This framework facilitates effective communication and information sharing among governments, space agencies, researchers, and industry players. In addition, a validated model improves accuracy in assessing collision risks and predicting debris behavior, crucial for ensuring the safety of spacecraft, satellites, and astronauts in orbit. Policymakers benefit from this shared understanding to develop regulations and policies, foster international agreements, and make informed decisions on space activities. Furthermore, resource allocation becomes more efficient with a validated open source model, allowing stakeholders to prioritize investments in proven technologies and strategies. Collaboration and knowledge sharing are encouraged, leading to continuous improvements in space debris modeling techniques. Finally, such a model helps to raise public awareness of the challenges of space debris, educate stakeholders about responsible space activities, and garner support for relevant policies and initiatives. Ultimately, it contributes to the sustainable use of outer space and the preservation of critical space assets.

To address the challenges and needs mentioned above, the MIT Orbital Capacity Assessment Tool (MOCAT) was created, which consists of two methods: a source-sink evolutionary model (MOCAT-SSEM) and a Monte Carlo approach (MOCAT-MC). MOCAT-SSEM is a multibin multishell generalizable SSEM model that is flexible in its object definitions. MOCAT-MC is a full-scale three-dimensional debris evolutionary model which propagates individual objects and models the interactions between objects at each time step, with the aim of assessing the LEO RSO population. In this thesis the development and validation of

MOCAT-MC is described and a summary of analysis of the LEO environment in the past and future, along with improvements to MOCAT-SSEM for a higher-fidelity model. MOCAT is developed in MATLAB and is open source, available in `https://github.com/ARCLab-MIT`.

## 1.3 Thesis Contributions

This section describes the main contributions of this thesis that close the technical gap in modeling the population evolution in LEO with variable-fidelity models. This section also includes a roadmap of the chapters found in this thesis.

This thesis makes several contributions to the literature, including:

- Development of the first open-source MC-based evolutionary orbital population model

- Simulation of tens of millions of orbital objects including Lethal Non-Trackable objects centuries into the future using single processing thread

- Demonstration that analytical propagation can be used to scale MC simulations

- First analysis of future constellation traffic as filed with ITU and FCC, reaching 82,000 operational satellites in LEO from the megaconstellations alone

- Increased fidelity of the Source-Sink Evolutionary Model (SSEM) through the use of multi-binned objects

- Novel inclusion of the Delta-V dynamics to SSEM formulation allowing for shell-to-shell interactivity in debris deposition.

### 1.3.1 Thesis Organization

The research motivation, introduction and literature review are described in Chapter 1. Chapter 2 describes the MC methods for evolutionary modeling of the LEO population that exist in the literature. Gaps in the literature are identified and MOCAT-MC is described, validated, and used to analyze several future scenarios. Chapter 3 describes the inclusion of Lethal Non-Trackable objects into MOCAT-MC and the effect of LNT on future space environment modeling and space sustainability. Chapter 4 describes the SSEM models and the development of the multi-bin model and Delta-V dynamics to increase its fidelity. Chapter 5 summarizes the work and explores potential future work.

# Chapter 2

# A New Monte-Carlo model for the Space Environment and its Prediction for Planned Missions

## 2.1 Introduction to MOCAT-MC

The MIT Orbital Capacity Tool (MOCAT) consists of a Monte Carlo approach called MOCAT-MC to simulate the long-term evolution of LEO orbital objects. The development of MOCAT-MC provides an open source validated tool that can be accessed and used by the scientific community, and particular attention is given to the computational speed of all the blocks of the tool. It is a full-scale three-dimensional debris evolutionary model which propagates individual objects and models the interactions between objects at each time step, with the aim of assessing the LEO RSO population. The tool is developed in MATLAB.

One of the drawbacks of MC methods is the high computational time required to run the simulations, which prevents these software from being tested against many different scenarios in terms of initial population, launch rate, collision and explosion event occurrences, etc. Additionally, several catalogs are considered and merged to obtain the current initial population. For what concerns the main core of the MOCAT-MC, several phenomena are considered, such as the atmospheric model and the propagator fidelity, active satellite station-keeping, new launches, reentry, post-mission disposal (PMD), explosions, and collisions. In particular, the last two events are modeled via the NASA standard break-up model (SBM). Finally, the proposed MOCAT-MC is tested with different launch rate scenarios, including the *no future launches* scenario.

Though this Monte Carlo approach is computationally expensive, it is capable of modeling and tracking individual objects' orbital and interaction history. Individual objects' parameters and trajectories at each time-step are adjustable, allowing for specific orbital maneuvers or change of physical parameters for each

satellite.

A simulation consisting of many episodes is run with sampling of one or more random variables with associated probability distribution functions (PDF). The random variables to be sampled and the PDFs can vary depending on the analysis to be performed.

The MOCAT-MC simulation setup involves several critical inputs to establish the scenario. These include the choice of the propagator, scenario duration, propagation time steps, atmospheric model, and parameters for collision detection. Additionally, initialization requires defining the initial population of space objects, specifying their properties, and incorporating a launch traffic model. This initial population may involve sampling from a probability distribution function (PDF) of the debris population. Furthermore, the methodology for orbit control and the post-mission disposal rate are chosen for each type of space object.

Throughout each time step in the simulation, all objects undergo propagation, and the probability of collision is calculated for pairs of objects situated closer than a specified Cube parameter. Collision events are randomly sampled, and debris is generated based on determinations from the NASA Standard Breakup Model (SBM). The simulation also includes modeling explosions according to the SBM, with preset explosion probabilities at the beginning of the simulation.

Subsequent to the initialization phase, MOCAT-MC enters a propagation loop. At each subsequent time step several key actions are executed. Active Resident Space Objects (RSOs) actively maintain their orbital altitude to counteract the effects of atmospheric drag. New launches are introduced into the simulation, either based on predetermined launch dates and orbital profiles or sampled from a probability distribution function (PDF) representing launch rates and final orbits.

Certain RSOs are deliberately deorbited and removed from the simulation as a result of atmospheric reentry. In addition, active satellites reaching the end of their designated lifetime undergo post-misssion disposal (PMD). However, some satellites may fail to execute PMD with some probability, transitioning into an inactive state and remaining in its orbit as an derelict object.

Explosions are simulated with a predefined probability, leading to the creation of smaller debris as described by the NASA Standard Breakup Model (EVOLVE 4) [55]. The characteristics of these newly generated objects, such as quantity, direction, and size, are determined by the model. The Cube method is used to determine collisions between two objects [92, 87], and results in the generation of numerous debris objects within the simulation as dictated by the NASA SBM. Depending on several factors including closing velocity and the mass of the colliding objects, the collision is deemed to be a catastrophic collision or a noncatastrophic collision. This distinction will determine the number of debris generated as well as the profile.

To validate this new model, comparison can be done to published results from other existing Monte Carlo methods. Numerous models have been developed by space agencies and private entities, as described earlier. Although all other codebases are proprietary, an IADC study in 2013 compared several of the models in [94]. Most of these models use the same assumptions, breakup models, and other submodules, which may contribute to some bias; however, the general agreement in the final results and conclusions shows that

comparisons against other models may be a good first step in establishing validity in a new model. It is seen that even for very simple scenarios such as *No Future Launches* or *Business As Usual* the models can vary in output. The randomized initial sampling of the initial distribution of RSOs used by these MC methods proves to be important, as seen by the fact that for all of the models, the results span a wide range. Note that validation of these models against historical data is difficult, as the collision rate – which largely determines the population growth in long-term simulations – has been a very low-probability event. To date, only four accidental collisions between two orbital objects have been documented, of which only one produced more than 5 fragments [61]. Validation of these models and their predictive power will be observed as more data on on-orbit collision events are observed.

## 2.2   Methodology

MOCAT-MC has multiple submodules, which is shown in the functional diagram in Figure 2-1. The description of each of these components is described in this section. Note that MOCAT is architected so that the submodules are modular and are easily adjusted or changed to an alternative method.
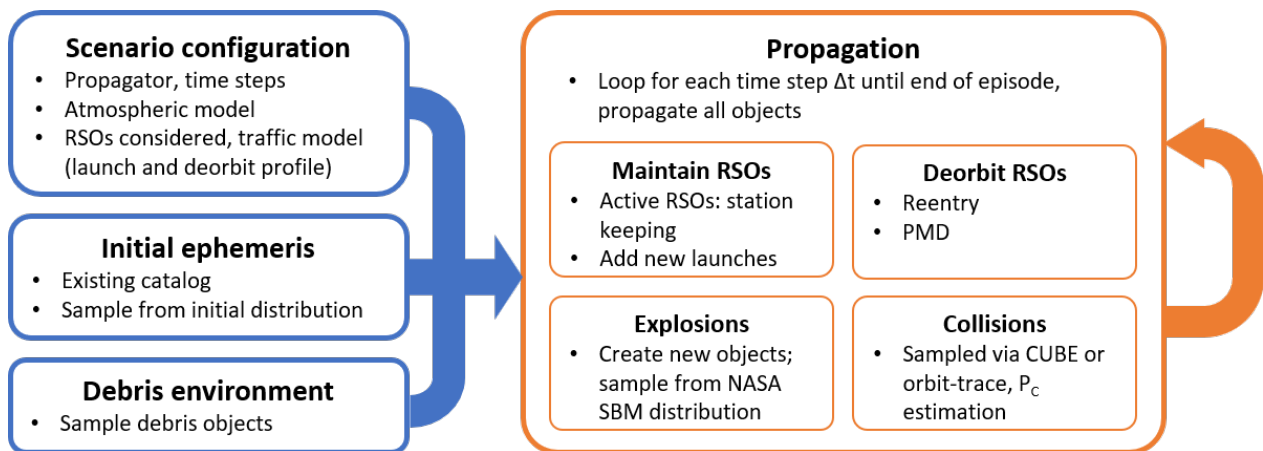


Figure 2-1: Schematic of the Monte Carlo tool MOCAT-MC

### 2.2.1   Analytical Propagator

Commonly, the SGP4 propagator is implemented to propagate the orbital motion of RSOs. However, other semianalytical and analytical propagators could represent a better choice in terms of a compromise between fidelity and computational time. Therefore, in MOCAT-MC, an analytical approximation of the solution for the motion of RSOs in LEO is used, considering the atmospheric drag and the $J_2$ perturbation. The initial ephemeris is also loaded, which can be seeded with an existing catalog such as the Two Line Element (TLE) catalog provided publicly by the 18th Space Defense Squadron.

In MOCAT-MC, a time-explicit analytic approximate solution for the motion of low-Earth orbiting satel-

lites is used. The main perturbations that act on space objects in LEO are the oblateness of the planet and the presence of atmospheric drag. An averaging perturbation technique has been employed to obtain the variational equations for the orbital elements with the combined effect of $J_2$ and drag as described in [101]. Implementation of other propagators such as the Draper Semi-analytical Satellite Theory (DSST) [21] and SGP4 [142] is reserved for future work, though these will require a higher computational burden compared to the analytical propagator. The propagator is based on two assumptions: the atmospheric density is constant and the orbit eccentricity is small. However, in the implementation of the analytical propagator, a time-varying atmospheric model is modeled with a piecewise continuous formulation with a mean solar activity [143] rather than a static atmospheric density. This allows for effects of geomagnetic storms and solar cycles to be modeled, which can strongly affect the atmospheric density.

Let us define

$$\alpha_0 = \frac{\bar{e}_0}{\sqrt{\bar{a}_0}} \ , \qquad\qquad \beta_0 = \frac{\sqrt{3}}{2}\,\bar{e}_0, \qquad\qquad \bar{n}_0 = \sqrt{\frac{\mu}{\bar{a}_0^3}}; \qquad\qquad (2.1)$$

and indicate with $c = \cos\bar{i}$ the cosine of the inclination. The resulting set of equations used for the propagation is

$$\bar{a} = \frac{\bar{a}_0}{\beta_0^2}\tan^2\left[\arctan(\beta_0) - \beta_0\bar{n}_0\bar{a}_0 C_0(t - t_0)\right]$$

$$\bar{e} = \frac{2}{\sqrt{3}}\tan\left[\arctan(\beta_0) - \beta_0\bar{n}_0\bar{a}_0 C_0(t - t_0)\right]$$

$$\bar{M} - \bar{M}_0 = \frac{1}{8}\frac{1}{C_0}\left[\frac{4}{\tau} + 3\alpha_0^2\ln\left(\frac{\tau}{\bar{a}_0}\right)\right]\Bigg|_{\tau=\bar{a}_0}^{\tau=\bar{a}} + \frac{3k_2\left(3c^2 - 1\right)}{16\mu}\frac{1}{C_0}\left[\frac{3\alpha_0^2}{2}\frac{1}{\tau^2} + \frac{4}{3\tau^3}\right]\Bigg|_{\tau=\bar{a}_0}^{\tau=\bar{a}} \qquad (2.2)$$

$$\bar{\omega} - \bar{\omega}_0 = \frac{3k_2\left(5c^2 - 1\right)}{16\mu}\frac{1}{C_0}\left[\frac{5\alpha_0^2}{2}\frac{1}{\tau^2} + \frac{4}{3\tau^3}\right]\Bigg|_{\tau=\bar{a}_0}^{\tau=\bar{a}}$$

$$\bar{\Omega} - \bar{\Omega}_0 = -\frac{3k_2 c}{8\mu}\frac{1}{C_0}\left[\frac{5\alpha_0^2}{2}\frac{1}{\tau^2} + \frac{4}{3\tau^3}\right]\Bigg|_{\tau=\bar{a}_0}^{\tau=\bar{a}}$$

where $[\bar{a}, \bar{e}, \bar{i}, \bar{\Omega}, \bar{\omega}, \bar{M}]^T$ represents the state vector at the current time $t$: semi-major axis, eccentricity, inclination, right ascension of the ascending node, argument of periapsis, and mean anomaly, respectively. The subscript 0 denotes state variables at the initial time of propagation $t_0$, and $k_2 = \mu J_2 R_E^2/2$ and $C_0 = \frac{1}{2}C_d\frac{A}{m}\rho_0$, with $\mu$ and $R_E$ representing the gravitational parameter and radius of the Earth, respectively, $\rho$ the atmospheric density, and $C_d$, $A$, and $m$ representing the drag coefficient, area, and mass, respectively.

A static exponential atmospheric model is used to test the validity of the analytical equations of motion in Eq. (2.2) compared to a numerical propagator that includes drag and $J_2$ effects. For a given initial population of objects between 200 and 2,000 km altitudes and a one-year propagation time, several relevant metrics are used for validation purposes: number of objects still in orbit depending on initial altitude $h_0$; reduction in the semi-major axis depending on $h_0$ and decay in right ascension depending on $h_0$; and finally the time to

decay depending on $h_0$. Figures 2-2 to 2-5 show the validation results.

Figure 2-2, for instance, illustrates the number of objects as a function of altitude, in the initial population and after the one-year propagation. It can be observed that the distributions of objects obtained by the analytical propagator and by the numerical propagator show strong agreement. The analytical propagator can effectively approximate the number of objects expected as a function of altitude. From Figure 2-3, it is shown that the analytical propagator typically underestimates the decay in the semi-major axis due to drag, but the overall distribution of semi-major decay as a function of altitude resembles that of the numerical propagator. On the contrary, in Figure 2-4, it is observed that the decrease in right ascension is usually overestimated by the analytical propagator, but the overall distribution of the decrease in right ascension as a function of altitude is also similar to that displayed by the numerical propagator. Lastly, and related to the results in Figure 2-3, it is observed in Figure 2-5 that the time to decay is usually overestimated by the analytical propagator, but the distribution of time to decay as a function of altitude produced by the analytical propagation also resembles that produced by the numerical propagator. Although certain quantitative discrepancies appear between the analytical and numerical propagators, the analytical solution is able to capture the overall effects of drag and $J_2$ as a function of time, while achieving orders of magnitude shorter computational times: which is particularly meaningful when propagating tens of thousands to millions of resident space objects.



(a) Analytical propagator        (b) Numerical propagator
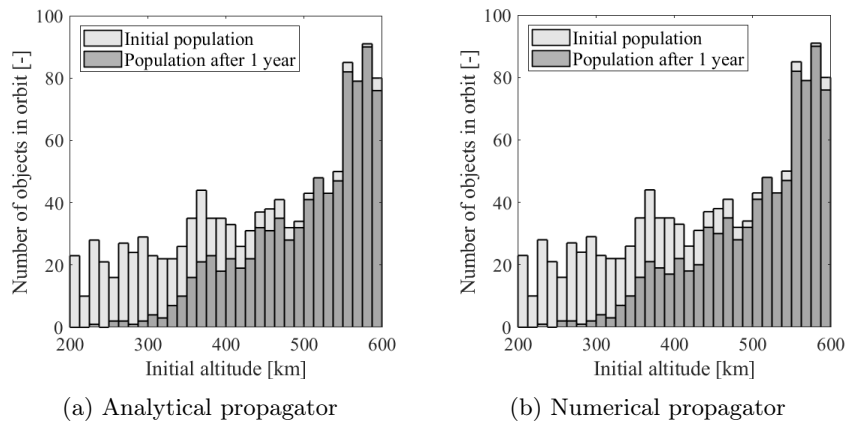
Figure 2-2: Number of objects in orbit depending on initial altitude. Altitude is binned at 12.5 km.

### 2.2.2 Initial Population and Data Sources

Simulations that have a basis in today's orbital environment require some data to seed the initial population. A range of orbital parameters can be provided to the simulation, which can be sampled to seed the initial orbital distribution. Each object can have a unique lifetime, station-keeping methods, failure rate, size, etc. to characterize its behavior and potential interaction with other objects. The initial debris environment is determined. Depending on the analysis, the size, number, and orbital parameters of these objects can be set. The minimum size debris to be considered in the model will also be an input parameter, which will affect

(a) Analytical propagator  (b) Numerical propagator
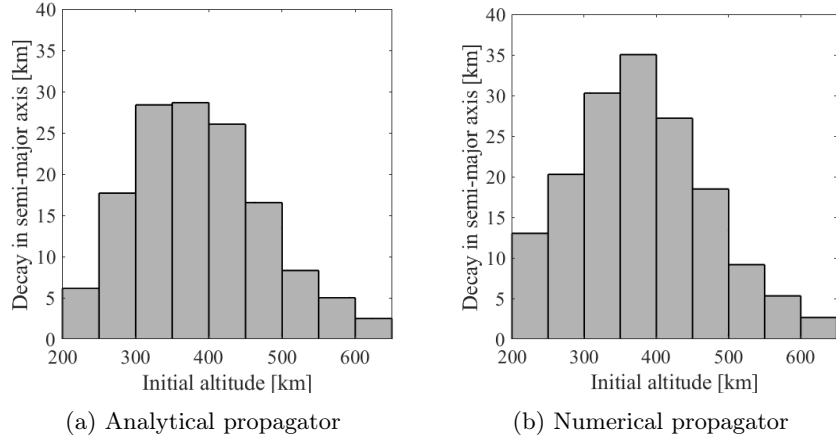
Figure 2-3: Decay in semi-major axis depending on initial altitude.



(a) Analytical propagator  (b) Numerical propagator
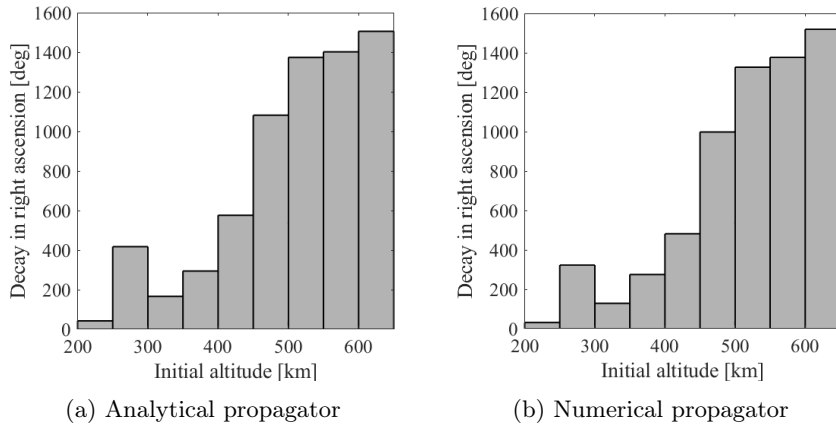
Figure 2-4: Decay in right ascension depending on initial altitude



(a) Analytical propagator  (b) Numerical propagator
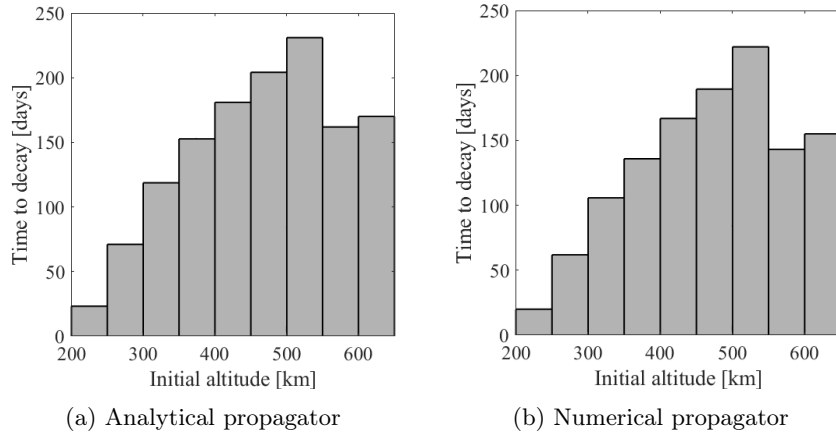
Figure 2-5: Time to decay depending on initial altitude

the number of objects in the simulation. The PDF of the debris population parameters can be supplied from LEO debris models such as ESA's MASTER model [49] and the current space catalog.

Two Line Element sets (TLEs) are used to identify objects that are currently in orbit around Earth. The

model considers a total of around 24,000 space objects obtained from Space-Track (as of September 2022)[1]. In order to have a complete dataset, some other information such as mass, diameter, status, object-class, and launch date need to be gathered. The physical characteristics, the date of launch, and the object-class are retrieved through DISCOS[2] developed by the European Space Agency. For up-to-date active/inactive status of payloads CelesTrak [3] is used. This may be important, as active payloads are able to perform station keeping and collision avoidance maneuvers and may attempt to dispose after their mission is over. After processing the data, MIT's catalog with an epoch of January 1 2022 consists of 21,014 TLEs, out of which 10,869 are debris, 7,015 payloads of which 5,129 active and 1,886 inactive, 1,421 rocket bodies, and the remaining 1,709 Mission Related Objects (MRO).

Table 2.1: Definition of parameters for each orbital object in MOCAT-MC

| Column | 1 - 6 | 7 | 8 | 9 | 10 | 11 | 12 |
|---|---|---|---|---|---|---|---|
| Description | $\bar{a}, \bar{e}, \bar{i}, \bar{\Omega}, \bar{\omega}, \bar{M}$ | $B^*$ | mass | radius | error flag | control flag | $a_{desired}$ |

| Column | 13 | 14 | 15 - 16 | 17 - 19 | 20 - 22 | 23 | 24 |
|---|---|---|---|---|---|---|---|
| Description | Mission duration | Contel Num | Date created, Date launched | $r_{x,y,z}$ | $v_{x,y,z}$ | object class | ID |

Parameters that are defined and tracked for each object throughout the simulation are defined in Table 2.1. The mean osculating orbital elements are defined with semimajor-axis, eccentricity, inclination, RAAN, argument of perigee, and mean anomaly as: $[\bar{a}, \bar{e}, \bar{i}, \bar{\Omega}, \bar{\omega}, \bar{M}]$. $B^*$ is an adjusted value of the ballistic coefficient of the satellite. Mass is denoted in kg, and radius is denoted in meters. The error flag is used for the internal propagation error state. The control flag denotes whether the object has control to stay at the desired semi-major axis $a_{desired}$ for the mission duration after launch. The constellation number denotes which constellation the object is part of, as defined in the constellation input file. The date created and the date launched are defined in modified Julian day (MJD). $r_{x,y,z}, v_{x,y,z}$ are cartesian states in inertial frame (ECI). The object class denotes the type of object, as described in Table 2.2. These definitions are consistent with those of the ESA MASTER database [49]. The satellite ID is defined for the purpose of tracking individual objects throughout the simulation.

Table 2.2: Definition of object-class in MOCAT-MC

| Class | 1 | 2 | 3 | 4 | 5 | 6 | 7 | 8 | 9 | 10 | 11 |
|---|---|---|---|---|---|---|---|---|---|---|---|
| Definition | PL | PL MRO | PL FD | PL D | RB | RB MRO | RB FD | RB D | D | Other D | Ukn |

Although all TLE objects are represented in the DISCOS database, some data entries may be omitted. For MOCAT-MC, DISCOS dataset is used for the physical parameters, launch date (or creation date for debris)

and the type of object as one of eleven categories defined by ESA. As the SatCat TLEs provide orbital parameters and type of object divided into Payload, Rocket Body, Debris, and Unknown, the objects with missing DISCOS data are sampled randomly from the PDF produced by the data from existing equivalent object type using a 2-D Gaussian fit. ESA's DELTA model resamples the by assuming an aluminum sphere for the density to calulate the mass from the radius and vice versa, which often overestimates the density of fragmentation debris.

### 2.2.3 Launch Rate

The launch profile of new objects can be defined arbitrarily. Historical launch rates and object parameters can be used, such as the past $n$ years of launches, where those objects are launched into the same orbits with the same object parameters, such as mass and shape. Some other studies have divided the types of objects into constellation objects, which have a constant launch rate for replenishment level launches assuming some constant desired constellation size, while nonconstellation objects would be launched at the historical rate over the $n$ year period. Another method of launching would be completely arbitrary, where payloads with some lifetime are launched into the orbit of interest with randomized orbital parameters. Debris and rocket bodies can also be introduced per launch, as desired. For both of these scenarios, an assumed increase in launch rate per year can be specified, modeling some linear increase in launch activity with respect to time. The FCC and ITU filings for future megaconstellation have been compiled and are discussed in Sec. 2.4.5.

### 2.2.4 Atmospheric Density Modeling

RSOs in the LEO regime are strongly perturbed by the Earth's upper atmosphere. Hence, accurate propagation of LEO RSOs requires an accurate estimate of the drag force caused by the Earth's upper atmosphere. However, the ionosphere-thermosphere system is highly dynamic and is strongly influenced by solar and geomagnetic activities.

In lieu of a static exponential density model, the Jacchia-Bowman 2008 (JB2008) density model is used in this work [17]. The JB2008 density model is an empirical density model that is extrapolated based on past historical atmospheric density data to capture the statistically average behavior of the atmosphere under different solar and geomagnetic forcing. The main drivers for the JB2008 density model are a set of solar fluxes measured at different wavelengths and the temperature change due to the Disturbance Storm Time (DSTDTC) index. The set of solar fluxes captures the effects of solar activities; the DSTDTC index, on the other hand, captures the effect of geomagnetic activities on the thermospheric density field.

The difficulties in accurately predicting the long-term solar and geomagnetic indices are one of the main challenges with using the JB2008 density model for long-term prediction. The solar fluxes closely correlate to the solar cycle. A solar cycle lasts approximately 11 years and corresponds to the Sun's magnetic field cycle. Here, a moderately active solar cycle is assumed for all future solar cycles, using the observed solar indices for a moderately active solar cycle taken from [139]. At each propagation instance, the solar indices

are sampled as independent Gaussian variables around the mean observed values, depending on the relative month in the solar cycle. On the other hand, a fixed DSTDTC value of 58k is used, which corresponds to the historical long-term mean DSTDTC value. Note, however, that the strength of the solar cycle tends to vary across different solar cycles and cycles over periods of high activities and low activities, and this is not reflected in our current assumption of consistently moderately active solar cycles.

Note that controlled payloads are propagated such that the semi-major axis will stay relatively constant. When $a$ of such an object deviates by some defined amount from $a_{desired}$, $a$ is simply updated to become $a_{desired}$ to simulate station-keeping at the desired altitude.

The $B^*$ value can be defined in several ways. When TLEs are supplied, the $B^*$ value supplied from the catalog can be used. Note that the provided value may be negative and nonphysical, as this parameter is often a free parameter that is fitted to the sensor data to fit an orbit to create the TLEs. Figure 2-6 shows the distribution of some TLE sampling over a period of several days, showing the prevalence of negative $B^*$ values and the magnitude with which the value varies from epoch to epoch. Horizontal lines denote the values of $B^*$ that span more than the limits of the axis. This shows a wide range of the $B^*$ values even for the same object within a week as reported by the TLE. For non-SGP4 propagators, B-star or AMR should be calculated separately. MOCAT-MC calculates the AMR from the physical properties of the objects, as noted in the ESA DISCOS database. A snapshot of the $B^*$ values from TLEs from January 2023 is shown in Figure A.1 in the appendix.
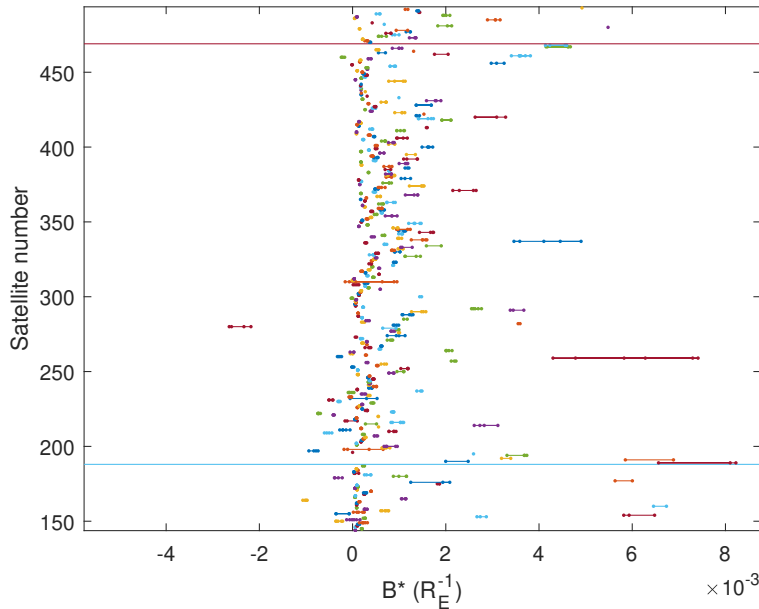


Figure 2-6: Variability of $B^*$ values from Space-track.org TLE's across a 5 day span

Alternatively, $B^*$ can be recalculated from the physical characteristics of the satellite. This method calculates the parameter as:

$$B^* = \frac{C_D \cdot r^2}{2m} \cdot 0.157 \tag{2.3}$$

where $C_D$ is the ballistic coefficient and is simply defined as $C_D = 2.2$. The unit for $B^*$ is $R_E^{-1}$.

To include the effects of the space weather, in terms of solar and geomagnetic activities, on the atmospheric density, the static exponential density model can be replaced by the following density model [9]:

$$
\begin{cases}
T = 900 + 2.5\,(F_{10.7} - 70) + 1.5 A_p \\
m = 27 - 0.012\,(h - 200) \\
H = T/m \\
\rho = 6 \cdot 10^{-10} \exp\left(-(h - 175)/H\right)
\end{cases}
\tag{2.4}
$$

where $F_{10.7}$ is the solar radio flux, measured in solar flux units (SFUs), with one SFU equal to $10^{-22}$ W/m$^2$Hz, $A_p$ is the geomagnetic planetary index, and $T$ is the temperature in Kelvin. In periods of strong solar and geomagnetic activity, both the values of $F_{10.7}$ and $A_p$ increase, heating the atmosphere and increasing the atmospheric density with a consequent stronger drag sinking mechanism.

Since the above model is valid within the range 150-1100 km, the reference altitude in Eq. (2.4) is assumed to be fixed at 150 km, for altitudes below 150 km, and at 1100 km, for altitudes above 1100 km.



(a) Static exponential model       (b) Extrapolated JB2008 model
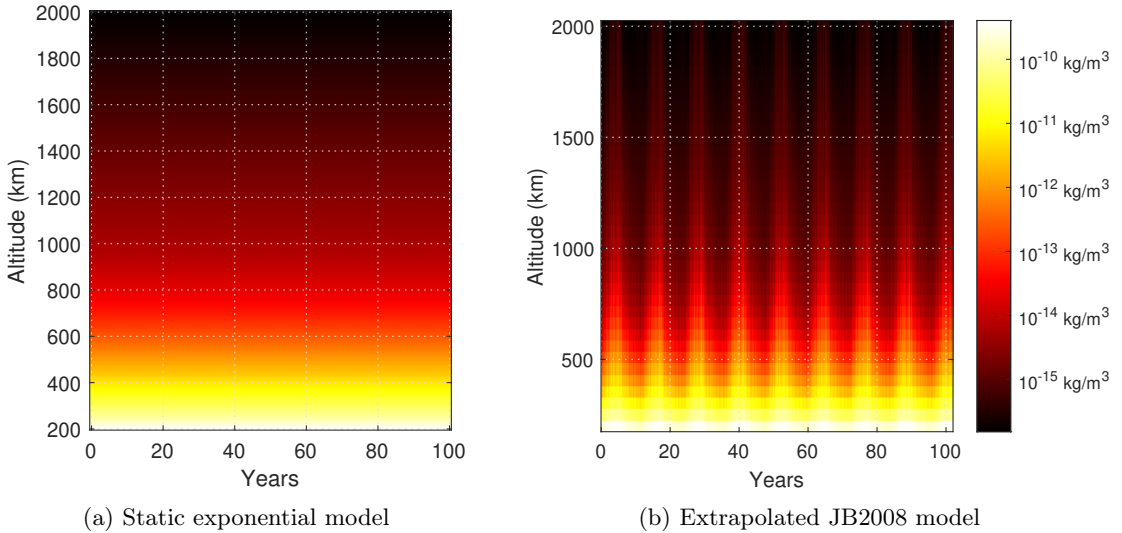
Figure 2-7: Comparison between the two atmospheric models

## 2.2.5   Collision detection

Sensors and algorithms were quickly developed to track orbiting objects soon after the first satellites were launched. As the number of objects began to increase, and especially so with human activity in LEO, prediction of the collisions between these objects has become even more important. There has always been debris associated with launches, be it rocket bodies or small pieces coming from the launch process.

In MOCAT-MC, a stochastic sampling-based method called the Cube method is used as described in

[92, 87]. In this method, the orbital volume is divided into equally sized cubes and the RSO states are propagated arbitrarily to see how often RSOs end up in the same volume, which can then count towards an interaction. For accuracy, the cube volume must become small to the extent where computation for a large number of satellites also becomes untenable [78].



(a) Divide the space into cubes at each timestep

(b) If two or more objects occupy the same cube, approximate the objects as gas particles in the cube volume
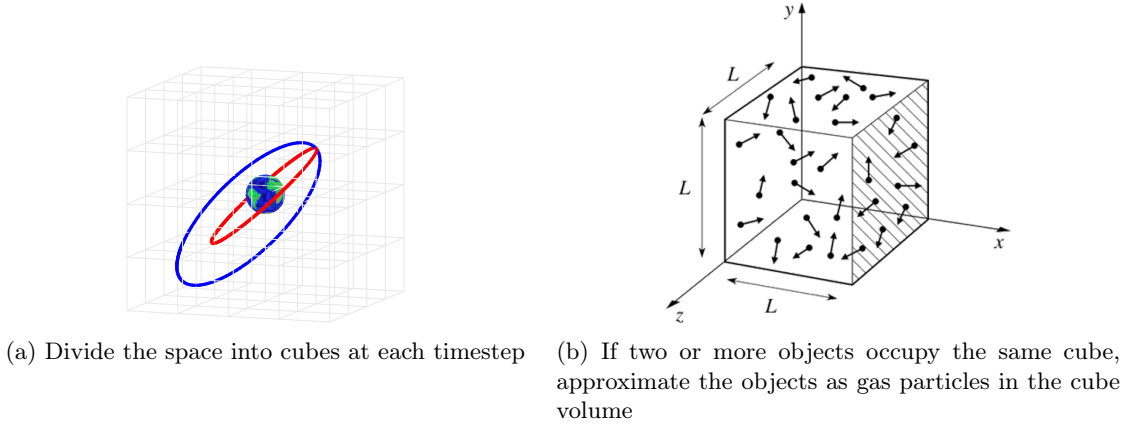
Figure 2-8: The Cube collision detection scheme involves a two-step process: proximity filter prior to employing the gas particle collision model

This method estimates the long-term collision probability by uniformly sampling the objects in time. The method treats any pair of objects to have a static probability of collision over a long period of time, and the collision probability is calculated for a particular moment in time when the objects are near each other. This is determined by discretizing the orbital space into cubes and flagging the two objects as close when they are in the same cube. At this point, the kinetic theory of gas is applied to determine the probability of collision. The probability of collision is calculated for any two objects that reside within a discretized cube concurrently as

$$P_{i,j} = s_i s_j V \sigma dU \tag{2.5}$$

where $s_i$ and $s_j$ are the spatial densities of objects $i$ and $j$ in the cube, respectively, $V$ is the relative velocity between the two objects, $\sigma$ is the collision cross-sectional area, and $dU$ is the volume of the cube. Note that this probability is the probability of collision per time, and the aggregate collision for the time step $\Delta t$ is calculated at that time step as $P_{i,j}\Delta t$. The length of a cube for the proximity filter is often taken as 1% or less of the mean semimajor axis of objects [92], which is around 70 km for a population of LEO RSOs. The 10 km cube length is often used to exclude collisions between objects that are well controlled within its altitude region. This two-step algorithm is described graphically in Fig. 2-8. The sensitivity and validity of using the Cube algorithm with various discretized time steps and cube size for collision detection modeling has previously been explored in the literature [77]. The relationship between cube resolution and $P_{i,j}$ estimation is explored later in the paper to describe MOCAT-MC and its collision probability parameters. One benefit of the Cube approach is that the computational complexity is $\mathcal{O}(n)$ as opposed to the exhaustive pairwise comparison that yields $\mathcal{O}(n^2)$ for $n$ objects. The Cube method is used in MOCAT-MC as the primary collision

detection model, as it has been well validated in the literature and due to its computational efficiency.

A comparison between the deterministic method and the stochastic methods is shown later in the results section. Once a collision is detected, fragmentation dynamics using the NASA Standard Breakup Model (EVOLVE4) is used as described in the next section.

### 2.2.6  Fragmentation Model

NASA's Standard Breakup Model (SBM) [55] is a semiempirical model based on evidence compiled from historical orbital data and terrestrial hypervelocity tests such as the Satellite Orbital Debris Characterization Impact Test (SOCIT). The model is deterministic and sample-based, and the samples are described by $L$ the characteristic length, $A/m$ the area-to-mass ratio, and $\Delta v$ the ejection velocity in a random direction from the parent velocity.

The propagation of debris clouds has also been an active area of research. Nominally, a covariance propagation model may be adapted, though the log-normal distribution of the number of objects and imparted $\Delta V$ in a collision is ill-suited to the multivariate Gaussian assumption for covariances. The evolution of debris clouds and their effect on key LEO orbits have been formulated and analyzed in [45, 24, 39]. Efficient cloud propagation has been done using DAMAGE and other MC approaches. [122, 74, 66] The specific contribution of explosion and future collision fragments to the orbital debris environment showed the importance of mitigating fragmentation events [135, 125]. The probabilistic uncertainty of the lifetime of the debris was analyzed in [28, 97, 77]. The effect of thermospheric contraction on debris reentry has been modeled [80]. Emperical modeling from fragmentation events such as the Iridium-Cosmos collision and the 2013 ASAT test has validated some models [149, 58, 134].

Fragmentation events in MOCAT-MC are simulated with the NASA standard breakdown model (SBM) [55, 63]. The NASA SBM is a semi-empirical model based on evidence compiled from historical orbital data measured *in-situ* on-orbit as well as terrestrial radar measurements and terrestrial hypervelocity impact experiments. The model is deterministic and sample-based, and samples are described by $L$ the characteristic length, $A/m$ the area-to-mass ratio, and $\Delta v$ the ejection velocity in a random direction from the parent velocity.

Ref. [40] reformulates the model into a probability distribution function, where the number of objects produced with $L$ that is greater than some lower bound $L_0$ is

$$N_L(L_0) = k L_0^{-\beta} \qquad k, \beta > 0. \tag{2.6}$$

$k$ and $\beta$ are unitless parameters that depend on the type of fragmentation and the physical characteristics of the objects involved. Although the SBM does not inherently conserve physical quantities such as mass and kinetic energy [38], this formulation of the breakup model into a probability distribution function allows the conservation of mass and energy to be enforced.

The model takes as input the smallest characteristic length $L_C$ for the generation of debris objects. The characteristic length is defined as the mean of the three maximum orthogonal projected dimensions of the object as $L_C = (L_x + L_y + L_z)/3$.

This is an input variable that can be adjusted, though MOCAT-MC's default value is 0.1 m. Note that $L_C$ will be treated as an equivalent diameter $d$. The number of fragments $n_f$ of diameter $d > L_C$ can be computed as

$$
n_f = \begin{cases} 6\, c_s\, \hat{L}_c^{-1.6} & \text{for explosions} \\ 0.1\, \hat{m}^{0.75}\, \hat{L}_c^{-1.71} & \text{for collisions} \end{cases}
\tag{2.7}
$$

where

$$
\hat{m} = \begin{cases} \dfrac{m_t + m_p}{[\text{kg}]} & \text{for } \tilde{E}_p \geq \tilde{E}_p^* \\ \dfrac{m_p\, v_i^2}{1000[\text{kg}\,(\text{m/s})^2]} & \text{for } \tilde{E}_p < \tilde{E}_p^* \end{cases} \qquad \text{with} \qquad \tilde{E}_p = \frac{m_p\, v_i^2}{2\, m_t}
\tag{2.8}
$$

Note that the symbol ˆ indicates normalized quantities, $m_t$ and $m_p$ are, respectively, the target (mostly derelicts or rocket bodies) and the projectile mass, $v_i$ the relative velocity, $\tilde{E}_p$ the specific energy of the projectile, and $\tilde{E}_p^* = 40$ [kJ/kg] the specific energy threshold for a catastrophic collision.

The scaling parameter $c_s$ in Eq. 2.7 is an event-specific calibration constant based on historic events and an empirical correction for certain classes of fragmentation events (with $0.1 \leq c_s \leq 1.0$). For a mass between 600 kg and 1000 kg, the calibration factor is $c_s = 1.0$. However, past fragmentation events showed very different characteristics, thus the break-up models need to be calibrated.

### 2.2.7 Area to Mass Ratio Calculation

According to the NASA standard break-up model, the area-to-mass ratio $A/m$ for new fragments is assigned according to a bimodal probability density function $p(\chi, \vartheta)$.

$$
p(\chi, \vartheta) = \alpha(\vartheta)\, p_1(\chi) + (1 - \alpha(\vartheta))\, p_2(\chi)
\tag{2.9}
$$

where $\chi = \log_{10}(\{A/m\}/[\text{m}^2/\text{kg}])$ is the area-to-mass parameter, $\vartheta = log_{10}(d/[\text{m}])$, and $p_{1,2}$ indicates the normally distributed density functions. The parameter $\alpha$, the means $\mu_{1,2}$, and the standard deviations $\sigma_{1,2}$ are calculated as stated in the NASA's new EVOLVE 4.0 breakup model [55]. According to which, the effective cross-section $A$, function of the fragment diameter d is

$$
A/[\text{m}^2] = \begin{cases} 0.540424(d/[\text{m}])^2 & \text{for } d < 1.67\text{mm} \\ 0.556945(d/[\text{m}])^{2.0047077} & \text{for } d \geq 1.67\text{mm} \end{cases}
\tag{2.10}
$$
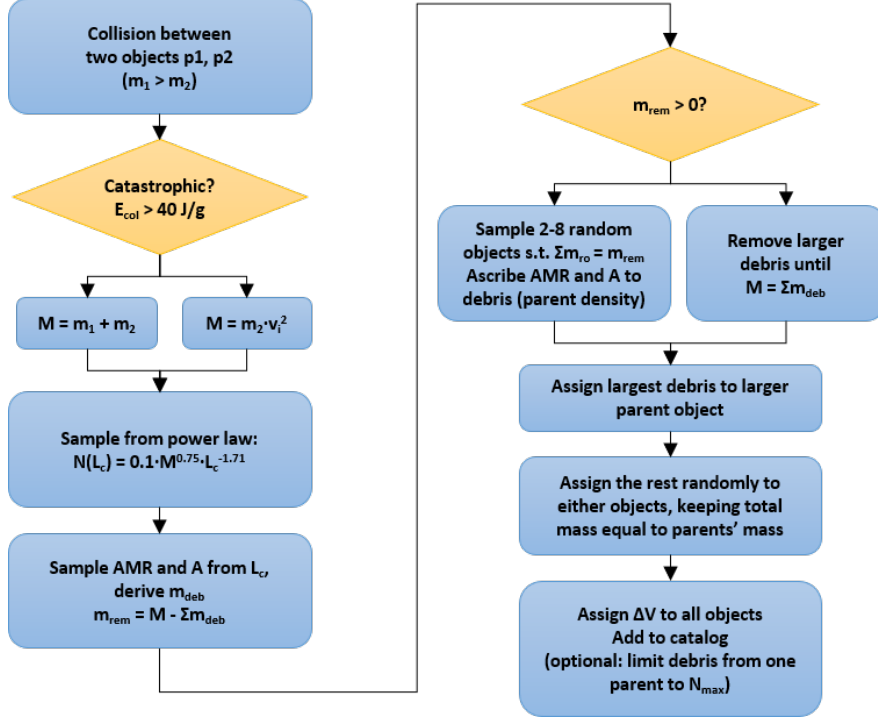
Figure 2-9: NASA Standard Breakup Model as implemented in MOCAT-MC

The fragment mass is thus determined as

$$m = \frac{A}{A/m} \tag{2.11}$$

The model requires also to assign the imparted fragmentation velocities, which are sampled from a normal distribution characterised by the following mean value and standard deviation

$$\mu_\nu = 0.2\chi + 1.85 \quad \sigma_\nu = 0.4 \quad \text{for explosions}$$
$$\mu_\nu = 0.9\chi + 2.90 \quad \sigma_\nu = 0.4 \quad \text{for collisions} \tag{2.12}$$

where $\nu = \log_{10}(\Delta v/[\mathrm{m/s}])$.

The generation and propagation of the debris at various times is shown in Fig. 2-10. The 3d plot of the fragments shows 3 epochs: immediately after the collision, one revolution after, and two revolutions after the collision. The fragments are generated by MOCAT-MC using the NASA Standard Breakup Model with $L_C = 10$ cm. The propagated locations of the original two objects are shown as red circles. As implemented in the NASA SBM, the magnitude of the $\Delta V$ imparted to each of the debris is stochastically assigned as a magnitude. For momentum conservation, it is assumed that the direction of the magnitude is uniformly distributed spherically, as is also implemented in the literature [20, 40, 126].
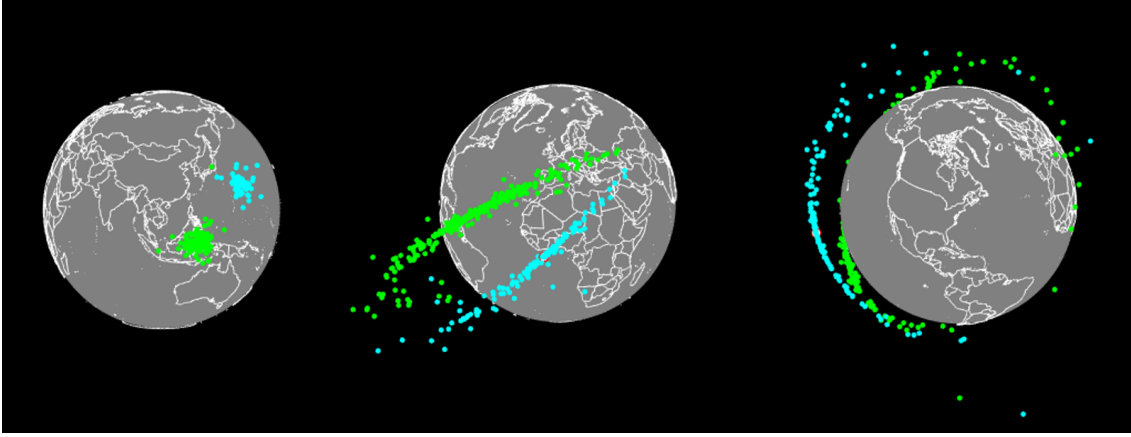
Figure 2-10: Time-series graphical view of the debris generated from a collision between two payloads

### 2.2.8 Active Payload Orbit Control

During propagation, each object is subjected to the effects of atmospheric drag, which causes the reduction of the semi-major axis $a$. On the one hand, this consequence is beneficial for LEO safety because it removes derelicts and debris, but on the other hand, it has to be counteracted by active satellites. Depending on the mission altitude and the solar activity level, perturbations, mostly drag effects, could require a satellite to perform station-keeping maneuvers even once per orbit. For current and future satellites, in particular those composing megaconstellations, electric propulsion seems to be the adopted hardware solution. This kind of propulsion system can provide a small level of thrust for a limited amount of time due to limitations in the available electric power. All of these factors, hardware solution, mission design and mission constraints, could yield a satellite to split a maneuver into a small set of successive sub-maneuvers over each or a few orbits. Since the orbit control modeling is not the main focus of the current paper, the solution here adopted consists of considering the active satellite semi-major axis variation null. In fact, at each time step, all the Keplerian orbital elements, except $a$, are propagated forward in time. More accurate models are planned to be included in future works.

During propagation, each satellite is subjected to the effects of atmospheric drag. To model station keeping maneuvers for active satellites, a threshold on the semi-major axis variation $\Delta a_{thr}$ has been set. The simplified maneuver consists of adjusting the current semi-major axis $a_{current}(t)$ (time dependent) to the initial and desired value $a_{desired}$ whenever, during propagation, the following condition is verified.

$$a_{desired} - a_{current}(t) > \Delta a_{thr} \tag{2.13}$$

Moreover, active satellites are supposed to perform collision avoidance maneuvers with a certain probability of failure, indicated by $\alpha$ in case the satellite encounters a noncooperative species (rocket bodies, derelict or debris), while with $\alpha_a$ if the encounter is between two active satellites. The resulting probability

of collision, computed with Eq. 2.5 is therefore pre-multiplied by one of these two factors as:

$$P_{i,j} = \begin{cases} \alpha_a \ P_{i,j} & \text{active-on-active encounter} \\ \alpha \ P_{i,j} & \text{otherwise} \end{cases} \tag{2.14}$$

Although these terms are user-defined, realistically $\alpha_a < \alpha$, as a pair of satellites are assumed to have a higher chance to successfully perform a collision avoidance maneuver through coordination compared to an active satellite against a debris. For constellation objects, distinction is often made to differentiate the effectiveness of collision avoidance within the constellation operator ($\alpha_{intra}$) and for two different operators ($\alpha_{inter}$). Typically, $0 \approx \alpha_{intra} < \alpha_{inter} = \alpha_a$.

Near-conjunctions for active satellites are a daily occurrence. SpaceX reported that their Starlink constellation has had to maneuver more than 25,000 times in a 6-month span between December 1, 2022 and May 31, 2023 to perform collision avoidance maneuvers. The 18th and 19th Space Defense Squadrons have noted that they have issued more than 170 million conjunction data messages (CDM) for more than 3 million conjunction events between January 2016 and December 2021 [109]. At the current launch rate, the Starlink satellites will have to maneuver more than a million times in a half-year period by 2028 [115].

Despite the large number of potential conjunction events, there has never been an active-on-active collision, leading to a historical trend of $\alpha_a = 0$. Even an active-on-derelict conjunction is quite rare with such safeguard and warnings in place. The first collision between satellites was the Iridium-Cosmos collision in 2009, although the policy of issuing CDMs using high-quality data had not been implemented then [148]. With many more active satellites and potential debris, this rate may increase.

### 2.2.9 Future Constellation Traffic

Future constellation traffic is described by specifying a few parameters per constellation in an external file that is ingested by the simulation during the setup phase. Several parameters must be provided for each constellation. The altitude and inclination are given for each shell or generation of the constellation, and the number of satellites already in orbit at the start of the epoch. Satellite parameters such as mass, radius, and mission life are also required, though missing information will default to using Starlink Gen 1 specifications. The start and end dates of the build-up phase must be supplied to calculate the launch rate during the build-up phase, where a linear build-up phase is assumed. Throughout the operational phase of the constellation, the appropriate amount of replenishment satellites are launched for the satellite that has reached the end of life. The end-of-operation date can be supplied for the constellation, after which no more replenishment satellites are launched. The constellation company index can be supplied to group the separate shells and phases into the same constellation. As described in the previous section, the intra-constellation collision avoidance efficacy can be specified such that the collision within a company's constellation is different from that of inter-constellation collision avoidance efficacy.

## 2.3 Validation

### 2.3.1 Validation against the IADC study

The Inter-Agency Space Debris Coordination Committee (IADC) in 2009 had several space agencies use their MC tools to compare the performance for a strict future scenario [94]. Six models were involved: ASI: Space Debris Mitigation long-term analysis program (SDM), ESA: Debris Environment Long-Term Analysis model (DELTA), ISRO: KS Canonical Propagation model (KSCPROP), JAXA: LEO Debris Evolutionary Model (LEODEEM), NASA: LEO-to-GEO Environment Debris model (LEGEND), UKSA: Debris Analysis and Monitoring Architecture for the Geosynchronous Environment (DAMAGE).

A 2009 baseline environment for debris 10 cm and larger was provided by ESA. The future space traffic model was based on a repetition of the historic 2001-2009 space traffic. Each participating member used its own solar flux projection model. A catastrophic collision was defined as one characterized by an impacter kinetic energy to target mass ratio of 40 J/g or greater. A future post-mission disposal (PMD) compliance level of 90% was assumed for both the spacecraft and launch vehicle stages. The initial simulation epoch was 2009 and was simulated for 200 years. The initial object count was 17070 based on the MASTER database, which included payloads, derelict objects, rocket bodies, and debris. Launches were repeated for launches between the years 2002 and 2008. The payload lifetime was assumed to be 8 years, and no collision maneuvers for any objects were assumed. No explosions were assumed as well.

The six models yielded similar qualitative results and confirmed the instability of the current LEO object population. The six member models revealed a steady increase in the > 10 cm population, despite an assumed global PMD level of 90%, with a catastrophic collision rate varying from once every 5 to 10 years. Most catastrophic collisions occurred near the 800 km and 1000 km altitudes due to high concentrations of space objects there. The study concludes by noting that compliance with existing national and international space debris mitigation measures will not be sufficient to constrain the future LEO object population. To stabilize the LEO environment, more aggressive measures, especially the removal of the more massive nonfunctional spacecraft and launch vehicle stages, should be considered and implemented in a cost-effective manner.

MOCAT-MC was used to run the same scenario to validate its results against the six models used in the IADC study. Although the specifics of the simulation data were not available, the best estimates were used to emulate the same scenario. For example, the initial population of the IADC study starts with 17074 objects in LEO, though the TLEs available for the same epoch yielded around 9874 objects. To start with the same number of objects with a similar altitude density profile, a total of 7,200 debris were added with the orbital and physical properties randomly selected from existing debris. The altitude of the additional debris was selected to match the initial spatial density of the initial population provided in the study, as seen in Fig. 2-11. Although the study was limited to trackable objects, the additional population was likely in the smaller objects compared to the tracked objects with orbits in the TLE catalog. To account for this size discrepancy in debris sampling, the characteristic length of the expanded initial population of TLE/DISCOS
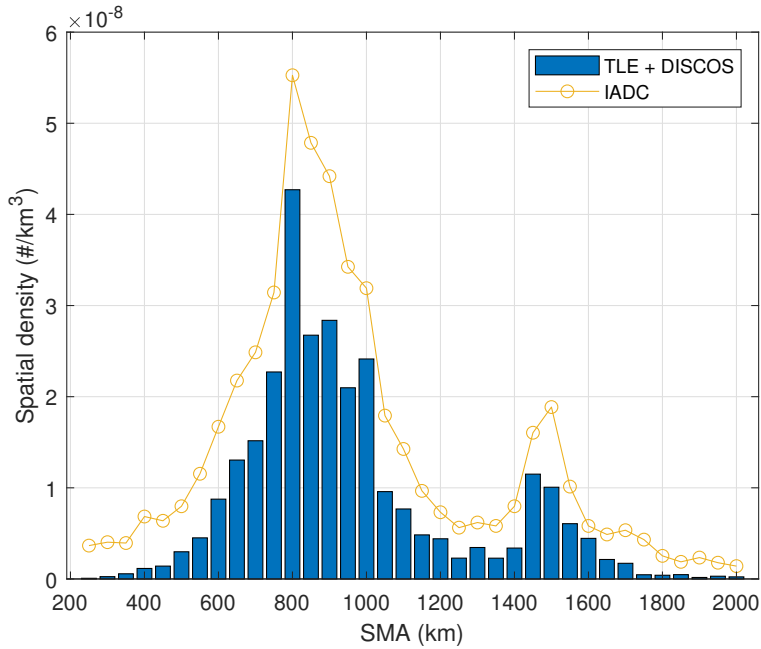
Figure 2-11: Initial population spatial density for IADC study vs TLE for scenario epoch May 2009. Altitude is binned at 50 km.

was reduced by a factor of 1.5. In addition, the PMD scheme assumed within MOCAT removes the object from the simulation when PMD is successful.

The summary of the MOCAT-MC validation exercise using the IADC study scenario is shown in Table 2.3. The comparison of the total population between MOCAT-MC and the models used in the IADC study is shown in Fig. 2-12, and the cumulative catastrophic collisions and the altitude of catastrophic collisions are shown in 2-13 and 2-14 respectively. MOCAT-MC performed similarly to those of the IADC study for these key metrics.

The details of this MOCAT-MC validation scenario are shown in Fig. 2-15. The population per object class shows that the number of debris dominates the > 10 cm population and contributes as the main source for the increase in total object count. The total population for some individual simulation is shown in gray for the population. The intact objects (payload + rocket body) are relatively stable. The collision number shows the relative occurrence between catastrophic collisions and all collisions.

The bottom portion shows the cumulative number of collisions, with the solid line denoting any collisions, whereas the dotted line shows only catastrophic collisions. In this scenario, most of the collisions are deemed catastrophic.
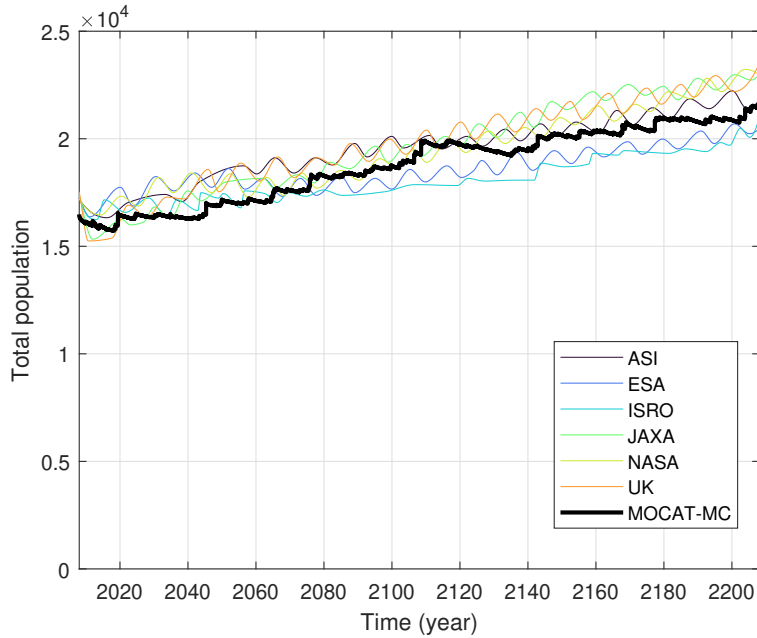
Figure 2-12: Comparison of total population between MOCAT-MC and IADC models [94]
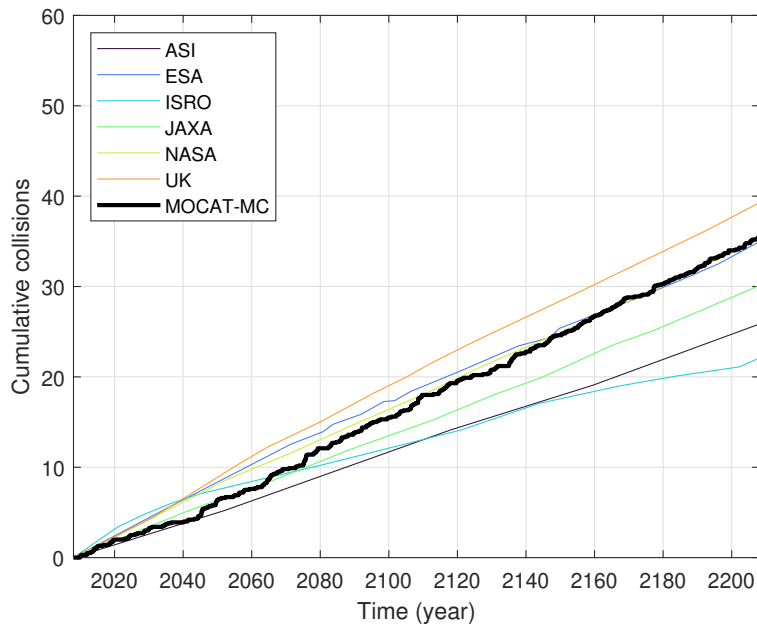


Figure 2-13: Comparison of cumulative catastrophic collisions between MOCAT-MC and IADC models

Table 2.3: Comparison between IADC study results and MOCAT-MC runs of the same NFL scenario

| Agency | ASI | ESA | ISRO | JAXA | NASA | UKSA | All IADC | MIT |
|---|---|---|---|---|---|---|---|---|
| Model | SDM | DELTA | KSCPROP | LEODEEM | LEGEND | DAMAGE | - | MOCAT-MC |
| Runs with $N_{2209} > N_{2009}$ | 88% | 75% | 90% | 88% | 89% | 94% | 87% | 92% |
| Change in Population | +29% | +22% | +19% | +36% | +33% | +33% | +30% | +35% |
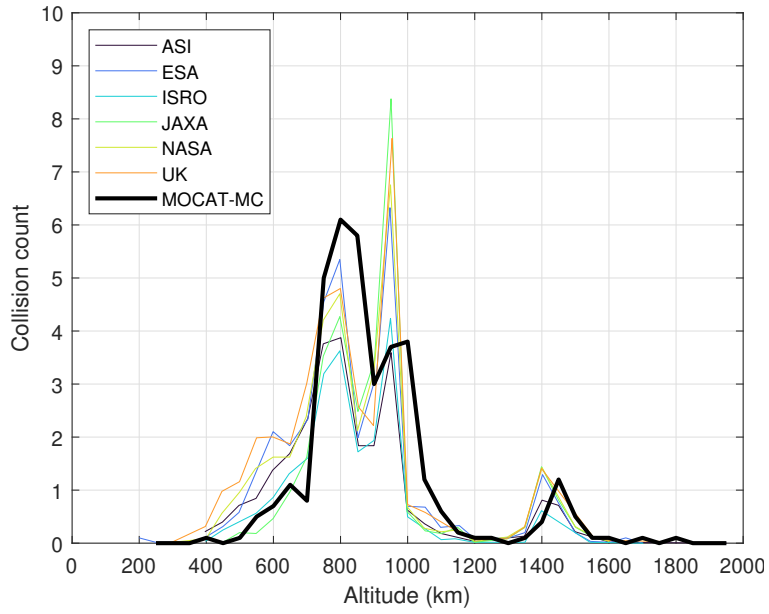
Figure 2-14: Comparison of altitude of catastrophic collisions between MOCAT-MC and IADC models. Altitude is binned at 50 km.



(a) Population per object class



(b) Cumulative collisions
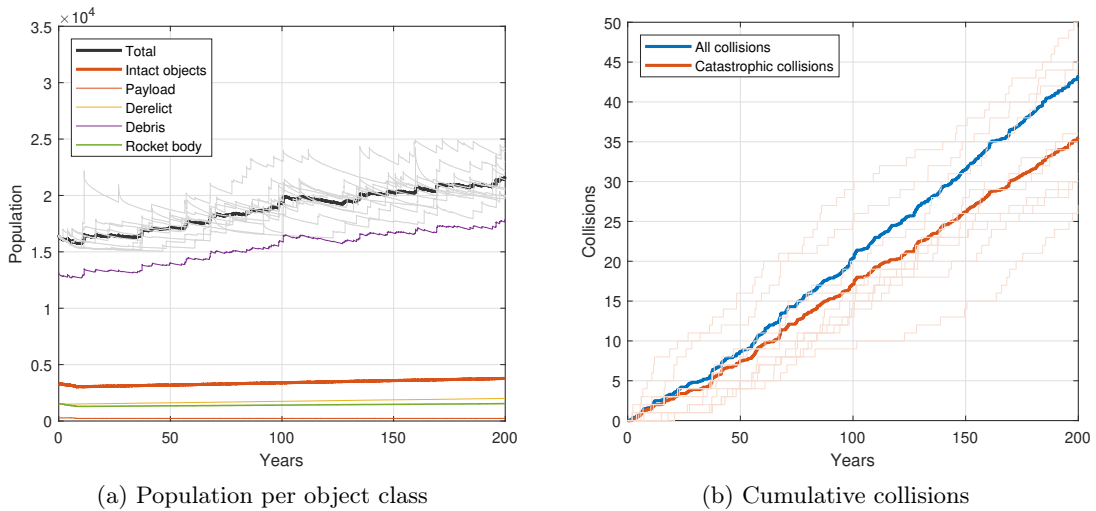
Figure 2-15: Details of the MOCAT-MC results for the IADC scenario

## 2.4 Results and Discussion

Many of the sub-functions were varied to understand the sensitivity of the simulation results on the various input parameters to the model.

### 2.4.1 Cube method Verification

The dependence of collision probability and collision statistics on the cube resolution was investigated. The use of small cube sizes would only consider objects that are close together to calculate a probability of collision, but the probability of collision would be higher as the volume of cube considered is smaller, as described in Eq. 2.5. The computational cost for both the propagation and the cube algorithm scales as $\mathcal{O}(n)$, yet the cube algorithm is typically an order of magnitude or two more computationally expensive compared to the analytical propagation.



(a) Analytical propagator  (b) Numerical propagator
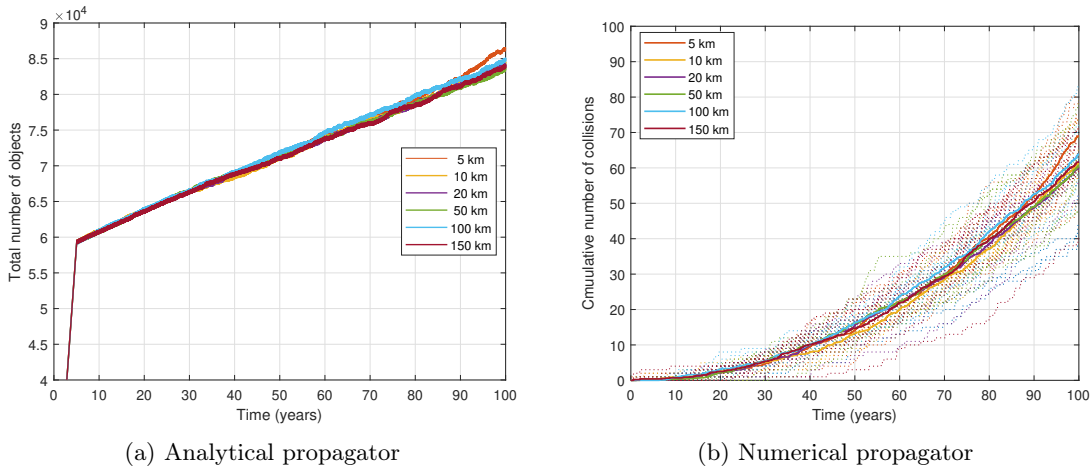
Figure 2-16: Number of objects in orbit depending on initial altitude

### 2.4.2 Convergence for Monte Carlo samples

Sampling-based simulations such as Monte Carlo models require a sufficient number of runs for a stable solution to be achieved. The rate of convergence is described by the central limit theorem, and more samples of the MC will converge to the true population mean. As $n \to \infty$,

$$\frac{\widehat{C}_n - C}{\sigma/\sqrt{n}} \sim N(0\,,\,1). \tag{2.15}$$

The variance of a Monte Carlo estimate of the population mean follows $\sigma_{\bar{X}} = \dfrac{\sigma}{\sqrt{n}}$, where $\sigma$ is the standard deviation of the population and $n$ is the sample size. The rate at which the standard deviation of the distribution of means decreases with the number of samples is $\sqrt{n}$. Thus, the rate of convergence is $\mathcal{O}(\sqrt{n})$. Note that the variance $\sigma_{\bar{X}}^2$ is the mean squared error, which varies linearly with $n$, since the standard
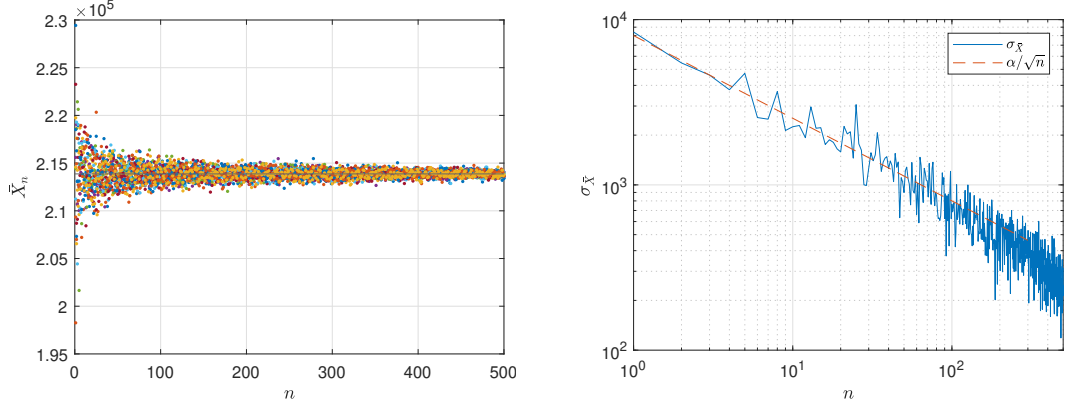
(a) Sample mean of the population at the end of the scenario

(b) Mean standard error of the final population

Figure 2-17: Convergence test for the number of Monte Carlo runs

deviation is the square root of the variance. For a precision of order $\epsilon$, approximately $m$ samples are needed, where $\epsilon \approx \sigma/\sqrt{m}$.

The variance of the distribution of the results can be used to determine the convergence rate of a MOCAT-MC scenario and get a sense of the number of MC runs needed for a high-confidence simulation. A 100-year simulation with 274 launches per year was run for 400 MC simulations. The sampling mean $\bar{X}_n$ and the mean standard error $\sigma_{\bar{X}}$ are shown for the mean of the total number of objects in the $n$ samples in Fig. 2-17. The mean standard error follows the expected convergence rate $\sqrt{n}$ and reaches $0.16\%$ of the population mean at $n > 50$. This shows that a sample size of around 20 yields a mean standard error $\sigma_{\bar{X}} < 1\%$ of the sample mean.

The convergence of the final population of the 200-year MC runs was also analyzed using a two-sample Kolmogorov-Smirnov (KS) test. Subsample sizes of $n_s = \{8, 16, 32, 64, 128, 256, 512\}$ samples were used to test the convergence of the CDF of the subset of samples, which was compared to the final CDF consisting of all 1000 samples. The KS test is a non-parametric statistical test to assess whether two sample sets are of the same continuous distribution, by comparing the CDF of each set. The KS test statistic $D^*$ is computed as the maximum absolute difference between the CDFs as:

$$D^* = \max_x \left( |\hat{F}(x) - F(x)| \right), \tag{2.16}$$

where $\hat{F}(x)$ is the proportion of the subsampled values less than or equal to $x$ and $F(x)$ is the proportion of the all 1000 values less than or equal to $x$. The KS test statistic $D^*$ is a measure of how well a subset approaches the full set. For each subsampling, a different $\hat{F}$ is obtained. Therefore, for each subsample size $n_s$, the test can be performed $Nr$ times, providing an estimate of the $D^*$ value. Figure 2-18 shows boxplots of $D^*$ as a function of $n_s$. As expected, the variability and mean decrease with increasing number of samples. These values asymptotically approach zero as the number of samples reaches infinity. The trend suggests

that an exponentially increasing number of samples is required for a linear increase in accuracy. A 5% error in the CDF would result in a maximum error of 400 objects or 1% of TTD near the median. This error is considered acceptable. Although not necessary, $n_s = 512$ exceeds the maximum error exactly once.
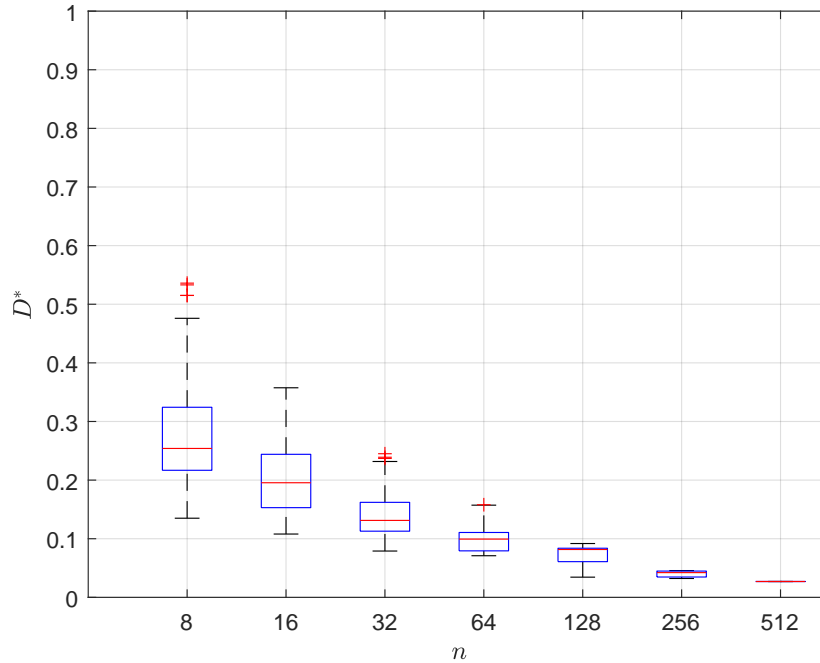


Figure 2-18: Two-sided KS test for the final population value after a series of 200-year simulation with $n_{MC} = 1000$

It is difficult to compare the computational duration required by MC models, as they are not typically disclosed in the literature. Through discussions with the researchers using these other models, some take days to weeks to run using a typical computational setup. However, a comparison of the maximum population modeled is disclosed in the published literature. Some comparison and references are shown in Fig. 2-19, which demonstrates the computational efficiency of MOCAT-MC.

### 2.4.3 Evolution of the future debris population

Two scenarios are run with MOCAT-MC to compare the effect of future launches on the trackable orbital population in LEO with scenario epoch at Jan 1 2023:

- Extrapolation of the recent launch traffic, explosion rates, and post-mission disposal rates

- No future launches scenario where no launches take place after 2022.

The SatCat TLEs were used for the orbital parameters of the trackable debris population with reference epoch Aug 1 2022, while the ESA DISCOS database was used for parameters such as the objects' size, mass,
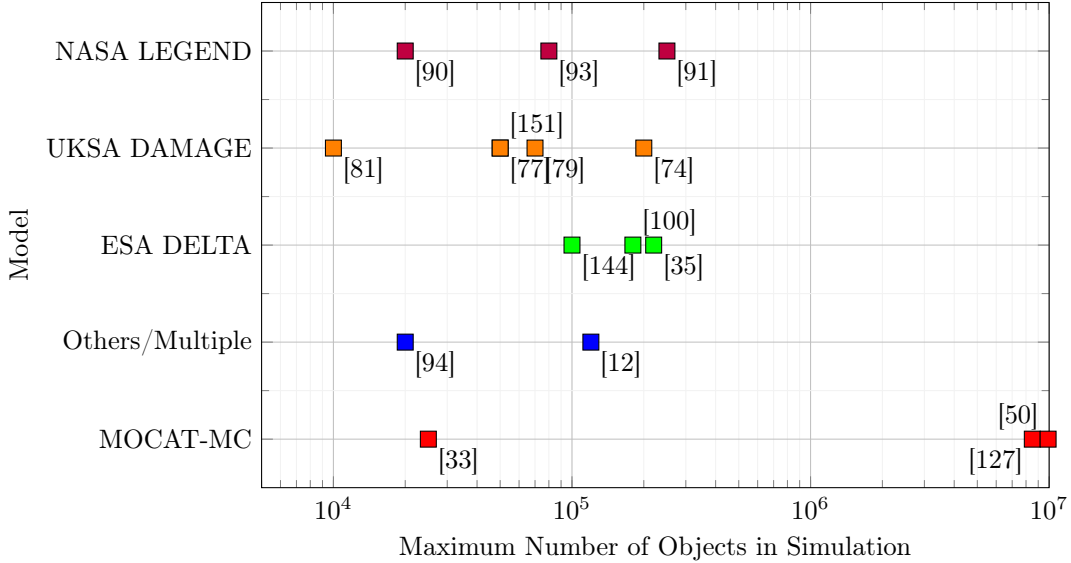
Figure 2-19: Comparison of population modeled in MC simulation tools

object type and launch date. Only objects with perigee between 200 km and 2000 km were considered. This initial population profile is shown in the Appendix Table A.1 and Fig. A.3.

Table 2.4: Parameters for NFL and extrapolated scenarios with 2023 epoch

| Scenario | Launch profile | $\mathbb{E}[P_{explosion}]$ | $P_{PMD}$ | PL lifetime |
|---|---|---|---|---|
| NFL | n/a | n/a | n/a | n/a |
| Extrapolated | repeat 2018-2022 | RB: 2.3 / yr | 0.4 | 8 years |

All simulations were run for $T_{scenario} = 100$ years, $\Delta t$ of 5 days and $a$ limit. 50 Monte Carlo simulations on the MIT Supercloud High Performance Computing cluster [120]. The explosion rate for rocket bodies and payload lifetimes is taken from the ESA Annual Report [34].

Figure 2-20 shows the evolution of the total population from the simulation, as well as the cumulative collisions over the 100-year simulations. The dotted lines above and below denote the 10th and 90th percentiles. The growth of objects can be seen even for the NFL case. Note that the PMD level for recent constellation objects have improved compared to the historic 40% level. This value is varied for further analysis in the future launch case section.

## 2.4.4 No Future Launch Cases from the Past

The No Future Launch case shown in the Validation section shows growth in the number of objects and in the number of collisions despite no new launches occurring. The literature has shown that MC methods point to the fact that the LEO environment was in an era of unabated growth for decades prior [34, 89, 100]. Using the same methodology as in the previous section with the combined dataset between the TLE catalog and the

(a) Population

(b) Cumulative collisions
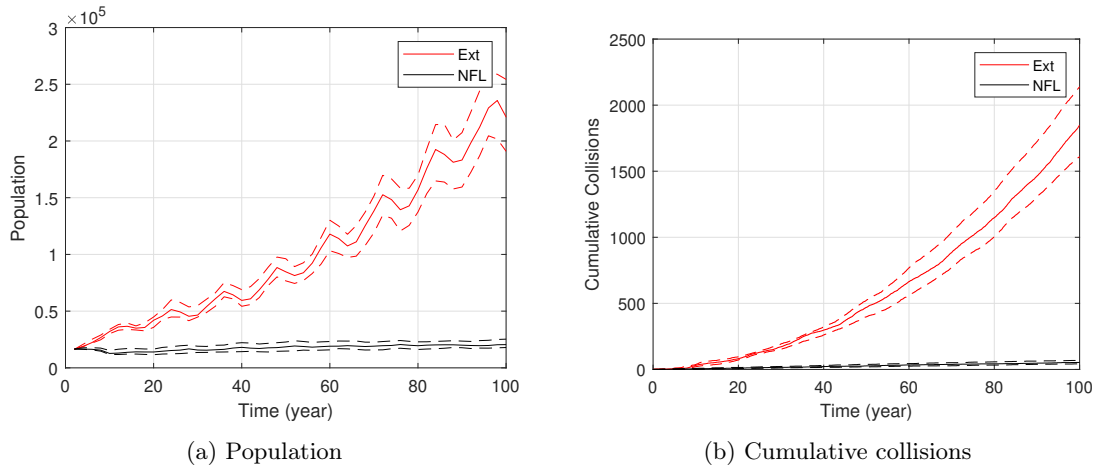
Figure 2-20: Extrapolated and No Future Launch Scenarios for Epoch 2023

DISCOS database, the future LEO environment is simulated at different epochs in the past. The NFL case is run for every year starting in the year 2000 with the cataloged objects at those epochs and removing all future launches to see the growth or decay in the number of objects. January 1 of each scenario epoch year is used for the initial population of objects for the LEO objects, which inherently limited the initial population to the tracked objects. All payloads were assumed to have a mission lifetime of 8 years, after which they undergo PMD with a success rate of 90%. Collision avoidance failure rate of $\alpha = 0.01$ and cube resolution of 10 km. No new objects were introduced into the environment other than through collision dynamics.

The results are summarized in Figs. 2-21 and 2-22. All of the simulations show a substantial growth from the initial population, which indicates that even without future launches, the unabated growth of objects is seen at least as far back as the year 2000 when there were 5000 tracked objects in orbit.

The results show that the growth in the number of objects is consistently present even with epoch in the year 2000, showing the importance of debris mitigation with any population. Of note are the more recent years, where the total count of trackable objects remain roughly steady compared to previous years despite the higher initial population count – in these scenarios, the Starlink satellites have begun to populate, taking up a significant portion of the initial population for those epochs. These active satellites will have been removed entirely from the environment within 8 years of the epoch, other than the few that remain as derelict satellites after failed PMDs. Compared to other satellites, the average lifetime for these active payloads at the simulation epoch are much shorter, therefore the effect on the space environment is much less. For two scenarios with the same number of population, the one with a greater proportion of active satellites that can CAM and PMD will yield a safer and sustainable long-term LEO environment.

The population divided into altitude is shown for the 2023 NFL case in Fig. 2-23. The dense region in the first few years around 550 km denotes the numerous Starlink satellites which mostly PMD after its mission lifetime, which is also seen in the payload population in Fig. A.5. The number of objects above the 700 km range continues to grow, though most objects below deorbit relatively quickly. The growth in the 1000 km
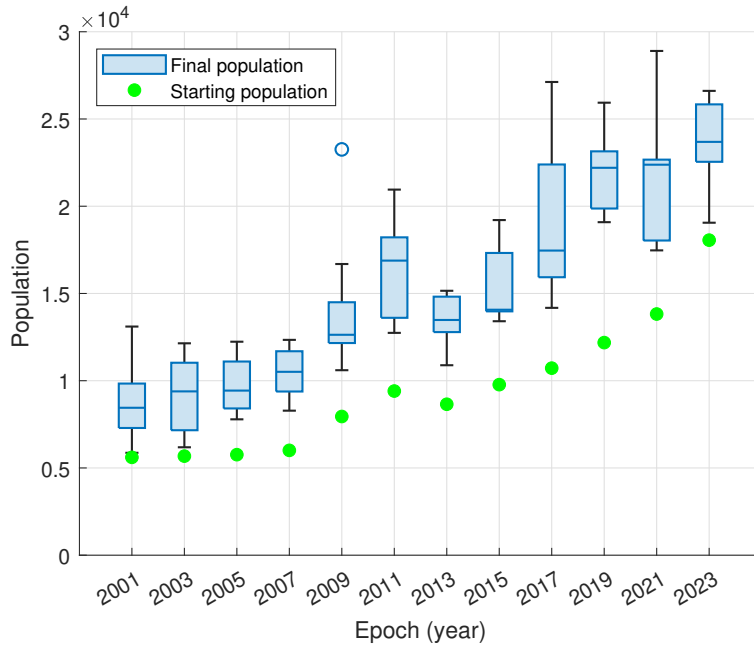
Figure 2-21: Object count for NFL cases starting at different epochs simluated for 100 years
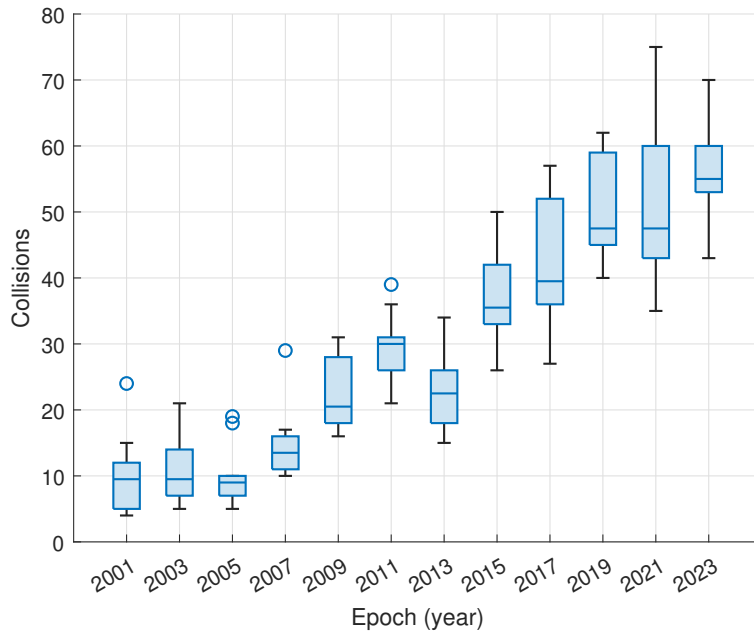


Figure 2-22: Cumulative collisions over 200 years at various epoch for the NFL cases

and 1400 km altitude region is seen, where many derelict and debris exist and are relatively unaffected by atmospheric drag. The altitude regions with higher density start to merge as collisions increase the number of objects and adds objects to a range of altitudes around the collision.
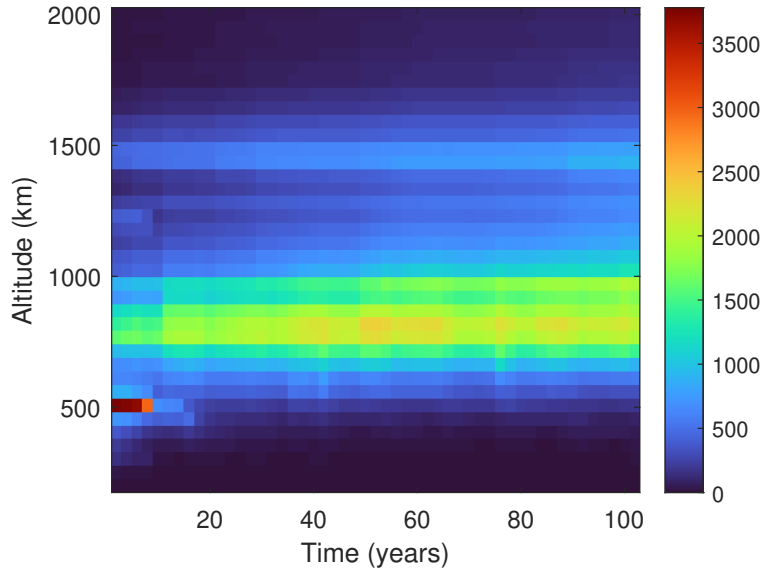
Figure 2-23: Total population per altitude for the NFL case with epoch at 2023. Altitude is binned at 50 km, and time is binned yearly.



(a) Initial and final population



(b) Cumulative collision per altitude
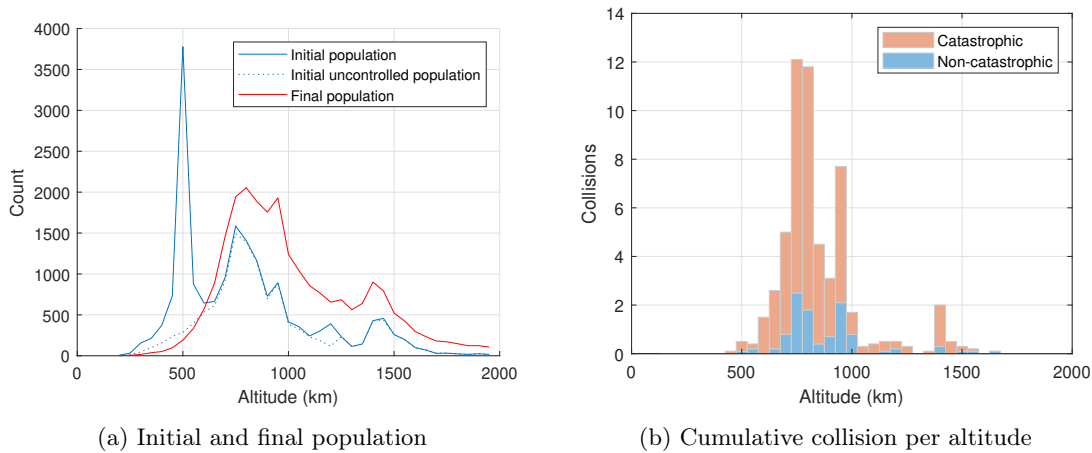
Figure 2-24: NFL case with epoch at 2023. Altitude is binned at 50 km.

### 2.4.5 Future Traffic with Megaconstellations

Megaconstellations are large networks of interconnected satellites that are designed to provide various services, including global broadband internet coverage, Earth observation, and communication capabilities. Two prominent examples of proposed megaconstellations are SpaceX's Starlink and OneWeb. The race to deploy megaconstellations is driven by the potential benefits of widespread internet access, improved communication infrastructure, and enhanced Earth observation capabilities.

It is impossible to forecast the exact state of LEO traffic and launches in the upcoming decades. The best estimate of megaconstellation data can be compiled from various sources, particularly governmental and regulatory bodies such as the FCC and ITU as well as press releases. As of writing, there are more than 50 megaconstellations – defined as constellations comprising more than 1000 satellites – that have been credibly

proposed [106, 48, 29]. Of these, only a few have operational satellites at the time of writing. As these are all commercial ventures, the technology roadmap, market conditions, and consumer demand make the forecasting of successful launch and operation of megaconstellations difficult.

A few examples of megaconstellations are described below. These examples highlight the growing interest in megaconstellation projects across various countries and industries, notably in the internet connectivity and remote sensing applications. Even in the past few years, many prominent megaconstellation projects that have filed with the ITU and/or FCC have been canceled or merged with other efforts. Future launches and traffic due to megaconstellation should be taken as estimates at best; however, this list gives a general overview of launches to expect.

**SpaceX's *Starlink*** SpaceX initiated the Starlink project in 2015 with the goal of creating a satellite network capable of delivering high-speed, low-latency internet access worldwide. The primary motivation behind Starlink was to bridge the digital divide and provide reliable internet connectivity to underserved regions. The constellation would consist of thousands of small, low-Earth orbit (LEO) satellites that creates a mesh network. SpaceX began launching Starlink satellites in batches, starting in May 2019. As of September 2021, SpaceX had already deployed thousands of satellites, and beta testing of the Starlink service had begun in select regions.

***OneWeb*** OneWeb is another megaconstellation project that aims to provide global broadband internet coverage. Founded in 2012, OneWeb intended to build a network of LEO satellites that could deliver internet services to remote and underserved areas. The project was supported by several notable investors, including SoftBank, Qualcomm, and the Government of the United Kingdom. OneWeb faced financial challenges and had to file for bankruptcy in March 2020. However, the company was subsequently acquired by a consortium consisting of the British government and the Indian company Bharti Global. This acquisition provided the necessary funding to continue the project. OneWeb resumed satellite launches in December 2020 and has since progressed with its deployment plans.

**Amazon's *Project Kuiper*** Project Kuiper is Amazon's ambitious venture to create a megaconstellation of satellites to provide global broadband internet coverage. Announced in 2019, the project aims to deploy a network of over 3,200 LEO satellites. Like other megaconstellations, Project Kuiper's objective is to deliver affordable, low-latency internet services to underserved communities around the world.

**Telesat LEO** Telesat, a Canadian satellite operator, is working on its own megaconstellation known as Telesat LEO. The project aims to provide broadband connectivity worldwide using a network of approximately 300 LEO satellites. Telesat LEO's focus is on serving both residential and commercial markets, offering high-speed internet access, enterprise connectivity, and government services.

**E-space's *Semaphore-C*** Greg Wyler's company E-space made headlines when it registered 327,000 satellites using Rwanda as the registration authority through the ITU in 2021. In June 2023, the company filed another constellation *Semaphore-C*, which is a constellation of 116,540 satellites orbiting between 414 and 600 km altitude, registered in France. Due to the recency of this addition, E-Space's constellation will not

be part of this analysis. Note that numerous other studies and literature have ignored this constellation due to the perceived lack of credibility that the constellation will launch in its entirety. The proposed constellation of more than 400,000 satellites would dwarf the total number of the other proposed megaconstellations. This highlights the academic and industry sentiment that regulatory filings are necessary but not sufficient to be used as credible sources for future LEO traffic.

The future launch model used in this case is listed in Table A.2, and totals more than 82,000 satellites in operation just from the megaconstellations alone. The missing mass and radius represented with a '-' used the Starlink satellite as the surrogate (260 kg and 2 m radius), while the start and finish years were set to be the latest dates for the other constellations with some data (2035 to 2055 for Guanwang). Fig. 2-25 visualizes the launches. Note that the replenishment launches are not shown in this figure. An average of $n/yr_{missionlife}$ satellites per year will be required to launch in order to maintain the current number of satellites $n$.

Three subsets of these megaconstellation launch scenarios are also chosen to be simulated.

*Case 1*: all of the filed megaconstellations as shown in Fig. 2-25, which totals 84139 operational megaconstellation satellites.

*Case 2*: just the constellations filed by Starlink, Kuiper and OneWeb, all of which have some constellation presence as of Jan 2024. This totals 44716 operational megaconstellation satellites.

Lastly, *Case 3*: which comprises of just Starlink v1, v1.5, Kuiper and OneWeb. Compared to Case 2, this case removes the largest megaconstellation proposed considered, which is Starlink v2. This totals 22228 megaconstellation satellites.
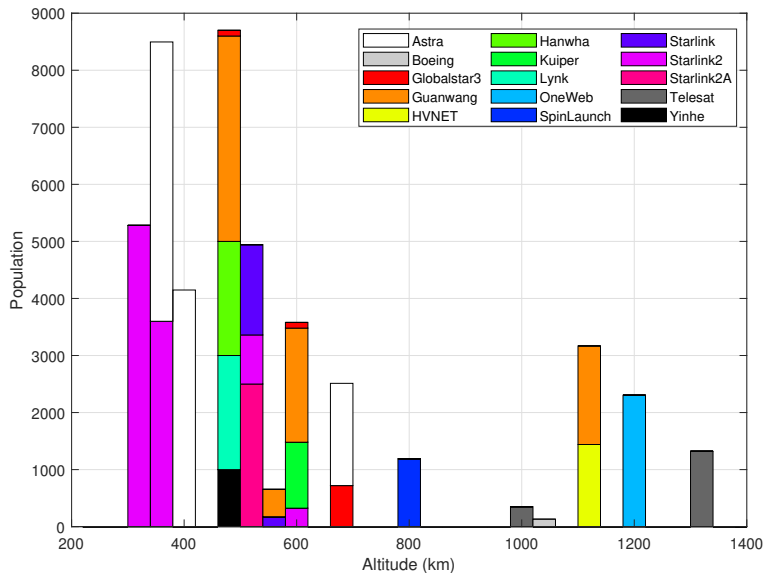


Figure 2-25: Modeled total operational population per megaconstellation

The simulation results for the three cases along with the no future launches case are shown in Fig. 2-26. Growth in the number of objects is clearly seen for all cases. Notable are the S (payload) and D (derelict)
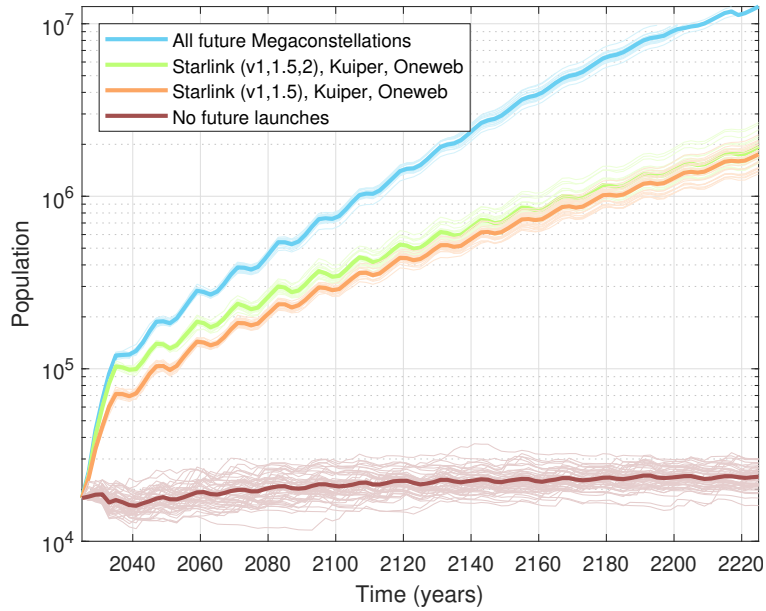
Figure 2-26: Total population in LEO with future megaconstellation launches



(a) Payload population

(b) Derelict population
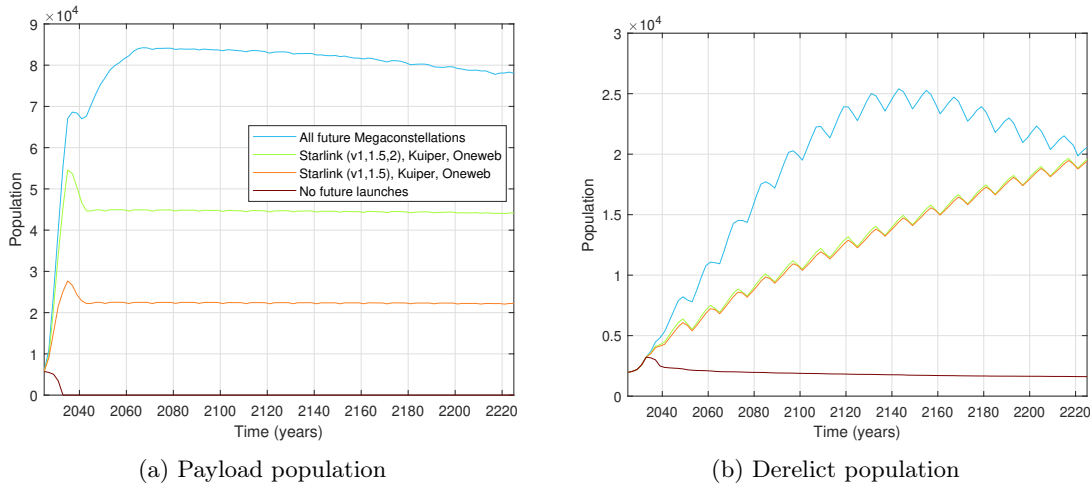
Figure 2-27: Payload and derelict population with various future megaconstellation launch models

plots in Fig. 2-27 – the number of objects grows with increasing launch scenarios, but at the highest number of launches, the number of payloads start to decrease, despite the 1% probability of failure to avoid a collision. That effect is more pronounced in the derelict class where such avoidance is not possible, and the number of derelict objects start to dwindle after 100 years. It is also seen in these charts that the number of objects likely will grow even without new launches. This is in line with the findings from literature and highlights the urgent need to limit the creation of derelict objects through higher PMD rates, and effective collision avoidance maneuvers to limit fragmentation events. The temporal population evolution per altitude is shown in Fig. 2-28. This clearly shows the large amount of accumulation above 1000 km region.

The population difference between objects above and below 700 km shows the accumulation rate between
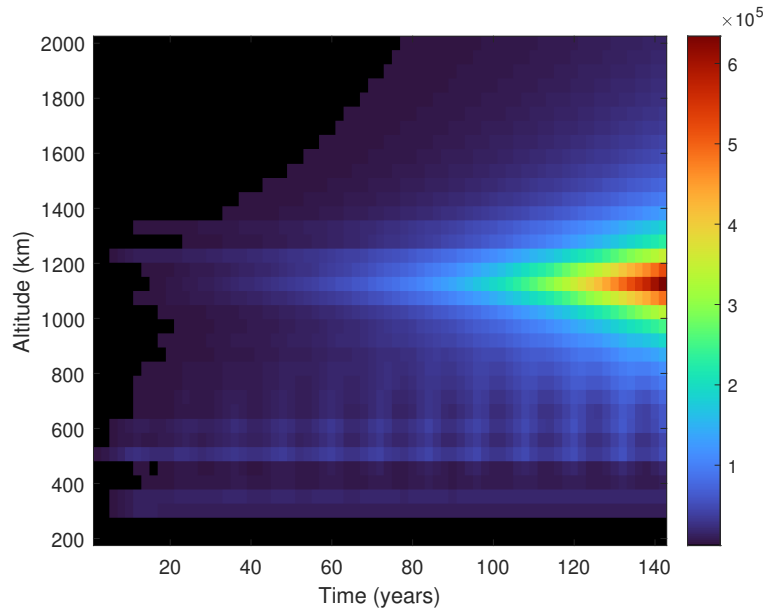
Figure 2-28: Total population per altitude for the all future megaconstellations case. Altitude is binned at 50 km and time is binned yearly.

the higher and lower altitudes. Figure 2-29 shows the comparison for each of the four cases, with the dashed line denoting the below 700 km population, and solid lines denoting the above 700 km population. Despite the much higher launches occuring below 700 km, the population below 700 km remain largely steady and low, while the higher altitudes grow continuously. This is pronounced even for the *No Future Launch* case. The lower altitude also exhibits population undulation due to the thermospheric expansion and contraction that follow the solar cycle. The comparison of only launching into lower altitude shells is explored in the next section.
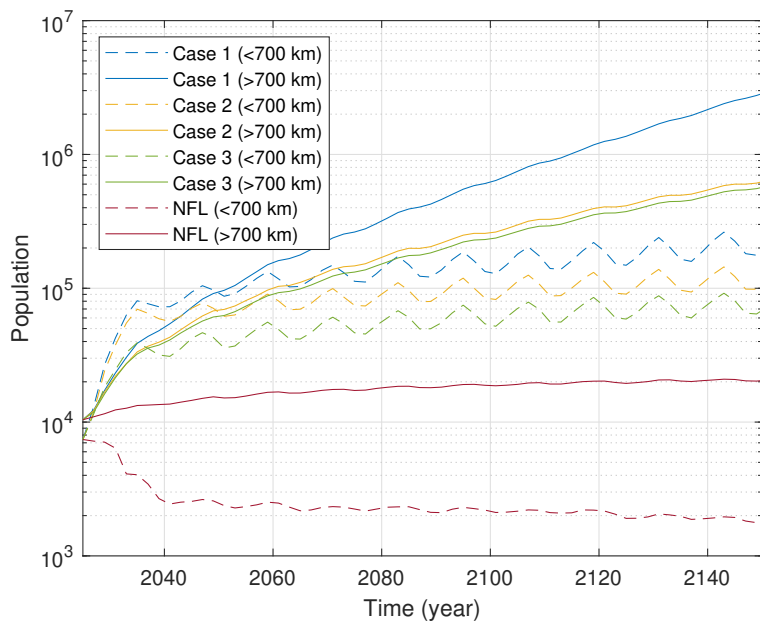
Figure 2-29: Total population below and above 700 km altitude for the four future launch cases

## 2.4.6 Megaconstellation case with limited altitudes

To see the effect of higher-altitude megaconstellation launches, a subset of the total megaconstellation case was launched and analyzed. Altitude limits of < 600 km (total 59336 operational), < 700 km (65408), < 900 km (66598) were chosen. The launch altitudes of the considered megaconstellations can be found in Fig. 2-25 and Table A.2. The same parameters as the previous section were used, other than the launched subset.



(a) Population             (b) Collisions
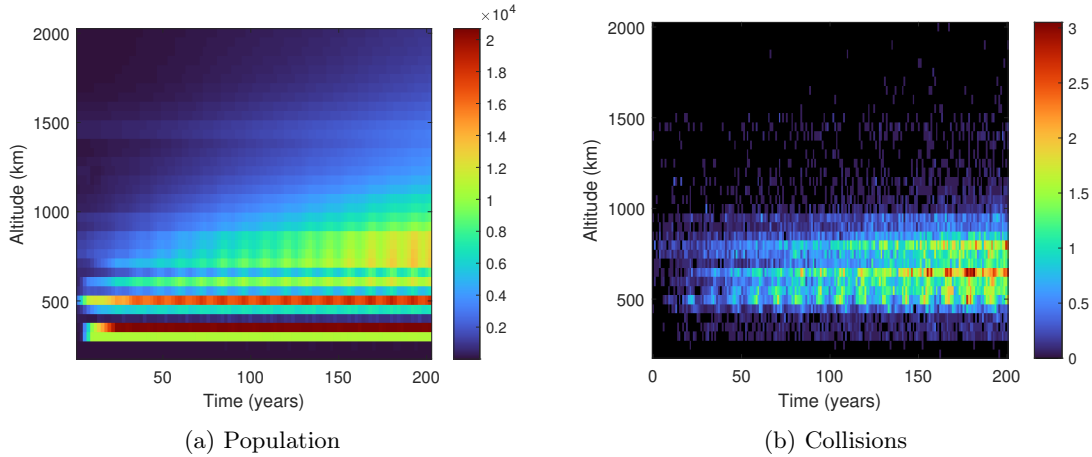
Figure 2-30: Megaconstellation launches limited to < 700 km

The collision and population statistics from the < 700 km constellation case is shown in Fig. 2-30. The comparisons involving the other cases are shown in the Appendix Figs. A.10 and A.11. It is clearly seen that the debris population growth and the collision rates are dominated by the higher orbits. Despite the much fewer of objects launched > 700 km, the total collision number across the 200 year simulation is more than halved. Note that for this analysis, the same PMD efficacy rate is used for all constellations. That is, the frequency of successful removal from the environment after the active payload's mission life is the same for all payloads of the same type no matter the altitude of the constellation. The more numerous population for the > 700 km launch scenario is due to the derelict satellites in higher orbits that remain in the environment for much longer due to lower atmospheric drag.

As a comparison, Fig. 2-31 shows the population when the > 700 km constellations are launched. Although the operational satellites for the > 700 km megaconstellations number around 1/4 of the < 700 km case, the population growth is much more pronounced. The reduced drag effect is clearly seen, with the debris population from the 800 km region persisting throughout the simulation duration. In Fig. 2-31(b), the dotted lines denote the uncontrolled objects, which includes derelict and debris objects. The solid line is the total number of objects. The difference between the solid and the dotted line is the controlled payload population, where Starlink's contribution to the current population from the initial population is clear around 500 km. This comparison shows the relative difference between the debris population and the payload population. The low altitude constellations are able to have a much higher payload to debris ratio, enjoying a lower debris environment due to the atmosphere while also lowering the collision avoidance operational burden.

The higher orbits, despite having the same PMD and $\alpha$ collision avoidance efficacy, must live with a much higher debris to payload ratio as the debris accumulates. This shows that debris mitigation efforts through higher PMD and effective collision avoidance will be crucial to maintaining a viable orbit regime for the higher altitudes.
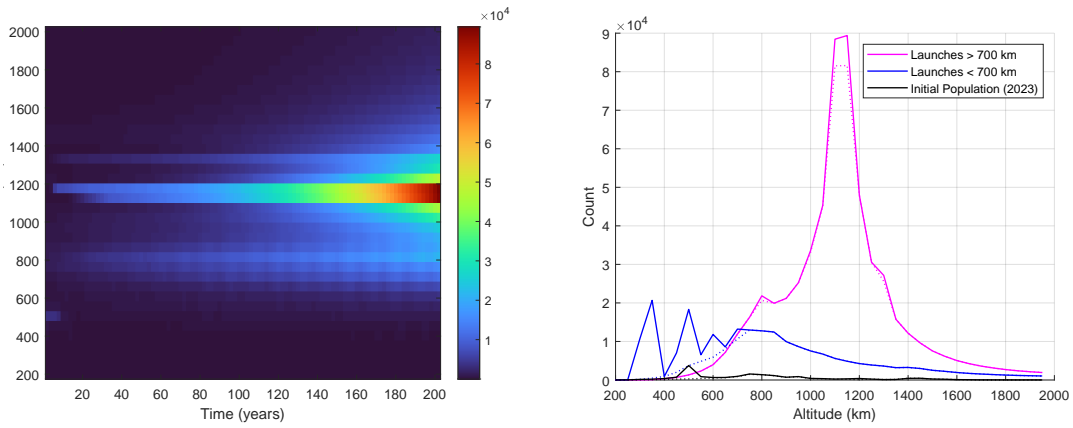


(a) Population

(b) Comparison of populations at 2223. Altitude is binned at 50 km

Figure 2-31: Megaconstellation launches limited to $> 700$ km

## 2.5 Conclusion

This chapter describes a novel Monte Carlo-based method to simulate the evolution of the LEO population. The tool is able to efficiently model the evolution of the orbital population characterized by dynamics such as launches, collisions, explosions, deorbit methods, and more. This Monte Carlo tool is flexible in its modeling fidelity with several options for the propagator, initial simulation population and launch profiles. A sampling-based collision model is used and its sensitivity to input parameters is explored. Statistical convergence is tested, and the output result has been validated against six other models in the literature with which MOCAT-MC shows good agreement. Historical look at the no-future launch cases shows that the LEO population without any new launches since 2000 may have continued to grow and has only accelerated with the increased population since then. A future launch case involving all megaconstellations filed with the ITU and FCC is explored, where the number of objects > 10 cm grows to tens of millions of objects. These results underscore the importance of a multitude of debris mitigation strategies that include international policies and technological solutions.

The simulation results from this section also show some important conclusions: the higher–altitude accumulation of orbital debris is much faster than that of the lower altitudes, and warrants careful planning. In addition, the accumulation of debris in the higher orbits is not only affected by payload launches into the lower altitudes; collisions in any orbital regime will deposit debris into any other orbital altitudes due to the $\Delta V$ imparted during the fragmentation event. Despite the much fewer megaconstellations planned at higher altitudes, their failure in PMD or CAM will result in an outsized effect on orbital debris accumulation.

Limitations exist to the current MOCAT-MC model and the submodules. Future work will include the inclusion of other semianalytical propagators and other breakup models, along with sensitivity assessment of the use of different submodules and assumptions. Economic variables can be layered into the simulation as an on-line feedback mechanism. Gaming scenarios with multiple competing or cooperative actors can also be layered in with a different context for national and international policies.

# Chapter 3

# Effect of Lethal Non-Trackable Objects on Space Sustainability

## 3.1 Background

Our knowledge of the orbital objects in LEO is best understood for those objects that are measured reguarly. This usually means that the objects are tracked and have orbits attributed to them with some fidelity such that sensors are able to reacquire and constantly update the state. Characterization of such objects can be done using various phenomenologies such as multispectral imaging, radar imaging, and even passive RF tracking for objects that are emitting in the RF spectrum. Ever since the launch of Sputnik in 1957, the US government has led the effort to track orbital objects. The Millstone Hill radar under development for the planned Ballistic Missile Early Warning System (BMEWS) by Lincoln Laboratory in Massachusetts was the first U.S. radar to detect and track Sputnik 1.

Searching and tracking objects in orbit has historically been done using terrestrial active and passive sensors, such as radars and telescopes. Technological progress since then has expanded measurement methods to also include passive radio frequency (RF) and remote sensing from space. Due to the resources needed to keep custody of these objects, government entities such as the US Space Surveillance Network (SSN), the 18th Space Defense Squadron, and the European Space Operations Centre in ESA have traditionally tracked the RSOs. In the past couple of decades, a thriving commercial SSA sector has been introduced. The global space situational awareness market is projected to grow from $1.3 billion in 2022 to nearly $2 billion in 2028 within the US alone [6].

Although tracking intact payloads and rocket bodies in LEO has largely become routine, tracking small debris remains a challenge. Not only is detection itself difficult for small objects due to sensitivity limitations of the SSA sensors, the number of objects grows exponentially as the limit of detectable size gets smaller, which leads to difficulties with identifying the detected object to create a track and an orbit - an *association*
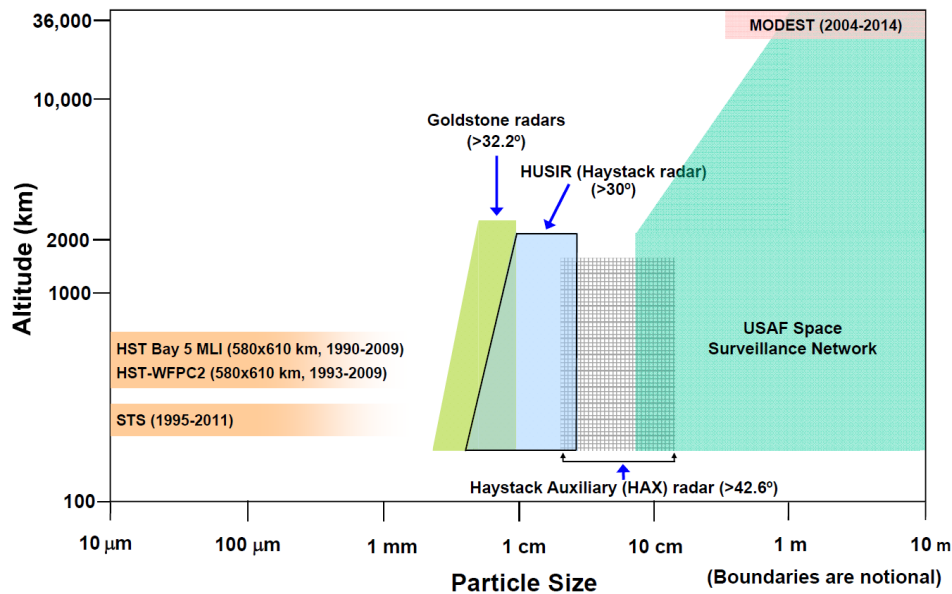
Figure 3-1: Measurement data used by the NASA ODPO to describe the orbital debris populations in the near-Earth space environment [65]

problem. The US Space Surveillance Network is understood to have orbital information for 10 cm and larger objects.

Tracking and keeping custody of small debris to keep an orbit may be difficult; however, routing measurements of the density of debris have been made over the years. For example, radar measurement data from the Haystack Ultra-wideband Satellite Imaging Radar (HUSIR) is provided to the NASA Orbital Debris Program Office for measurements of objects as small as 3 mm [110]. The radar operates in a "beam-park" mode with a fixed elevation and azimuth pointing direction to obtain the number of objects, RCS and doppler measurement of the objects that cross through the field of view. This provides a fixed detection volume that simplifies calculations of the debris flux, or number of objects detected per unit area, per unit time. The effects of collision events and ASAT tests have been seen by measuring the statistics of the objects.

In situ measurements of the small debris population have been made in LEO as well. Debris as small as several micrometers in size have been measured by impact craters into space-exposed materials from satellites and specific missions with sensors to measure on-orbit debris impacts. Although specific orbital information for individual debris is difficult to measure, the statistical distribution of objects with respect to their orbital parameters and physical characteristics can be estimated. The Long-Duration Exposure Facility was launched in April 1984 by the Space Shuttle mission STS-41-C into an altitude of about 480 km, where it sampled the LEO environment for more than 2000 days. The LDEF mission showed that by 1990 there was a large amount of debris in the LEO environment with a population following the power law and showed the large amount of debris that eludes current sensor technology for tracking [103, 32]. The solar arrays replaced on

70

the Hubble Space Telescope (HST) Service Missions SM-1 and SM-3B in 1993 and 2002, respectively, have provided the space community with solar arrays that have been exposed to the space environment at about 600 km for more than seven years. Other in-situ measurements have been conducted since then, including the Space Debris Sensor (SDS) currently mounted on the exterior of the International Space Station. The LDEF mission has sampled for the longest duration as well as sampling from a diverse set of altitudes, as seen in Fig. 3-2.
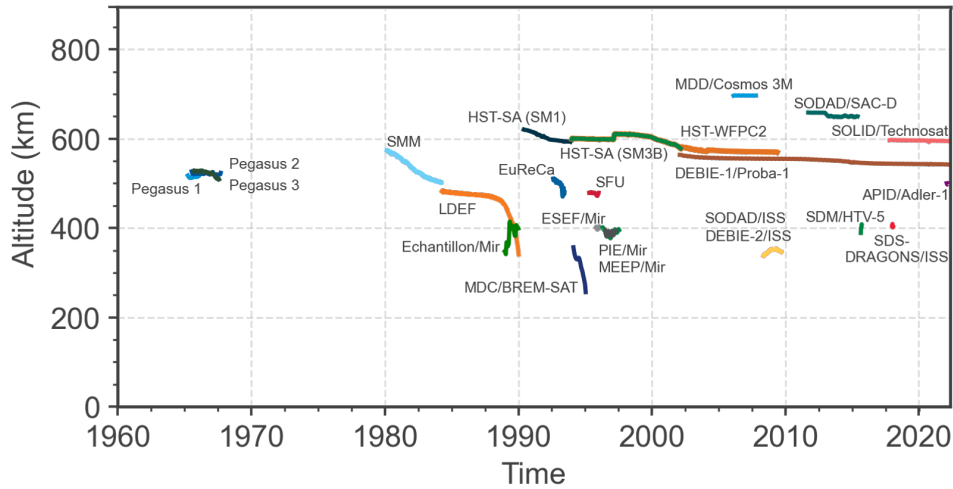


Figure 3-2: History of in-situ measurement missions for small debris [34]

Many models have been created using these data for the past and future LEO orbital debris environment, including NASA's ORDEM [102, 99] and ESA's MASTER [49]. The debris population from these databases for some initial simulation epoch can be used to seed the initial population with randomized orbits. The difficulty lies in the fact that for smaller object sizes, the number grows rapidly. ESA estimates that there are more than 1 million fragments between 1 and 10 cm, and around 130 million objects between 1 mm and 1 cm in orbit around Earth as of June 2023. Any impact with one of these objects threatens to at least impair the functioning of a working spacecraft, or at worst destroy it altogether, creating ever more debris. The computational power needed to simulate an environment with that many objects is difficult, and thus most MC models have limited analysis to > 10 cm objects, or run specific cases with smaller objects. Not only does the initial population need to be propagated, with a smaller size threshold for simulations, the debris generated from collisions will also produce objects down to that size.

## 3.2 Modeling the effect of Lethal Non-Trackable Objects

Lethal Non-Trackable Objects (LNT) are defined here as objects that are sufficiently small to not be reliably detected in a way that is actionable for collision avoidance maneuvers by the satellite operators and the payload. The LNT population is quickly populated from any simulation that allows small objects to be

created from collisions. With MOCAT-MC the LNT population below the 10 cm region can effectively be explored, as it is able to simulate millions of objects with ease as shown in Ch. 2.

**Collision Avoidance Maneuver Modeling**

In MOCAT-MC, the LNT population is defined as objects with $L_C < 10$ cm. The model takes into account $\alpha, \alpha_a$ terms that modify the probability of collision between an active payload and a nonactive object, and between two active payloads, respectively. These account for the efficacy of the collision avoidance maneuver (CAM), since the maneuver can be planned. Although this is a static value effective for all tracked objects, it is modified for LNTs whose orbital states are either not known, or are tracked with larger uncertainties.

The efficacy of CAMs against LNT objects is assumed to follow a logistic curve. With this modifier, the $\alpha$ term is modified such that $\alpha$ effectively becomes 1 as the radius of the nonactive object nears 0, effectively eliminating any reduction of the probability of collision. The modified $\alpha$ for LNT objects is as follows:

$$\alpha_{LNT} = \left(1 - \frac{1}{1 + \exp\left(-25(r_j - 0.3)\right)}\right)(1 - \alpha) + \alpha, \tag{3.1}$$

where $r_j$ is the radius of the non-active object and $\alpha$ is the original collision avoidance term. A range of $\alpha_{mod}$ is shown in Fig. 3-3 using Eq. 3.1 as the modifier. The $\alpha$ term is maintained for large objects and approaches 1 as the radius of the object decreases and evades detection.
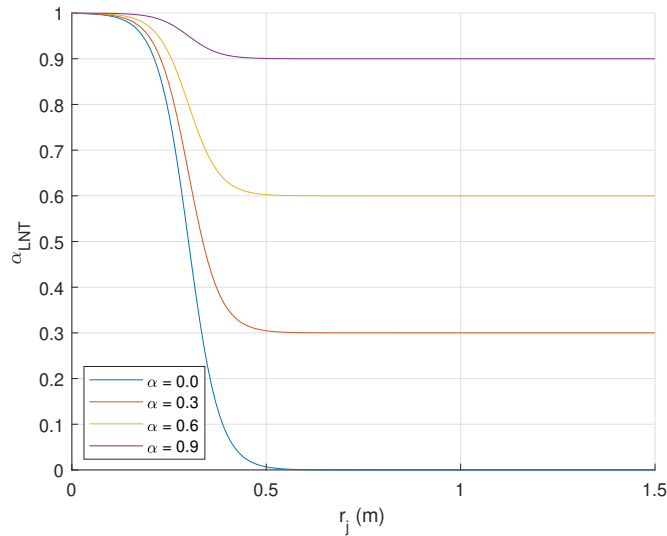


Figure 3-3: The collision avoidance efficacy term $\alpha_{LNT}$ for LNT objects for a range of baseline efficacy $\alpha$

Note that all payloads are assumed to be well-tracked; therefore, the $\alpha_a$ term is not modified. At the time of writing, two maneuverable and controlled active satellites have never collided so effectively that $\alpha_a = 0$.

### 3.2.1 Henize factor for incomplete measurements

The Henize factor has been used in the literature to estimate the true number of objects at certain altitudes. This attempts to inflate the number of smaller objects, noting that SSA sensors do not have a sharp sensitivity cutoff and the number of small tracked objects may not be representative.

In this method, $d_{tr}$ is defined as the trackable diameter computed for an object at altitude $H$, which is assumed to be the perigee altitude of the parent object $h_p = H$. To determine the trackable diameter, an empirical formula is used

$$
d_{tr} = \begin{cases}
8.9 \text{ cm} & H \leq 620 \text{ km} \\
1.0 \text{ cm} \cdot 10^{-0.736748+0.604\ \log(H)} & 620 \text{ km} < H \leq 1300 \text{ km} \\
1.0 \text{ cm} \cdot 10^{-4.417+1.8186\ \log(H)} & 1300 \text{ km} < H \leq 3800 \text{ km} \\
1.0 \text{ m} & H > 3800 \text{ km}
\end{cases}
\tag{3.2}
$$

The true number of objects larger than the trackable diameter is computed applying a correction through the Henize factor $f_{Hz}$ which is computed as

$$
f_{Hz} = \begin{cases}
\sqrt{10^{e^{\left(-\frac{\log_{10}(\hat{d}_{tr})-0.78}{0.637}\right)^2}}} & \text{if } d_{tr} > 10^{0.78} \text{ cm} \\
\sqrt{10} & \text{otherwise}
\end{cases}
\tag{3.3}
$$

The Henize factor considers the lack of sensor availability to track all the debris generated from a fragmentation event. In fact, usually only a part of the debris could be observed; thus, the Henize factor solves for the incompleteness of the radar catalog for objects larger than a given diameter [49]. The resulting value $n_f$ can now be considered as the true number of objects larger than $d_{tr}$ generated by an event on an orbit with perigee altitude $H$.

## 3.3 Validation with ADEPT dataset

Aerospace Corpporation's evolutionary model called Aerospace Debris Environment Projection Tool (ADEPT) [47] is used as a benchmark for the validation of MOCAT-MC's LNT performance. ADEPT is capable of propagating objects between LEO and GEO, and uses the Orbit Crossing method for collision calculation and an internal fragmentation model called IMPACT [130]. ADEPT is also able to group homogeneous objects in similar orbits into one object with some weighting factor to represent multiple objects, sometimes numbering in the thousands. This method allows ADEPT to propagate one representative object instead of having to do so for all the represented objects. An initial population is given (*popZero*), and the Future Launch Model (*FLM*) can be specified with a mix of Continuously Replenishing Constellations (*CRC*), non-replenishing constellations (*Non-CRCs*), and Future Constellation Models (*FCM*). All objects simulated in ADEPT are defined by 16 attributes, as described in Table 3.1.

Table 3.1: Definition of parameters for each orbital object in ADEPT

| Column | 1 | 2 | 3-8 | 9 | 10 |
|---|---|---|---|---|---|
| Description | ID | Start epoch | $\bar{a}, \bar{e}, \bar{i}, \bar{\Omega}, \bar{\omega}, \bar{M}$ | End epoch | Object type |
| Column | 11 | 12-13 | 14 | 15 | 16 |
| Description | Disposal flag | Stationkeeping flag | Area and mass | Diameter | Weighting |

"Historical" PMD success rates were used, where PMD = 90% for CRC LEO, GEO, MEO, and LLC satellites and PMD = 70% for nonCRC LEO satellites. A successful PMD results in the object being removed from the environment; whereas a failed PMD would leave it in the simulation. Operational satellites were assumed to avoid collisions with >10cm fragments with 100% efficacy.

A dataset of input and output populations and statistics was obtained for the use of MOCAT-MC validation. The simulation for the dataset had a starting epoch of December 1, 2022, and the outputs for 100 runs were provided. The initial population given had 399,399 objects, and the operational payload count was steady at 18,006 objects. In the given ADEPT dataset, many objects could be represented by one object where the weighting is > 1. For example, after a fragmentation event, ADEPT's collision model IMPACT creates a few representative object sizes with multiple weighting factors that span down to 2 cm objects. This weighting factor can also be a decimal. In conversion to MOCAT simulation, all of these objects are independently represented with a randomized mean anomaly. For the cases of non-integer weighting factors, a random value is used between the floor and the ceiling of that factor. The SBM for MOCAT was run with $L_C = 2$ cm.

The comparison of the initial population reduction between the two models for this scenario is shown in Fig. 3-4. For MOCAT, the mean of 10 runs is shown for all the results. This shows good agreement between the two models, which validates the propagator and the drag model used in MOCAT-MC. The waviness of the population is due to the time-varying atmospheric density, and the phasing difference between the two

(a) Initial population
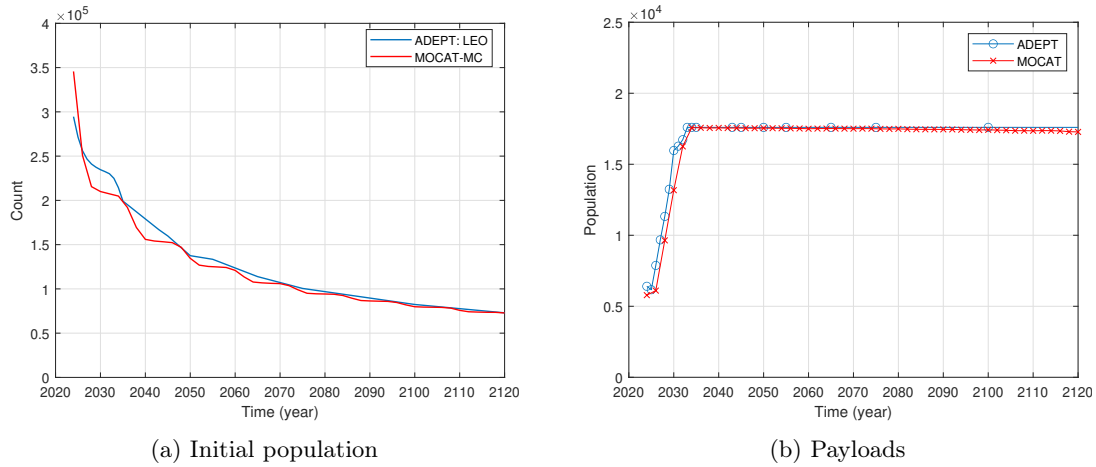
(b) Payloads

Figure 3-4: Population comparison for ADEPT vs MOCAT-MC.

models. The active payload count is also shown in the figure, which shows good agreement for the launch and PMD model. The launch traffic varied between 5500 and 8000 objects per year after 2030, and included payloads (controlled and uncontrolled), rocket bodies, and debris.

This validation exercise shows that MOCAT and ADEPT agree well in the propagation module, atmospheric model, and launch model even for LNT objects down to the 2 cm objects.

## 3.4 Results with Lethal Non-Trackable Objects

### 3.4.1 No Future Launch scenarios

The *No Future Launch* case described in the previous chapter is run while allowing for LNT debris to exist. The 3cm cases are shown here, while the details of the 1 and 5cm limits can be found in the Appendix.

Even if objects below 10 cm did not interact with any other objects, the number of objects in that region produced by collisions would show a higher number compared to a scenario that allows only objects > of 10 cm. Of note is the number of collisions that grow with the introduction of LNTs. Fig. 3-5 shows the difference in the cumulative number of collisions between two independent sets of scenarios: one allowing objects to exist above 10 cm and another for objects above 3 cm. For both of these cases, the previous scenario *No Future Launch* is assumed and simulated for 200 years. Each of the thinner lines represents one of the 50 MC runs for that scenario, while the thicker line shows the mean value of those runs. It can be seen that the number of collisions continues to grow even without any new launches into the LEO environment. For the > 3 cm case, the number of collisions increases faster. Since collisions beget more collisions, the slopes of these lines have an exponential growth factor for the population.

Although it is expected that there are more collisions with a population that has more objects, an analysis of the object types involved in the collisions along with relative frequencies is needed. For example, with the addition of 3-10 cm objects, the > 3 cm scenario will have many more LNT-on-LNT collisions, which does not directly affect the intact RSOs. The collision probability is affected by the combined cross-sectional area of the two objects as described in Eq. 4.9, and thus a given pair of LNT objects will not collide as frequently as it would against another larger object.



(a) Initial and final population size distribution        (b) Cumulative collisions
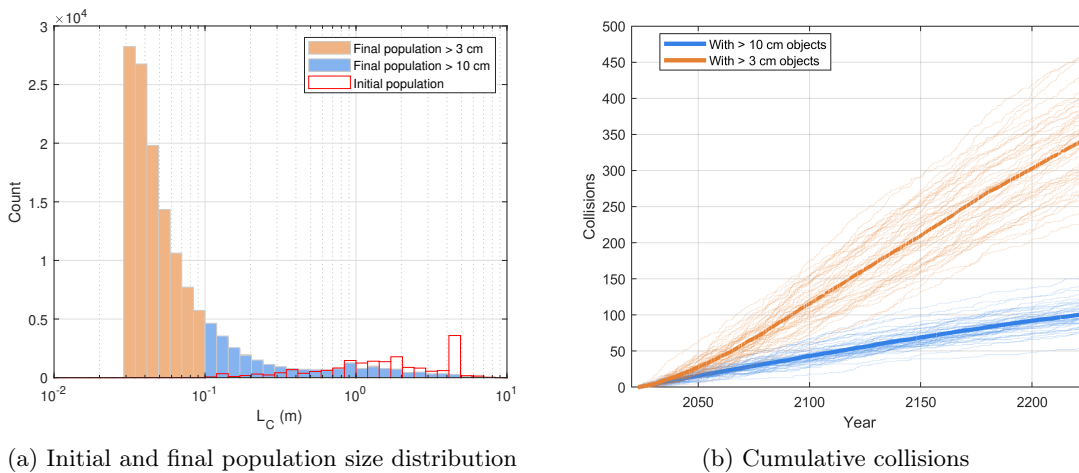
Figure 3-5: No Future Launches scenarios for $L_C = 3$ cm and 10 cm

Fig. 3-5 compares the distribution of the final population at the end of each of the scenarios. The red outline also shows the initial population distribution. Since both are for the *No Future Launch* cases, the initial population's larger objects are slowly deorbited or removed due to collision attrition. The small-object

population grows quickly over the 200-year simulation as the debris generated from these collisions, especially below the 10 cm region. It is notable that some bin sizes have fewer population in the $> 3$ cm case compared to the $> 10$cm case, especially closer to 10 cm, as these objects also undergo fragmentation events from smaller objects for the $> 3$ cm scenarios. In the $> 10$cm scenario, these objects would not collide with other smaller objects simply because they do not exist in the scenario. This example shows that lowering the characteristic length limit for a simulation would replace the population of trackable objects with LNTs. Thus, limiting the simulations to only trackable objects gives an incomplete understanding of the LEO environment. It is also shown here that due to the interaction between the LNTs and smaller-sized objects, a simulation run with LNTs that has been cropped to show the non-LNT objects is not equivalent to a simulation run without considering LNTs.



(a) Initial and final population per altitude

(b) Population evolution
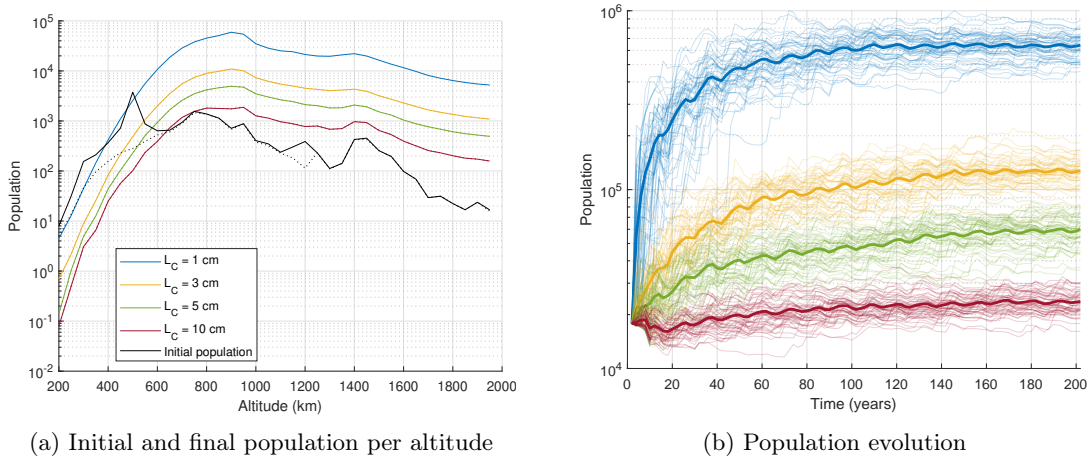
Figure 3-6: Total population count with no future launches over a 200-year span for various minimum LNT sizes ($L_C$). The altitude bins are 50 km.

### 3.4.2 Megaconstellation launches

The scenario with launches of future megaconstellations described in Chap. 2 is repeated. The scenarios with a subset of future megaconstellation launches are explored here for the varying levels of $L_C$. PMD success rates were derived from the historical rates given by ESA, with 40% for active (non-constellation) payloads, 55% for rocket bodies, and 90% for constellation satellites. Collision avoidance efficacy was chosen to be $\alpha = 0.01$ for actively controlled satellites, while all other cases with two active satellites were set at $\alpha_a = \alpha_{inter} = \alpha_{intra} = 0$.

The launch scenario considers all $< 700$ km constellations that total 65,408 operational constellation satellites. The launch traffic is run with $L_C = 0.2, 0.5, 0.7, 1, 3$ and $10$ cm. The initial epoch is January 1 2023 with a scenario duration of 200 years. For each of the $L_C$ values, 20 MC simulations are run. With smaller $L_C$, the cumulative number of objects per collision increases exponentially following the NASA SBM. Similarly, in this scenario, the number of objects grows as the population in the simulation consists of smaller

objects. The mean values of the MC simulations for each $L_C$ scenario are shown in Fig. 3-7. Figure 3-8 shows the population per altitude for $L_C = 2$ mm and 7 cm. The $L_C = 7$ cm case clearly shows each of the megaconstellation launches, as the vast majority of the objects are constellation objects. Although no launches are made to $> 700$ km altitudes in this scenario, higher altitudes also show an increase in population. This is due to the energy imparted to each debris object during a collision, which reduces and increases some of the fragments. With $L_C = 2$ mm, the smaller debris objects are tracked, which are much more numerous compared to the consetllation objects. The increase in the higher altitudes is shown more clearly and shows up earlier than in the case where smaller objects are omitted. The atmospheric sink effect is also clearly shown with an orders of magnitude difference in the debris population between high and low solar activity periods for lower altitudes.
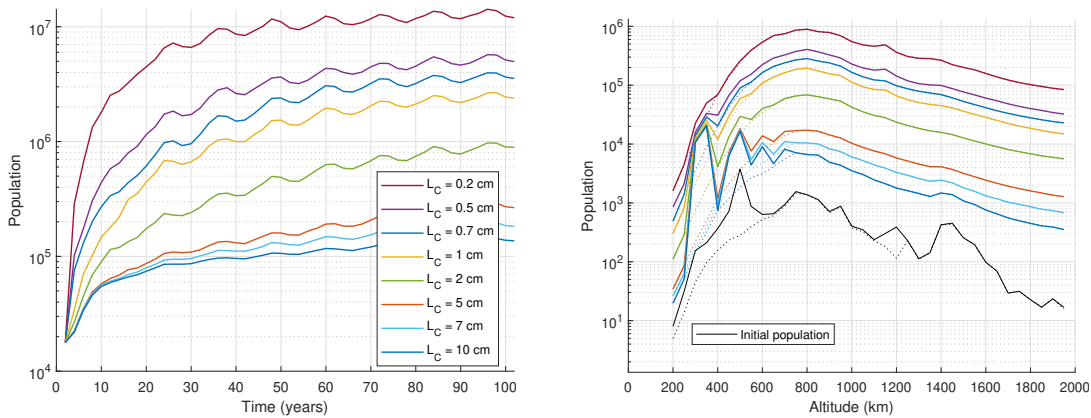


(a) Total population evolution for first 100 years

(b) Initial and final population per altitude. Dotted lines represent all uncontrolled objects.

Figure 3-7: The total population count with megaconstellation launches limited to $< 700$ km over a 200-year span for simulations with $L_C$ between 2 mm and 10 cm. The altitude bins are 50 km.
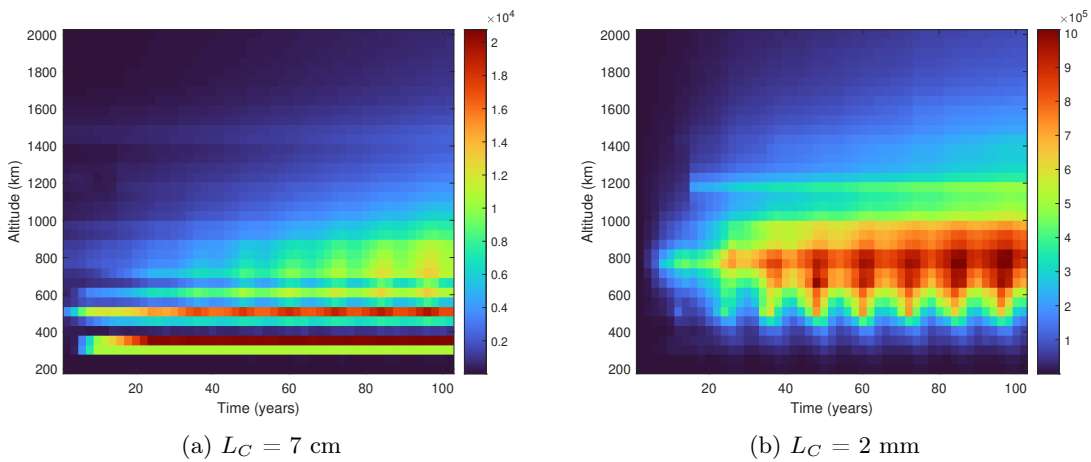


(a) $L_C = 7$ cm

(b) $L_C = 2$ mm

Figure 3-8: Population growth per altitude with megaconstellations launches limited to $< 700$ km over a 200-year span for various LNT sizes ($L_C$). Time binned at 2 years and altitude binned at 50 km.

The catastrophic and total collision statistics for the three cases are shown in Fig. 3-9, where several

conclusions can be drawn. The catastrophic collisions show that there are more total collisions with the inclusion of LNTs, as expected. However, the number of catastrophic collisions increases much more slowly as the minimum size of the object decreases. For most altitudes, the catastrophic collision rates are similar. The altitude with the greatest difference is around 800 km, where the $L_C = 0.2$ cm and the $L_C = 10$ cm cases differ by approximately a factor of 2. This is also despite the fact that launches are limited to altitudes $< 700$ km, with the highest concentration around 350 km and 550 km as shown by the launch rate by altitude in Fig. 2-25. Note that the number of catastrophic collisions is much fewer compared to the number of non-catastrophic collisions for all $L_C$, but unlike the catastrophic collision rate, the non-catastrophic collision rate increases much more rapidly with smaller $L_C$. Orders of magnitude difference is seen in the total number of collisions.



(a) Catastrophic collisions

(b) All collisions

Figure 3-9: Cumulative number of collisions with megaconstellations launches limited to $< 700$ km over a 200-year span for a range of $L_C$. Altitude is binned at 50 km.

The NASA SBM categorizes a collision as catastrophic or non-catastrophic with a simple specific energy threshold as described in Eq. 1.2. For a typical collision geometry with $v_{imp} \approx 11$ km/s, this specific energy threshold is reached when the ratio of the two masses is greater than $\approx 1500$:1. Therefore, for a catastrophic collision to occur given an LEO payload mass, the colliding object must have some minimum mass. This means that the LNTs generally only produce noncatastrophic collisions, and the cascading effect of on-orbit collisions is reduced. This effect is more clearly seen when the collision energy histogram is shown for a range of $L_C$, as shown in Fig. 3-10. In this figure, the collision types are divided into three groups: object vs. object, object vs. debris, and debris vs. debris. The object here is defined as all intact objects, which includes derelict and rocket body objects. Active payloads are not represented in these collisions as $\alpha_a = 0$ for these simulations. Debris is defined as all other objects. The red line denotes the 40 J/g threshold for catastrophic collision, as defined by the NASA SBM. As shown before, smaller $L_C$ simulations show more collisions, and the collision rate for non-catastrophic collisions grows much more quickly. When simulations only consider objects greater than 10 cm, the collision rate between noncatastrophic and catastrophic collisions may seem comparable, but a higher fidelity simulation shows that the number of noncatastrophic collisions may be

much higher and is sensitive to the $L_C$ considered in the simulation.



(a) $L_C = 10$ cm        (b) $L_C = 1$ cm        (c) $L_C = 0.2$ cm
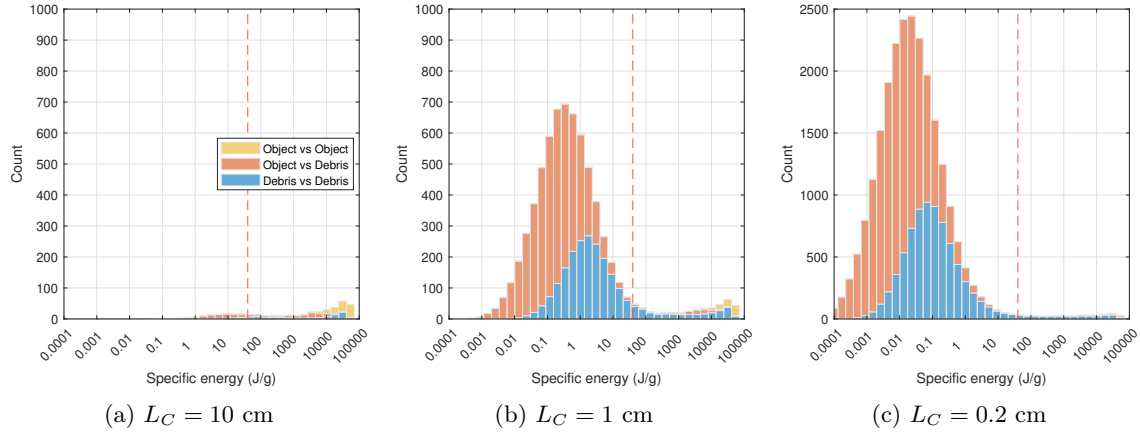
Figure 3-10: Histogram of the specific energy of all collisions for megaconstellation launches $< 700$ km for a range of $L_C$. Each scenario is an average value of 20 MC runs of a 100-year simulation. The red line denotes the $\tilde{E}_p^* = 40$ J/g threshold.

The distinct difference in the peaks of the object vs debris and debris vs debris collision energy is explained by the definition of the specific energy. The specific energy in a collision is soley determined by the impact velocity and the ratio of masses between the two parent objects. The specific energy of a collision between two identical masses – whether for a pair of 10 g debris or a pair of 1000 kg payload – yields the same specific energy. The peaks of the histograms therefore correspond to the ratio of the collision masses when that pair of objects collide. Intact objects such as payloads, derelicts and rocket bodies tend to be much more massive than debris objects. This results in a much lower specific energy of collisions between an intact object and a debris object than that of an object-on-object collision. This phenomena is also seen by the peak of the debris-on-debris collisions reducing in its specific energy as $L_C$ is reduced – there are far more collisions between two unequal masses within the debris class as smaller debris are simulated in an MC environment. $L_C = 10$ cm on average had 316.7 catastrophic collisions out of 409.9 total collisions, $L_C = 1$ cm had 480.4 of 6760.0, and $L_C = 0.2$ cm had 405.1 of 23773.1 collisions that were catastrophic. This relationship is summarized in Fig. 3-11. A more realistic simulation allowing for simulations against

Note that while it is true that a catastrophic collision would produce more objects compared to a non-catastrophic collision between the same pair of objects, not all of the catastrophic collisions shown in these histograms would necessarily produce more debris than the non-catastrophic collision. The number of debris is ultimately determined by the masses of the parent objects, and an catastrophic collision betwen two objects would produce more debris than one between two debris. Consequently, it is possible that a noncatastrophic collision between an object and debris yields more debris than a catastrophic debris-on-debris collision. As a comparison, a 50 g golf ball hit at 42 m/s will yield 44 Joules. Such golf ball hitting another stationary golf ball would produce a specific energy of around 0.9 J/g.
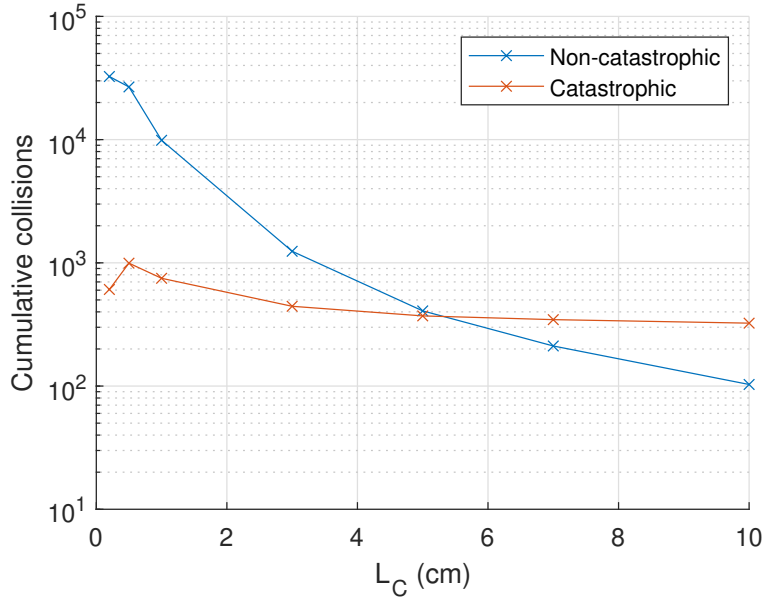
Figure 3-11: Cumulative number of collision for the 700 km megaconstellation launch case after 100 years for $L_C$ values from 0.2 cm to 10 cm

### 3.4.3 Effect of improved PMD

The effect of improved PMD is explored for the various $L_C$ from in the previous section. The PMD failure rate has been halved, as indicated in Table 3.2.

Table 3.2: Historical and Improved PMD Rates

|  | Historical PMD [34] | Improved PMD |
| --- | --- | --- |
| Active (non-constellation) | 40% | 70% |
| Active (constellation) | 90% | 95% |
| Rocket Body | 55% | 77.5% |

Note that the vast majority of the launches in this scenario comprise constellation payloads. The reduction in the total orbital population due to this is shown in Fig. 3-12. Because the LNT population depends heavily on the number of collisions, there is a greater effect in controlling the LNT population with the reduction of derelict objects. The reduction in collision rate is also seen in Fig. 3-13. With the amount of derelict produced per year effectively halved, the number of catastrophic collisions for the altitudes with launches ($< 700$ km) is halved. This is seen for both the scenario with $L_C = 1$ cm and 10 cm. The effect on non-catastrophic collision is even greater, as the opportunity for debris-on-debris collision is also reduced. However, note that for any type of collision, improved PMD can only effectively reduce the collisions in the altitude regions where the launches occur. The altitude regions without launches do see some reduction due to the reduction in eccentric debris created from collisions. These findings are in line with the literature, where larger and higher objects seem to be the most polluting. [108, 127]
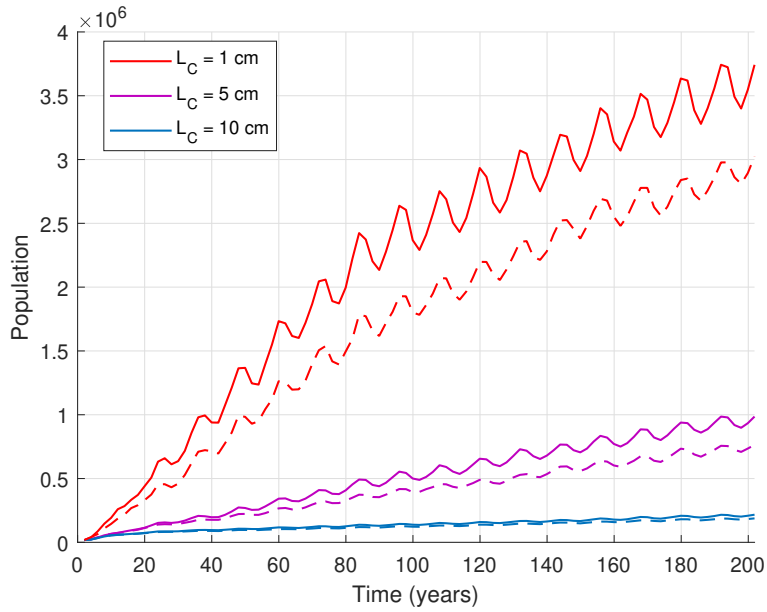
Figure 3-12: Total population count with megaconstellations launches limited to < 700 km over a 200-year span for various minimum LNT sizes and with increased PMD efficacy. Dotted lines represent the high PMD cases. The altitude bins are 50 km.
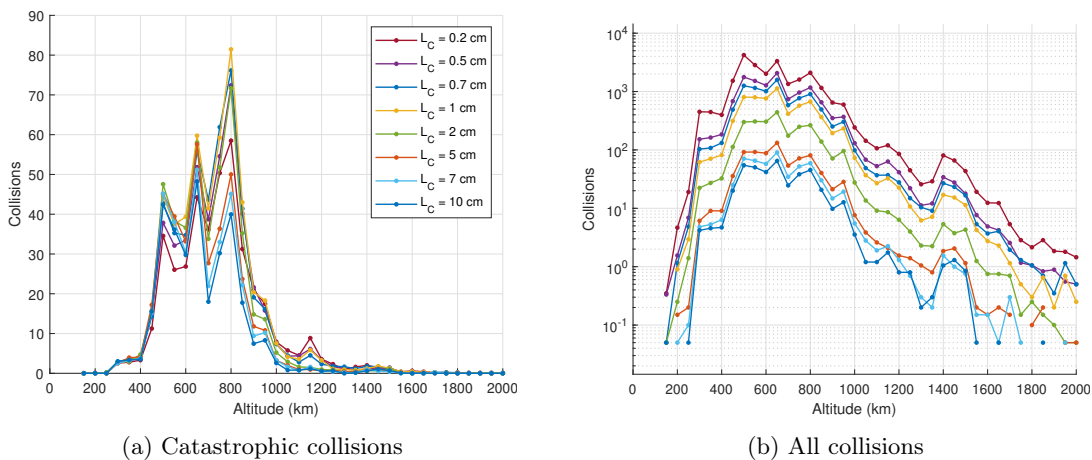


(a) Catastrophic collisions
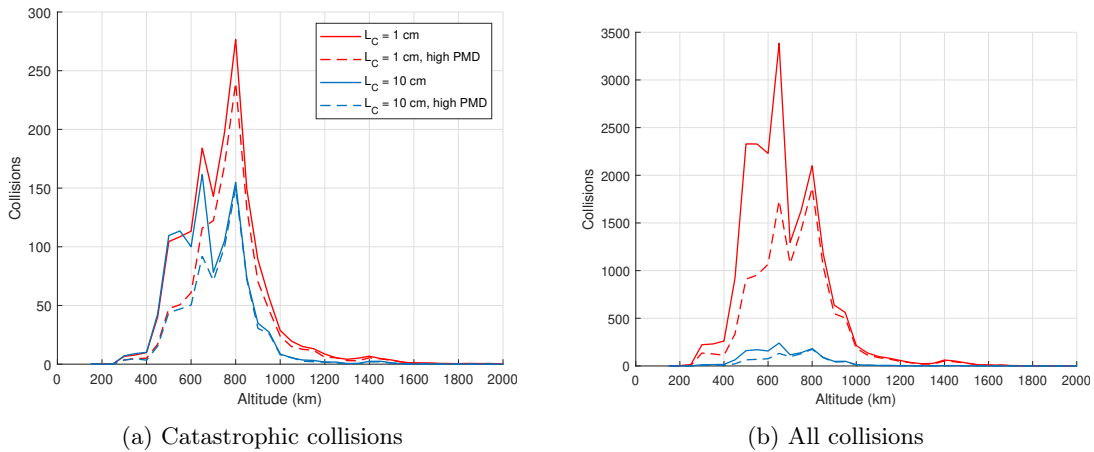
(b) All collisions

Figure 3-13: Cumulative number of collisions with megaconstellations launches limited to < 700 km over a 200-year span for various LNT sizes ($L_C$) and with improved PMD. Altitude is binned at 50 km.

(a) Historic PMD

(b) High PMD
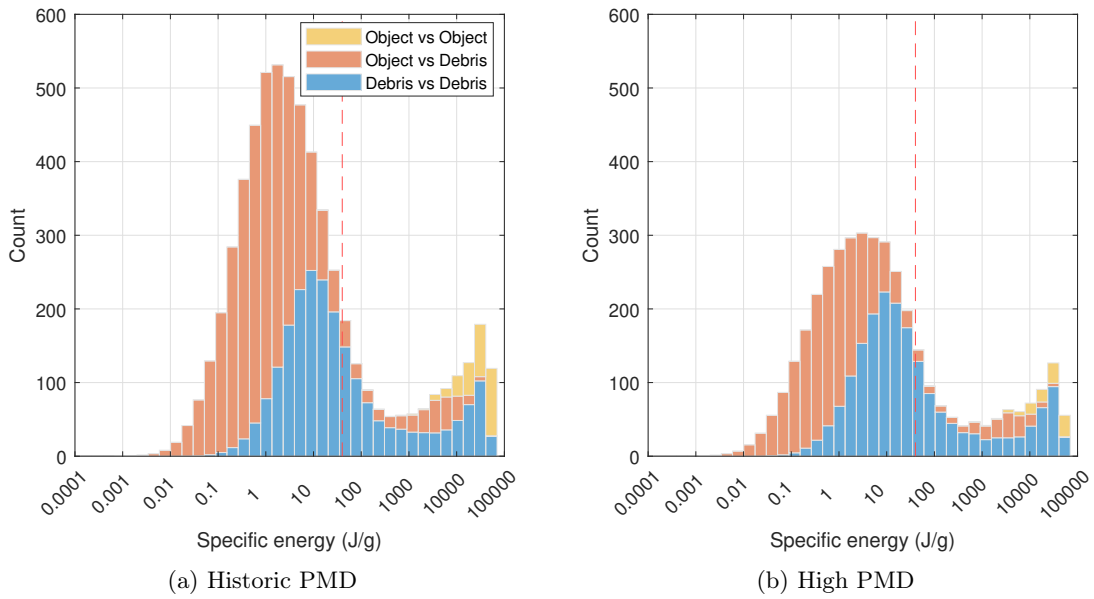
Figure 3-14: Effect of improved PMD on specific energy of collisions for limited to $< 700$ km megaconstellation launch scenario with $L_C = 3$ cm.



(a) Historic PMD

(b) High PMD
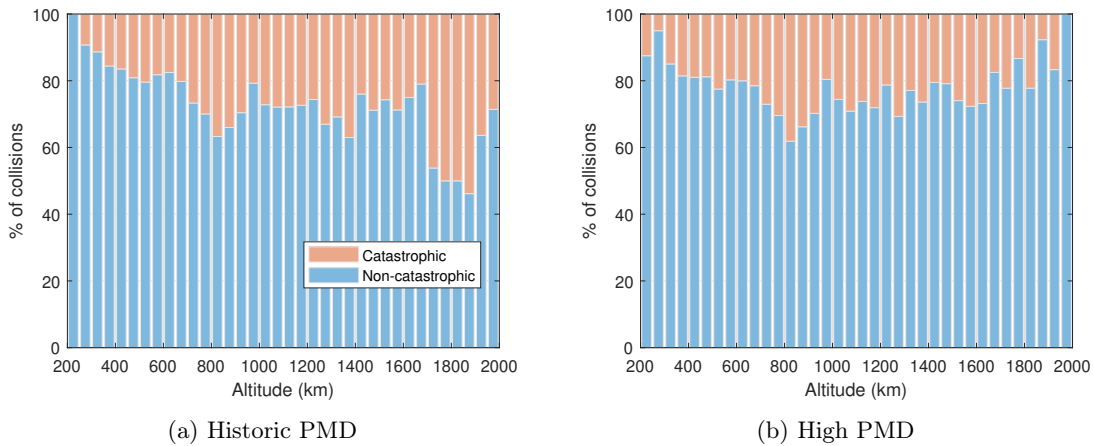
Figure 3-15: Effect of improved PMD on catastrophic collision rates of collisions for limited to $< 700$ km megaconstellation launch scenario with $L_C = 3$ cm.

## 3.5 Conclusion

Most orbital objects today are untracked or untrackable due to the limitations of the sensors. Attribution of these objects to specific launches or fragmentation events is difficult; however, ground-based sensors and in situ sensors on-orbit have been used to characterize the spatial density of debris into altitude and inclination. Even with such debris density models, the population of these models can easily reach millions of objects, making it difficult to use high-fidelity evolutionary models using Monte-Carlo-based methods. MOCAT-MC is able to efficiently model the LEO environment and thus able to model the numerous LNT objects.

It is shown through several scenarios that while the population of LNTs follows the power-law distribution, the number of catastrophic collisions does not grow linearly with the LNT population, as most of these objects do not collide with larger rocket bodies, derelict and payload objects with sufficient specific energy. However, the impact on payload survivability is pronounced, and the creation of derelict objects can cause secondary catastrophic collisions. Similarly to debris in 10 cm ranges, the LNT population also shows a steep dropoff in pouplation density below 500 km altitudes due to the atmospheric drag.

# Chapter 4

# Source-Sink Evolutionary Model Approach and Methodology

## 4.1 Introduction

There is a need to calculate long-term collision risk and debris population evolution without propagating all objects. One method to model population dynamics without propagating individual objects is through source-sink models, where the interaction between species is described by differential equations. These source-sink models are also known as evolutionary, predator-prey, and Lotka-Volterra models. A particle-in-box (PIB) assumption can be made within an enclosed domain within which the species can interact. An uncontrolled group of satellites is modeled by following the kinetic theory of gas within the enclosed domain. Several such models have been proposed in the literature, starting with [136] where the LEO domain is modeled as a series of spherical shells binned by altitude [117, 137, 112, 123, 75, 52, 138]. All use this spherical altitude discretization as a basis as most objects are circular and as objects' interaction with atmospheric drag and with other objects can be easily modeled in parallel. The LEO RSO population is often divided into three species: payloads, derelict satellites, and debris, though other or additional species may be used such as rocket bodies, untracked debris, etc.

Eccentricity can be modeled by binning the population and by a fractional contribution of the population to the corresponding shells. Not all models have eccentricity, although some have discretized eccentricity as well, such as in [56, 57] and the fractional contribution of each species to the corresponding altitude bins [129]. In CiELO the fragmentation cloud is described in terms of its spatial density and is propagated as a function of the semi-major axis ($a$) and eccentricity ($e$) [68, 69].

Although orbital propagation of states is circumvented in a PIB model, the interaction between the species and between the environment and the species must be modeled carefully and validated for an accurate model. The natural sink of the LEO environment is the atmospheric drag and the primary means to reduce the RSO

population. The lifetime of satellites may depend on the altitude, solar cycle, and ballistic coefficient of the orbiting object, and the binned altitude parameter captures the drag dynamics well.

The space debris problem has enormous political and economic implications, spanning topics such as equitable use of space, first movers advantage, tragedy of the commons, and game theory. PIB and SSEM models can be used to model such aspects. For example, economic analysis of LEO management was performed in [124], and the evaluation of the statistical model for adaptable debris control strategies was explored in [128, 82]. In [13], a game-theoretic view of cooperative and non-cooperative satellite launch policies as well as taxation schemes for sustainable developments was analyzed. The development of a higher-fidelity medium-term LEO population model will aid in such policy developments. The shared risk and responsibility of the debris problem was modeled and the level of cooperation in a competitive environment was assessed in [19, 1], and the consequences of an unfettered open access model to space were shown to result in the growth of runaway space debris [119]. MOCAT-SSEM aims to aid in such questions by leveraging its higher-fidelity space environment modeling and modularity in defining the species of interest.

## 4.2 LEO population and collision risk modeling

MOCAT-SSEM is a family of multi-bin, multi-species source sink models with multiple revisions and updates [26, 27, 85, 25, 51]. In MOCAT-3, the LEO RSO population is divided into three species: payload ($S$), derelict satellites ($D$), and debris ($N$). Derelict satellites represent intact satellites that fail to meet the post-mission disposal guidelines and remain on-orbit, but without the ability to perform collision avoidance maneuvers or station-keeping maneuvers. All objects of the same species have the same characteristics, and the domain of collision interaction is limited by altitude shells.

There are many unique aspects to the MIT Orbital Capacity Assessment Tool (MOCAT), which has been used to estimate LEO orbital capacity using stability criteria to maximize launch rate while keeping the environment stable and for varying degrees of payload failure rates [26, 114]. MOCAT-4S models the use of concentric specially phased orbital shells of "slots" for large constellations that inherently avoid collisions and was used to demonstrate a method to estimate benefits to space sustainability and spaceflight safety from slotting [85, 25]. MOCAT-4N subdivides debris into a trackable and lethal population of untracked debris and includes a radar model to model debris custody and detectability [27]. More recently, the model has been used to assess the possibility of using adaptive governance for safe space allocation [86], as well as to evaluate the economic impact of orbital debris and other policies [118].

Fundamentally, MOCAT-SSEM uses the PIB formulation, where the interactions between species are defined by ordinary differential equations. The base ordinary differential equations used in the 3-species model (typically for payload $S$, derelict satellites $D$ and lethal debris $N$) has been modified from the simple model in [52]. The modifications include the addition of altitude shells with drag interaction and the inclusion of multiple bins per species type. At the core, the governing dynamics is shown in Eq. 4.1.

$$\dot{S} = \lambda - \frac{S}{\Delta t} - \phi(\delta + \alpha)(N + D)S - \alpha_a \phi S^2, \tag{4.1}$$

$$\dot{D} = \frac{(1 - P)S}{\Delta t} + \phi \delta DS - \phi(N + D)D + \frac{n_+ v_+}{D_{hu}} + \frac{D v_-}{D_{hl}}, \tag{4.2}$$

$$\dot{N} = K_0 \phi(N + D)(\alpha S + D) + \alpha_a \phi S^2 + \phi N^2 - \frac{n_0 v_+}{D_{hu}} - \frac{n_0 v_+}{D_{hu}} + \frac{N_+ v_-}{D_{hl}}, \tag{4.3}$$

where $\lambda$ is the launch rate, $\Delta t$ is the average operational lifetime of a payload until post-mission disposal, $\phi$ is the characteristic length occupied by the satellite, $\alpha$ is the fraction of collisions that an active satellite fails to avoid, $\alpha_a$ is the fraction of collisions that an active satellite fails to avoid against another active satellite, $P$ is the successful post mission disposal rate, $v_+$ and $v_-$ are the flux from the shell above and below respectively, and $K_0$ is the number of fragments produced per collision.

Once the model is set and the species defined, the input variables to the model include $\lambda$ the launch rate and initial populations such as $S_0, D_0, N_0$ for each shell. Active debris removal methods would affect the terms $\dot{S}$ and $\dot{D}$ and to some extent $\dot{N}$ but are not modeled here. The atmospheric drag term is assumed to be constant per altitude shell according to the static CIRA-72 model. All objects are confined to be within each shell and interact only with those in that shell.

Similar to other SSEM models, MOCAT generalizes population parameters such as mass and diameter to some average value. For example, previous MOCAT iterations modeled payload and derelict populations as featuring an average size of 1.49 m and average mass of 223 kg as chosen in [129]. In this dissertation, we introduce new functionalities and parameters to expand the species definition and compare their contribution to the orbital capacity by analyzing 4 and 5-population models different properties from the original species. This will show how the discretization of parameters for each species can allow for modeling a range of parameters for a population species, especially for parameters that exhibit nonlinear effects on the population derivatives.

The dynamics for the SSEM from Eq. 4.1 can also be described by a system of ordinary differential equations as such:

$$\dot{\boldsymbol{P}} = \dot{\boldsymbol{\Lambda}} + \dot{\boldsymbol{C}}_{PMD} + \dot{\boldsymbol{F}} + \dot{\boldsymbol{C}} \tag{4.4}$$

where each term is meant to be function of time and altitude shell. For example, in a model with at least three species of payload ($S$), derelict ($D$), and debris ($N$) populations, the population vector can be described as $\boldsymbol{P}(h, t) = [S(h, t), D(h, t), N(h, t), ...]$ where $h$ is the shell number and $t$ describes the time index. For a model with a larger number of species, additional elements are appended to $\boldsymbol{P}(h, t)$.

$\dot{\boldsymbol{\Lambda}}$ is the launch rate in objects per year. For a scenario in which only the payload class has launches, $\dot{\boldsymbol{\Lambda}} = [\lambda_s, 0, 0, ...]$ where $\lambda_s$ is the yearly launch rate for the payload species.

$\dot{\boldsymbol{C}}_{PMD}$ describes the effect of post-mission disposal, which is the controlled process of removing an active satellite after its useful lifetime has ended. Most LEO satellites with enough propellant will have such a plan

to remove themselves from the space environment safely [34]. A failed PMD will contribute to the space debris problem, and the model will then categorize the payload $S$ as a derelict object $D$, and the rate at which this occurs is described by $\dot{\boldsymbol{C}}_{PMD}$. The PMD success rate is described by $P_M$ and the operational lifetime of the payload population is $\Delta t$ years. This results in the payload class increasing by $-\frac{S}{\Delta t}$ every time step, and the derelict class increasing by $\frac{1-P_M}{\Delta t} S$ every time step.

$\dot{\boldsymbol{F}}$ describes the population changes within a shell due to atmospheric drag and the consequent decay of the altitude. Active satellites are assumed not to be subject to the decay effects, since they can perform station-keeping maneuvers to remain in their orbit. Therefore, only derelicts and debris experience the effects of orbital decay.

$$\dot{\boldsymbol{F}} = \left[0, \dot{F}_{d,D}, \dot{F}_{d,N}, ...\right] \tag{4.5}$$

Indicating with $Q$ the number of objects belonging to a generic species, $\dot{F}_{d,Q}$ can be written as follows:

$$\dot{F}_{d,Q} = -\frac{Q_+ v_+}{d} + \frac{Qv}{d} \tag{4.6}$$

where $d$ is the thickness of the shell, and the subscript $+$ refers to the quantities related to the shell right above the current one. $v$ is the rate of change of the semi-major axis, expressed as:

$$v = -\rho B \sqrt{\mu R} \tag{4.7}$$

In Eq. (4.7), $\mu$ is the Earth gravitational parameter; $R$ is the radial distance of objects with respect to the center of the Earth (the assumption of near-circular orbits is here carried out, so that the semi-major axis corresponds to the radial distance); $B = c_D \frac{A}{m}$ is related to the ballistic coefficient with $c_D = 2.2$ [18]. $A$ is the area of the object, and $m$ is the mass of the object. $\rho$ is the atmospheric density, calculated as a static exponential model from CIRA-72 [3].

$$\rho = \rho_0 \exp\left(-\frac{h - h_0}{H}\right) \tag{4.8}$$

where $h$ is the altitude of the object, $\rho_0$ is the atmospheric density at reference altitude $h_0$, and $H$ is the atmospheric scale height [143]. $\dot{\boldsymbol{C}}$ describes the population change due to collision dynamics between species as

$$\dot{\boldsymbol{C}} = [\dot{C}_S, \dot{C}_D, \dot{C}_N, ...]. \tag{4.9}$$

The number of fragments generated by each type of collisions $n$ is derived from the NASA standard break-up model [55], where the collisions are classified as catastrophic and non-catastrophic depending on the released energy of the impact. The number of fragments caused by catastrophic and noncatastrophic collisions is denoted as $n_c$ and ($n_{nc}$ respectively. In MOCAT, collisions are considered catastrophic between intact objects (e.g. $S, D$) and noncatastrophic for collisions involving debris.

where $M_i, M_j$ are the mass of the object $i$ and $j$, respectively, $M_p$ is the mass of the lighter object, $L_C$ is

the characteristic length, and $v_{imp}$ is the impact velocity assumed to be for all collisions 10 km/s, which is accurate for the vast majority of collisions between two random LEO objects [129].

To organize the collision interactions and input parameters, a particular species' population changes due to collisions can be described with:

$$\dot{C}_i = \sum_{j=1}^{N_s} \Gamma_{ij} \phi_{ij} Q_i Q_j \tag{4.10}$$

where $N_s$ is the number of species considered (in this work $N_s = 4$), $i, j = 1, ..., N_s$ are the subscripts indicating each generic species $Q$, and $\Gamma_{ij}$ stores the various coefficients. A detailed description is found in [26, 27, 85] and is expanded in the following section.

The unique attributes of the MOCAT model are organized in the next section.

### 4.2.1  Inclusion of additional classical orbital elements

On long timescales, the evolution of a fragment cloud in LEO can be considered in three phases [107, 40, 69]. In the short term, the particles remain close to each other and form an ellipsoid. In the medium term, the different semimajor axis of the particles ($a$) induces a difference in anomaly and a ring is formed in the orbit. At this point, which usually occurs within several orbits, the true anomaly ($f$) about the original orbit becomes distributed. In the long term, the difference in $a$ induces differential precession due to the Earth's oblateness (J2 term) and distribution across the RAAN ($\Omega$) takes shape. Timescales on the order of months allow the fragments to be distributed over $\Omega$. At this point, the fragments' orbital elements can be well-defined by just the $a$ and $e$.

Since source-sink models allow only for average value per species to be used, continuous parameters that contribute significantly to the dynamics can be discretized and made into separate populations for a higher-fidelity model. While all source-sink models shown in the literature use spherical shells to discritize the altitudes of the LEO orbital domain, there are only a handful that model the different orbital elements such as eccentricity, inclination, ballistic coefficients, and more. Adding these other binned parameters would result in a much larger set of ODEs to be solved. Due to this trade-off between complexity and fidelity, a judicious set of parameters must be chosen for discretization. It should be noted that the source-sink models that assume circular orbits and discretization of altitudes limit the interaction of objects with other objects within the shell, greatly reducing the complexity of the ODEs. Allowing for interaction between shells with binned eccentricity or orbital plane orientation would quickly increase the computational demand.

A survey of the current LEO environment was performed to see the number of objects residing in different regimes. A TLE catalog from space-track.org in December 2021 was used to populate the initial conditions. Most LEO objects are near-circular, with 90% of objects having less than 10 km differences between their apogee and perigee. This can inform a suitable size for the altitude binning of the shells, as too large a shell may lead to discritization errors and less sensitivity, while too small may result in too few objects in each bin that results in over counting the effect of small samples [40].

### 4.2.2 Launch traffic

Currently, the largest satellite constellation operator is SpaceX with more than 5000 operational satellites in LEO. The company has implemented launch strategies for their satellites to combat the space debris problem by launching into lower orbits and then using propulsion to raise its orbit to operational altitude [132]. System failures often occur at orbit insertion, and any orbital insertion anomaly would allow the derelict satellites to reenter the atmosphere far more quickly than a direct injection into their target orbits. OneWeb also implements orbit raising maneuvers, launching into 450 km altitude, then each payload raises its orbit to the final orbit of 1200 km. These maneuvers are shown in Fig. 4-1. The initial launch altitude, parking orbits, and the final orbital insertion are shown. Starlink has a higher failure rate at 5% and the green plot shows the altitude decay for deployment rods (debris). Starlink also uses its parking orbit to distribute the satellites into a range of RAAN using nodal precession. OneWeb instead uses one launch for one batch of satellites in one plane.



(a) Starlink                    (b) OneWeb
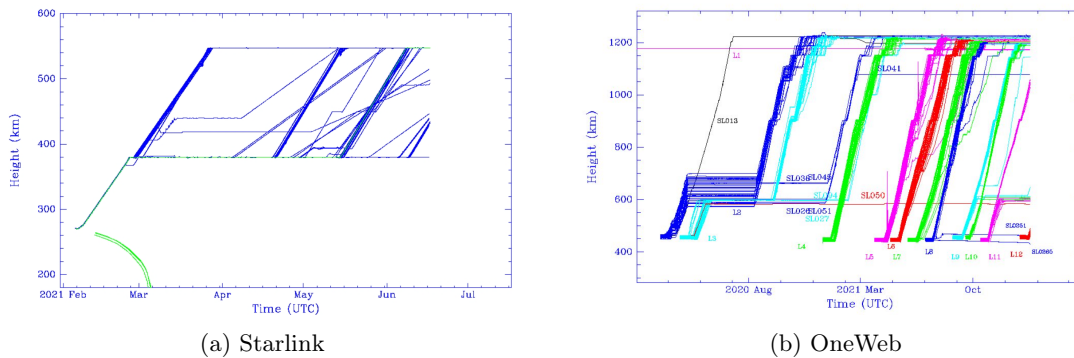
Figure 4-1: Example launch and transfer maneuver profiles [105] [104]

If the currently proposed megaconstellations are all successfully launched, the vast majority of the source of collisions will come from payloads, much of which will be in transit to the parking or operational orbit after launch or to a lower altitude for post-mission disposal. The additional flux between orbits caused by this traffic will be modeled via MOCAT. In addition, past launch rates and future planned constellations will model the realistic scenarios as the source of RSOs for the model.

### 4.2.3 Fragmentation model

Most LEO collisions occur in regions of high spatial density, around 800 and 1000 km altitudes, with collisions occurring with impact velocities of 10 km/s on average [89]. A range of collision velocity for two circular orbits with a difference in $\Omega$ and ß are shown in Fig. 4-2.

In MOCAT, the probability distribution function of the NASA SBM is sampled for the parameter value used for each species, as described in Eq. 2.6. According to the SBM, the imparted velocity on a sizable debris population often exceeds 10 km/s [55], which is enough $\Delta V$ to reach escape velocity or deorbit within an orbit due to its low perigee. Of note is the inclusion of non-self-interacting constellations such as satellites

(a) $v_c$ between two orbital planes        (b) $v_c$ for a range of $\Delta i$ and $\Delta \Omega$
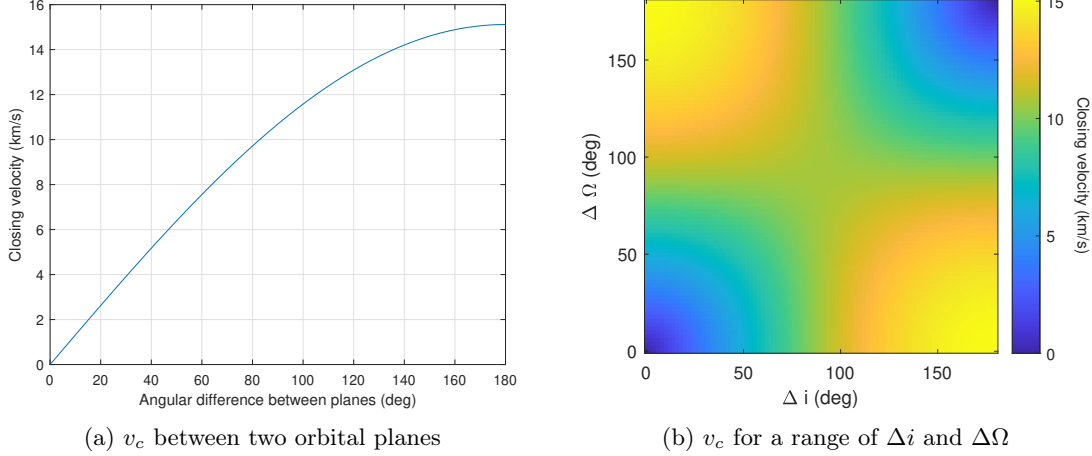
Figure 4-2: Collision velocity $v_c$ between two circular 500 km orbits

within a megaconstellation. However, $\alpha_a$ in Eq. 4.1 describes the COLA efficacy of a controlled payload and its chance of a collision against another controlled payload, a satellite as part of a megaconstellation would have a much lower probability of a collision against another satellite within the same constellation. As more LEO RSOs are a part of a bigger megaconstellation, the chance of collision should be reduced for those satellites in relation to other satellites, assuming coordination within the constellation is not an issue.

## 4.3    Differences between MC and SSEM approaches

There are many differences in how the SSEM method approaches modeling the future LEO population compared to how the MC method models the population, resulting in distinct pros and cons for both. This section aims to explain the differences between the two.

Fundamentally, the SSEM model simplifies the population of LEO objects into a few species. The population within a species is assumed to be homogeneous, and only the population of each species is propagated. Therefore, every object of the same species experiences the same dynamics and interacts with other species in the same manner. This allows one set of coefficients to describe the entire population's dynamics. The orbital environment can be divided into concentric altitude shells to keep account of each shell's population as well as limit the collision interaction of populations to within the shell. The model can then be propagated with a set of ODEs to describe the interaction between the population, as shown in Eq. 4.1.

There are three main interactions in the population dynamics: 1) launches into the system as the source, 2) drag forces acting on the objects ultimately leading to removal of the object from orbit, and 3) collision dynamics that creates more debris and removes the parent objects. MOCAT-SSEM does not assume inclusion of graveyard orbits for the LEO payloads.

The limitations of having one debris species in the SSEM are shown in Fig. 4-3, where the debris created from a collision is shown for a model using the MC model compared to the SSEM. The Gabbard plot of the

generated debris after a collision would contain eccentric orbits with a range of orbital periods; however, the simplified SSEM model assumes discretized circular altitudes as well as drag as the only force reducing the SMA of the objects.

Table 4.1: Summary of the fundamental differences between MC and SSEM models

|  | SSEM | MC |
|---|---|---|
| Propagated variable | Number of objects per Species $(S, D, N, ...)$ | Orbital element per object |
| Orbital states tracked per object or species | $a$ | $a, e, i, \Omega, n, p$ |
| Object parameters tracked | Mass, area, $C_D$, all uniform within each species | Mass, area, $C_D$ for individual objects |
| Collision event | Deterministic - average number determined by input | Stochastic |
| Collision domain for gas particle assumption | Spherical shells $(\approx 6 \times 10^{10} \text{ km}^3)$ | Cubes $(\approx 5 \times 10^5 \text{ km}^3)$ |
| Debris generation from collision | Deterministic - averages used | Stochastic, sampled at discrete collision event |
| Debris mass conservation | Unenforced - limited by species' parameters | Enforced |
| Atmospheric model | Static or time-varying | Static or time-varying |
| Drag dynamics | Objects are uniformly distributed within a shell, and some ratio move between shells determined by lifetime in shell | Drag force affect objects independently |
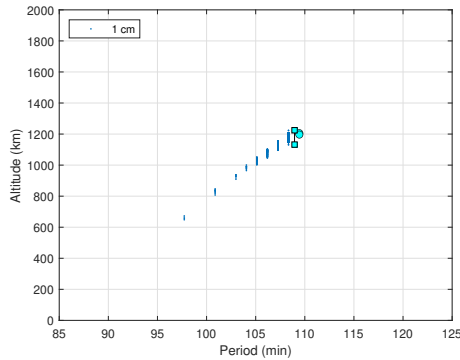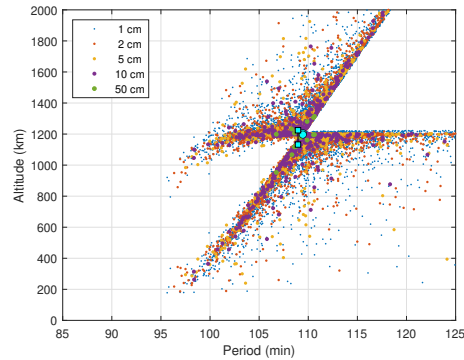


(a) 3 Species SSEM      (b) MC

Figure 4-3: Gabbard plot of debris 15 years after a collision

The computational resources required to run the SSEM and MC tools are shown in Fig. 4-4 for a range of 100-year simulations. For the SSEM case, the number of species determines the computataionl cost rather than the total population. The SSEM cases were all run with $10^6$ to $10^7$ poopulation. For the MC case, both the collision detection algorithm through Cube and the propagator scale as $\mathcal{O}(n)$, which is shown in the resulting computational duration required. Populations of 17,000 to $10^7$ were run on the Supercloud HPC system [120] with Intel Xeon Platinum 8260 processors. MOCAT-MC is created as a single-thread process – multiple threads and cores would allow for simultaneous runs of different MC simulations, but it will not inherently improve the run time for a particular MC simulation.



(a) MOCAT-SSEM  (b) MOCAT-MC
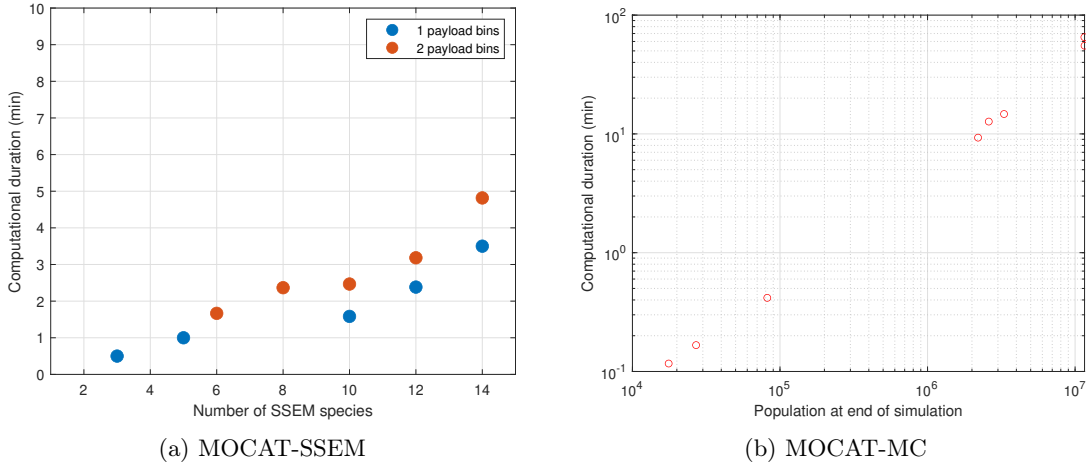
Figure 4-4: Compuatational requirement between MOCAT-SSEM and MOCAT-MC

## 4.4   Expanding the SSEM species parameters

The inherent architecture of SSEM models requires the use of a value associated with each parameter of a population, typically an average. For example, all payloads and derelict objects in the previous MOCAT models were generalized to objects with mass $m = 223$ kg and cross-sectional area $A = 1.741$ m$^2$ [26, 27, 85, 25]. The generalized approach of SSEM models allows for faster computation, though with lower fidelity, and the number of species is limited to capture the evolution of the population dynamics with limited computational cost. In reality, objects in space vary wildly in size and shape, and the effect of generalizing these into singular average values has not been studied. Debris objects in particular can range multiple orders of magnitude in size and number [130]. To address this gap, population parameters can be discretized and sampled at a higher rate rather than using an average value. One such parameter that has been discretized for all MOCAT models and most other SSEM models has been the altitude parameter, which is usually discretized into equi-spaced shells. This limits interaction between species to intrashell populations, which is more realistic, and it more closely models the vastly different role the atmospheric sink plays at each altitude. A finer discretization scale may seem to allow for higher fidelity simulations, though it has been shown that

after 30 or so LEO altitude bins, the fidelity gain is limited [129].



(a) Mass dependence on $\epsilon$      (b) Radius dependence on $\epsilon$      (c) AMR dependence on $\epsilon$
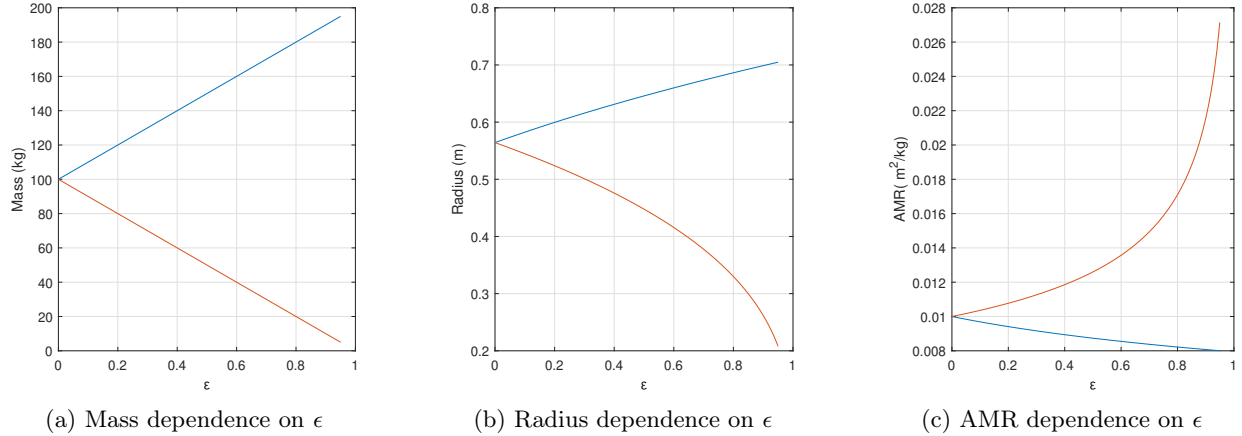
Figure 4-5: Notional physical attribute scaling $\epsilon$ for constant mean mass and density. Red line corresponds to the smaller mass, while the blue line signifies the larger mass.
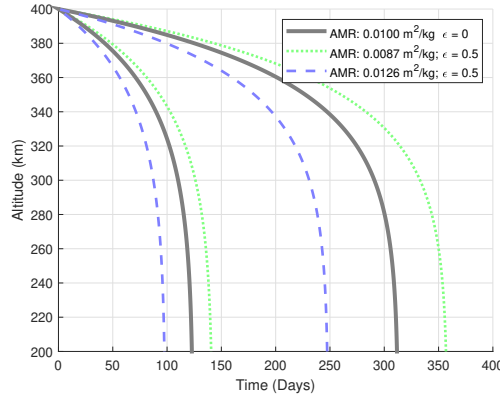


Figure 4-6: Decay of RSOs from 400 km circular altitude for F10.7 index between 70 to 200 sfu for various AMR and $\epsilon$ of 0 and 0.5. High solar flux results in greater atmospheric drag and a faster decay rate.

The effect of different area-to-mass ratio (AMR) on the deorbit duration for low to high solar activity periods ranging from 70 to 200 solar flux units is shown in Fig. 4-6. Density of the debris object is assumed to be constant, no matter how the population's mass is divided. This leads to a varied AMR for the different sizes of the object, as seen in the debris catalogs [49].

### 4.4.1    Expanded debris population for a 4-species model

The collision interaction between species contributes to the overall population via $\dot{C}$ in Eq. 4.4. The pairwise interactive term for the expanded 4-species model is broken down into each interactive element in Table 4.2. The debris population is divided into an additional population with a different physical characteristic – in this case, the mass of the object is additionally sampled.

The parameter $\epsilon$ is introduced to divide the population into two populations. In this model, we divide the mass of the original debris population into two species of differing mean masses, although the mass of

the ensemble debris population is fixed at $\bar{m}_{N0} = 0.64$ kg. For a given $\bar{m}_{N0}$, the $\epsilon$ parameter allows the mean of the two new species to grow apart until the smaller debris mass $m_M = 0$ and the larger debris mean mass $m_N = 2\bar{m}_{N0}$. There are non-linear effects to the orbital lifetime when the ensemble debris population's mean mass is kept constant, since $m \sim b^{1/3} \sim A^{2/3}$. While keeping the mean mass equivalent to a model with fewer species, the subdivided population will experience different population dynamics such as collision probability, atmospheric drag effects, collision fragmentation dynamics, etc. Rather than describing the entire debris population with one mass, this will allow a finer sampling, and its implications explored. The fragmentation dynamics is described in Eq. 2.7, where the number of noncatastrophic fragments is $n_{nc} \sim M^{0.75}$.

The 3-species model is expanded such that the debris species is further divided into a small and a large debris species ($N$ and $M$ respectively) to create a 4-species model. The only difference between the properties of the N and M classes is in the masses as described in Table 4.2. For $\epsilon = 0$, this 4-species model behaves identically to the 3-species model when the two debris populations are summed.
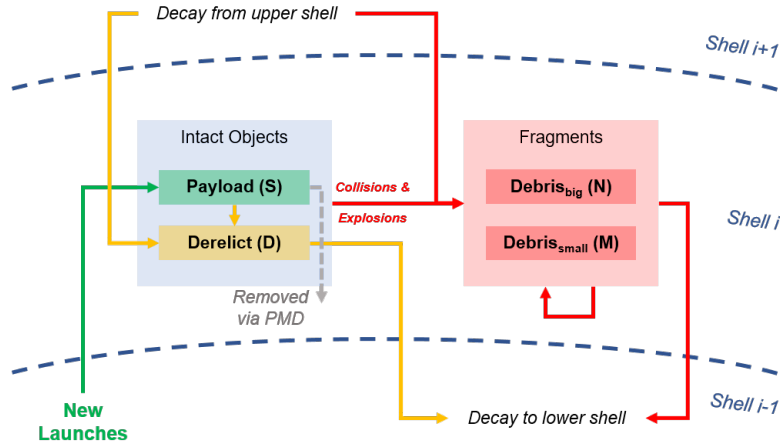


Figure 4-7: Schematic for the 4-population model that includes an expanded debris population.

Table 4.2: Pairwise interactions between the species for the expanded debris model (4-species model)

| | Species | S (Active satellites) | D (Derelicts) | N (Larger Debris) | M (Smaller Debris) |
|---|---|---|---|---|---|
| $\dot{C}$ Collision Source | S | $-\alpha_a \phi_{11} S^2$ | $\delta S(\phi_{12}D +\phi_{13}N +\phi_{14}M)$ | $n_{11}\phi_{11}\alpha_a S^2 +n_{12}\phi_{12}\alpha SD +n_{13}\phi_{13}\alpha SN +n_{14}\phi_{14}\alpha SM$ | $n_{11}\phi_{11}\alpha_a S^2 +n_{12}\phi_{12}\alpha SD +n_{13}\phi_{13}\alpha SN +n_{14}\phi_{14}\alpha SM$ |
| | D | $-\phi_{12}(\delta+\alpha)SD$ | $-\phi_{22}D^2$ | $n_{22}\phi_{22}D^2 +n_{23}\phi_{23}DN$ | $n_{22}\phi_{22}D^2 +n_{23}\phi_{24}DM$ |
| | N | $-\phi_{13}(\delta+\alpha)SN$ | $-\phi_{23}ND$ | $n_{33}\phi_{33}N^2$ | $n_{34}\phi_{34}NM$ |
| | M | $-\phi_{13}(\delta+\alpha)SM$ | $-\phi_{24}MD$ | $n_{34}\phi_{34}NM$ | $n_{44}\phi_{44}M^2$ |
| m Mass [kg] | - | 223 | 223 | $(1+\epsilon)\bar{m}_{N0}$ | $(1-\epsilon)\bar{m}_{N0}$ |
| b Diameter [m] | - | 1.5 | 1.5 | $(1+\epsilon)^{1/3}b_{N0}$ | $(1-\epsilon)^{1/3}b_{N0}$ |
| A Area [m²] | - | 1.77 | 1.77 | $(1+\epsilon)^{2/3}A_{N0}$ | $(1-\epsilon)^{2/3}A_{N0}$ |

Table 4.3: Simulation input parameters

| $h_{min}$ | $h_{max}$ | $N_{bins}$ | $d$ | $\Delta t$ | $v_r$ | $\alpha$ | $\delta$ | $\bar{m}_{N0}$ | $b_{N0}$ |
|---|---|---|---|---|---|---|---|---|---|
| 200 km | 1700 km | 50 | 30 km | 5 years | 10 km/s | 0.2 | 10 | 0.64 kg | 0.18 m |

## 4.4.2 Expanded payload and derelict populations for a 5-species model

As the payload and derelict satellite classes are inherently related, expanding the payload species will require expanding the derelict species. The additional payload and derelict populations result in a 5-species model, which is described in this section. The interaction of species per shell is visualized in Fig. 4-8. Note that there are now two payload classes ($S_+$ for the large payloads and $S_-$ for small payloads) as well as derelict classes ($D_+$ and $D_-$ for large and small derelict objects, respectively). The population interaction coefficients ($\dot{\mathbf{C}}$) are described in Table 4.4. Note that this sampling over size or mass of the species can be extended into any number of bins, and a schema is shown for expansion into two classes per species.
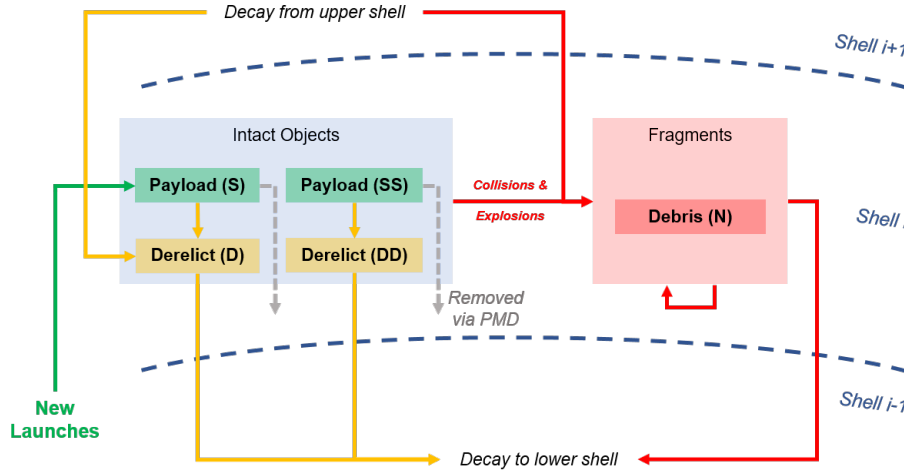


Figure 4-8: Schematic for the 5-population model that includes an expanded debris population.

## 4.4.3 Variance reduction of SSEM species parameters through binning

As mentioned in Sec. 4.4, one of the fundamental assumptions in the SSEM model is the fact that all objects within a species are homogeneous and therefore have the same parameters and characteristics. While this allows for SSEM models to simplify the problem, the reality is that even within the same species, there can be a large variation in the objects such as the mission lifetime, area, mass, probability of failure, etc. To model a particular scenario without bias, the mean or median value for the parameter within a species is often used. Because of the non-linear effect of parameters – such as the area-to-mass ratio on the deorbit duration – even if the averages are used to represent the species' generalized parameters, the result may show bias.

There are many assumptions in categorizing orbital objects into SSEM species. For each species, the physical parameters such as size, mass and area are uniform within each species. Or, at the very least,

Table 4.4: Pairwise interactions between the species for the expanded payload model (5-species model)

| | Species | $S_+$ (Large satellites) | $S_-$ (Small satellites) | $D_+$ (Large derelict) | $D_-$ (Small derelict) | N (Debris) |
|---|---|---|---|---|---|---|
| **Ċ** **Collision** **Source** | $S_+$ | $-\alpha_a\phi_{11}S_+^2$ | $-\alpha_a\phi_{12}S_+$ | $\delta S(\phi_{12}D_+$ $+\phi_{13}N$ $+\phi_{14}N)$ | $\delta S_+(\phi_{12}D_+$ $+\phi_{13}N$ $+\phi_{14}N)$ | $n_{11}\phi_{11}\alpha_a S_+^2$ $+n_{12}\phi_{12}\alpha S_+D$ $+n_{11}\phi_{11}\alpha S_+N$ $+n_{12}\phi_{14}\alpha S_+N$ |
| | $S_-$ | $-\alpha_a\phi_{11}S_+S_-$ | $-\alpha_a\phi_{11}S_-^2$ | $\delta S_-(\phi_{12}D_+$ $+\phi_{13}N$ $+\phi_{14}N)$ | $\delta S_+(\phi_{12}D_-$ $+\phi_{13}N$ $+\phi_{14}N)$ | $n_{11}\phi_{11}\alpha_a S_-^2$ $+n_{12}\phi_{12}\alpha S_-D$ $+n_{11}\phi_{11}\alpha S_-N$ $+n_{12}\phi_{14}\alpha S_-N$ |
| | $D_+$ | $-\phi_{12}(\delta+\alpha)S_+D_+$ | $-\phi_{12}(\delta+\alpha)S_-D_+$ | $-\phi_{22}D_+^2$ | $-\phi_{22}D_+D_-$ | $n_{22}\phi_{22}D_+^2$ $+n_{23}\phi_{24}D_+N$ |
| | $D_-$ | $-\phi_{13}(\delta+\alpha)S_+N$ | $-\phi_{13}(\delta+\alpha)S_-N$ | $-\phi_{23}ND_+$ | $-\phi_{23}D_-^2$ | $n_{34}\phi_{34}D_-N$ |
| | N | $-\phi_{13}(\delta+\alpha)S_+N$ | $-\phi_{13}(\delta+\alpha)S_-N$ | $-\phi_{24}ND_+$ | $-\phi_{24}ND_-$ | $n_{34}\phi_{34}N^2$ |
| **m** **Mass [kg]** | - | $(1-\epsilon)\bar{m}_{S0}$ | $(1+\epsilon)\bar{m}_{S0}$ | $(1+\epsilon)\bar{m}_{D0}$ | $(1-\epsilon)\bar{m}_{D0}$ | 0.64 |
| **b** **Diameter [m]** | - | $(1+\epsilon)^{1/3}\bar{b}_{S0}$ | $(1+\epsilon)^{1/3}\bar{b}_{S0}$ | $(1-\epsilon)^{1/3}\bar{b}_{D0}$ | $(1-\epsilon)^{1/3}\bar{b}_{D0}$ | 0.18 |
| **A** **Area [m²]** | - | $(1+\epsilon)^{2/3}A_{S0}$ | $(1+\epsilon)^{2/3}A_{S0}$ | $(1+\epsilon)^{2/3}A_{D0}$ | $(1-\epsilon)^{2/3}A_{D0}$ | 0.25 |

uniform enough so that a given value is representative in the model, usually chosen as some mean or median of a distribution from the actual population. This is immutable throughout the SSEM simulation. In real life, there may be distinctions in these physical parameters, notably for debris objects. Payloads and derelict objects are by definition intact source populations that are clearly defined; the assumption of a uniform population can be valid. However, for debris objects that are created by some fragmentation event, there is a large variety of physical parameters that interact with other objects differently through collisions, and deorbit at different timelines. A set of MC simulations is run with collision debris at multiple altitudes and propagated to see the changes to some of these parameters. The results are shown in Fig. 4-9, where the collision for each scenario is between 100 pairs of objects with masses of 200 kg and 20 kg. The simulation had no other initial population and $L_C = 10$ cm. In Fig. 4-9(a), the $B^*$ values are shown with dotted lines that denote the 25th and 75th percentiles, while the solid line denotes the median value. The $B^*$ values are shown to have a large variability within each scenario, and from altitude to altitude. Since $B^*$ is inversely proportional to the AMR of the object, this behavior is explained by the fact that higher AMR objects are quickly removed from the simulation due to drag, while low AMR and high $B^*$ objects remain. This causes an upward trend for $B^*$ over time, and this behavior occurs rapidly for collision debris at low altitudes. The population change also shows this behavior, as shown in Fig. 4-9(b).

The debris class is binned into various masses with roughly equal numbers of objects at the onset of collision debris generation. The evolution of the binned model $B^*$ evolution for the 800 km scenario is shown in Fig. 4-10. Binning into the various masses shows remarkably consistent $B^*$ parameters. This shows the strong correlation between the dynamics of the population, the mass and $B^*$. Dividing the debris population into these mass bins result in better uniformity within each binned debris class than when using one parameter to represent the entire class.

A *simple* launch case is simulated using MOCAT-MC to illustrate the use of a global median value for

(a) $B^*$ values of the debris class



(b) Debris population after collisions at varying altitudes
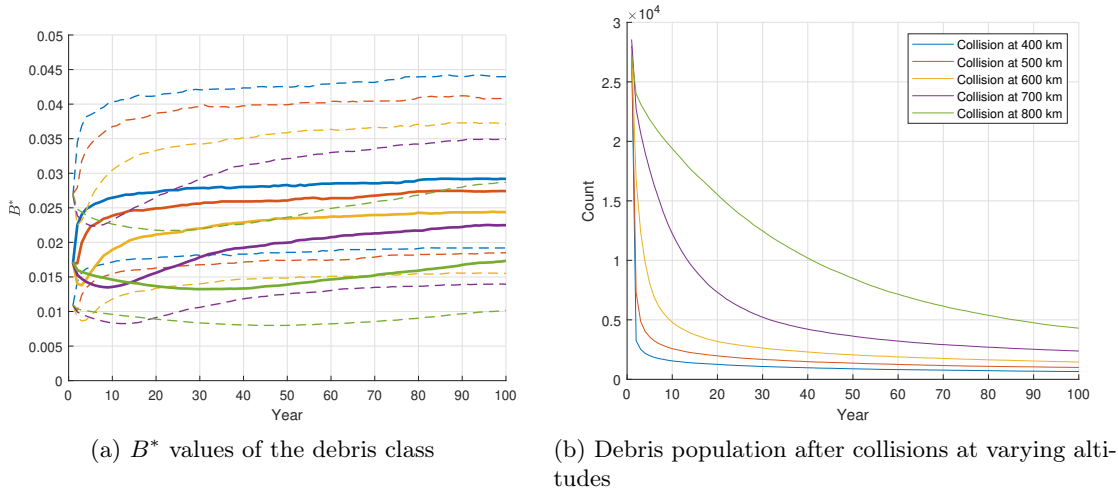
Figure 4-9: Scenario with collisions seeded at various altitudes
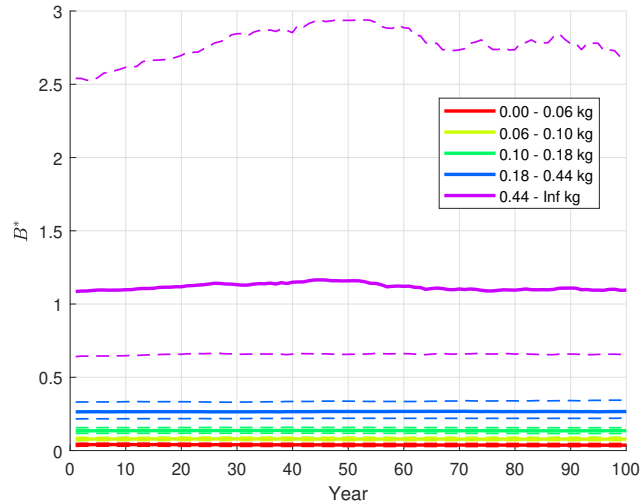


Figure 4-10: $B^*$ values of the binned debris class in mass for the 800 km collision scenario

debris and binned median values. In the *simple* launch case, no initial population is modeled and a constant launch rate is applied per altitude shell, ranging from 360 per 50-km shell near 200 km to 10 per year at 2000 km. PMD is set at 90%, and $L_C$ is set at 10 cm. The duration of the scenario was 150 years. The relationship between the mass of the debris objects and $L_C$ at the end of the 150 year scenario is shown in Fig. 4-11. Since the limit of the scenario $L_C$ was 10 cm, the limit is shown on the left, while there is a clear relationship between $L_C$ and mass, as expected. The discontinuity in the number of objects at $L_C = 1$ m is due to the SBM creating objects following two different methods. Objects below 1 m are created by following the strict power law CDF, whereas larger objects are created by combining the remaining mass into "a few" of the larger objects.

The histograms for each of the axes show the debris distribution for mass and $L_C$. If a median were used from this timestep, the median mass would be 0.152 kg, while the median $L_C$ would be 15.1 cm. In terms

98

of mass conservation, the true total mass of the debris at this timestep was 135.4 metric tons. If the median mass value were used for the number of debris objects (141049), as would be the assumption in an SSEM, the total mass would come to 21.4 mt. This descrepancy is one of the reasons for binning the SSEM species in size ($L_C$), as there is a clear relationship between size and mass, which would affect the deorbit property through AMR as well as secondary collision numbers.

The right subplot shows the distribution using the NASA SBM. Note that the SBM ascribes a bimodal AMR to each of the debris given its $L_C$, from which the mass can be derived.



(a) After 150 years of *simple* launches

(b) Distribution according to NASA SBM
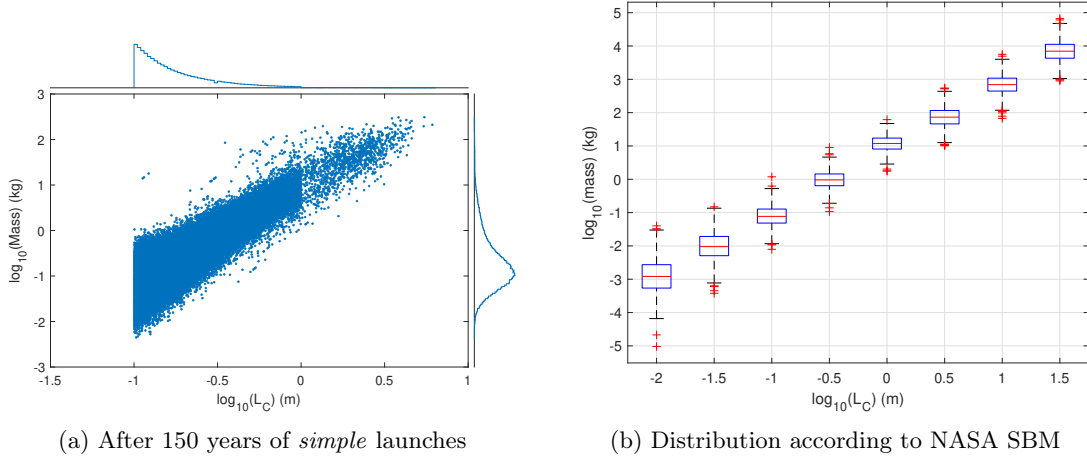
Figure 4-11: Distribution of $L_C$ and mass of debris objects



(a) Payload count

(b) Median mass of Debris objects
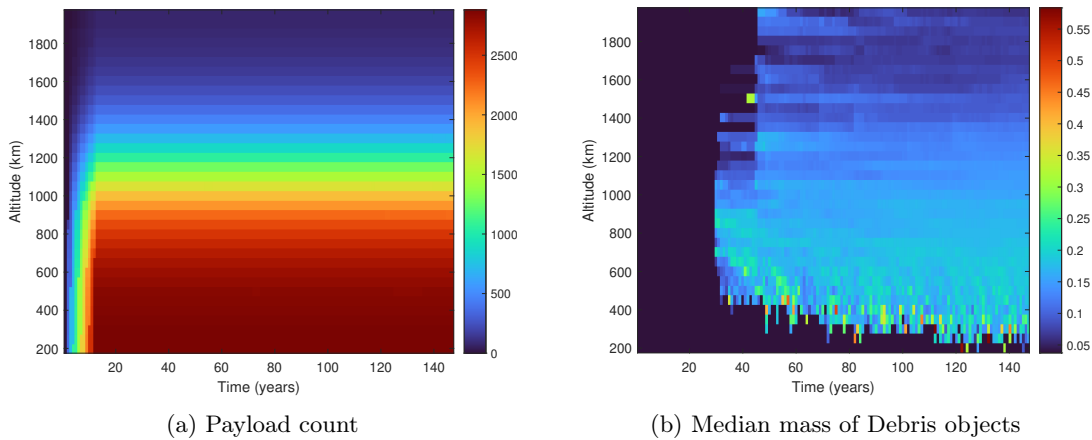
Figure 4-12: Distribution of masses after *simple* launch case

The *simple* launch scenario's payload count per time step is shown in Fig. 4-12. With a 8-year mission lifetime, the steady-state number of active payloads at the 200 km altitude bin is 2880 while at 2000 km it is 80. The median mass value per altitude bin every 2 years is shown in Fig. 4-12(b). The median is only taken if the population is >6. A clear dependence on altitude is also shown where the lower-altitude debris objects consist primarily of more massive objects that remain longer in the denser lower orbits.

It is clear that treating the entire debris species as a uniform class using the median physical parameters

will introduce a large loss of fidelity. The lack of mass conservation, deorbit profile, and secondary collisions would skew the result. By allowing multiple bins of the physical parameters, the variance of the parameters for the binned species can be reduced, allowing for a higher-fidelity and lower-bias SSEM model. By allowing for multiple bins of the physical parameters, the variance of the parameters for the binned species can be reduced, allowing for a higher-fidelity and lowered-bias SSEM model.

### 4.4.4 Binned SSEM Parameters

The fundamental difference between the number of objects and the relationship between $L_C$ and the mass of debris objects from the NASA SBM means that with few bins, mass conservation and number of debris population cannot both be fulfilled with the generalized binned model as described in the previous section. The optimal location for binning in $L_C$ for the debris class was found using the mass conservation factor as the cost function. The cost function is defined as:

$$\min_{x} \quad f(x) = \left( \sum_{i=1}^{n} \tilde{m}_i c_i - m_{tot} \right)^2 , \tag{4.11}$$

where $\tilde{m}_i$ is the median mass of the objects in bin $i$ and $c_i$ is the number of objects in that bin for $n$ total bins, and $m_{tot}$ is the total mass of the debris objects. Bin numbers $n = 1$ through 50 were run, with optimal edges and the resulting error shown in Fig. 4-13. The edges of the bins are chosen as the extrema of the debris $L_C$, which in this case ranges from 10 cm to 6.1 m. The optimal bins are shown to largely follow a log-linear pattern, though often with some bias toward denser spacing below 1 m. This can also be attributed to the SBM creating objects with two different methods at that size.



(a) Optimal bin edges　　　　　　　　(b) Total mass error

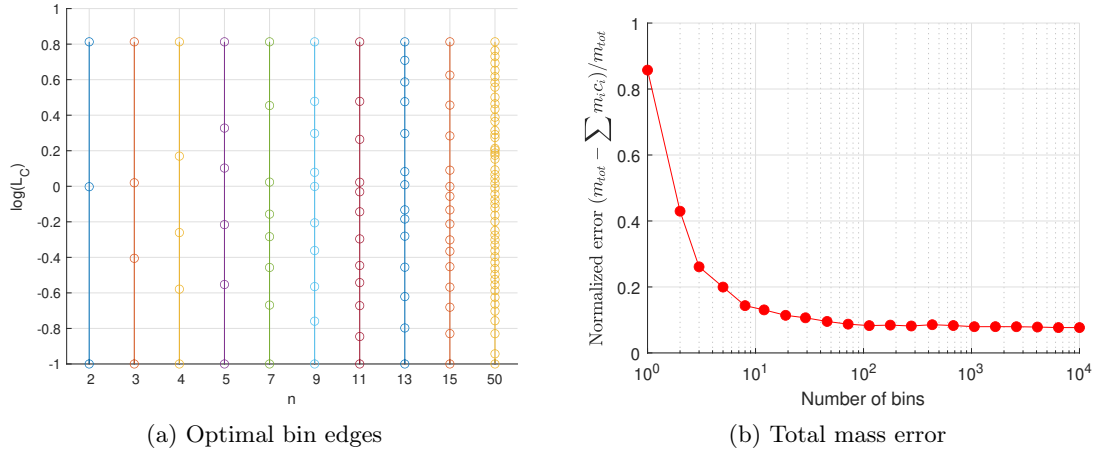Figure 4-13: Optimization of binning for debris class depending on a range of number of bins in $L_C$

The error is defined as the ratio between the difference in the total debris mass calculated in the binned model and the total debris mass. As expected, as the number of bins grows, the error decreases, although not all the way to 0. With the singular bin, the mass error is around 86% of the total mass of the parent objects

and reduces to 14% with 8 bins. The SSEM calculation yields less mass than the expected mass due to the skewness of each bin toward smaller objects which contribute less in aggregate compared to the larger objects, as shown in Fig. 4-11. The trade between fidelity of mass conservation from collision and compuatational cost shown in Fig. 4-4 will be needed when setting up the SSEM model. A more detailed analysis of the mass conservation effect, an alternative method of calculating the representative physical parameters of the bin, and the effect of minimum $L_C$ is explored in Appendix G.

The result of a similar *simple* launch case is run within the SSEM environment with a range of binning for the debris class. The unbinned case similar to the MOCAT-3 model is run, and a range of optimized bins calculated earlier is run for up to 9 debris classes to see the differences in the final result. No initial population is given, and the launched payloads have mass of 260 kg, radius of 0.7 m and area of 1.7 m$^2$, and collision avoidance efficacy of $\alpha = \alpha_a = 10^{-5}$. Mission life is 8 years, and PMD efficacy is 0.65. The launch model tapers off around 800 km and totals 6588 launches per year, as illustrated in Fig. 4-14. The environment is divided into 50 km shells ranging from 200 km to 1400 km with the static exponential atmospheric model, and is simulated for 200 years.



(a) Launch population        (b) Population of all debris for 11-binned model
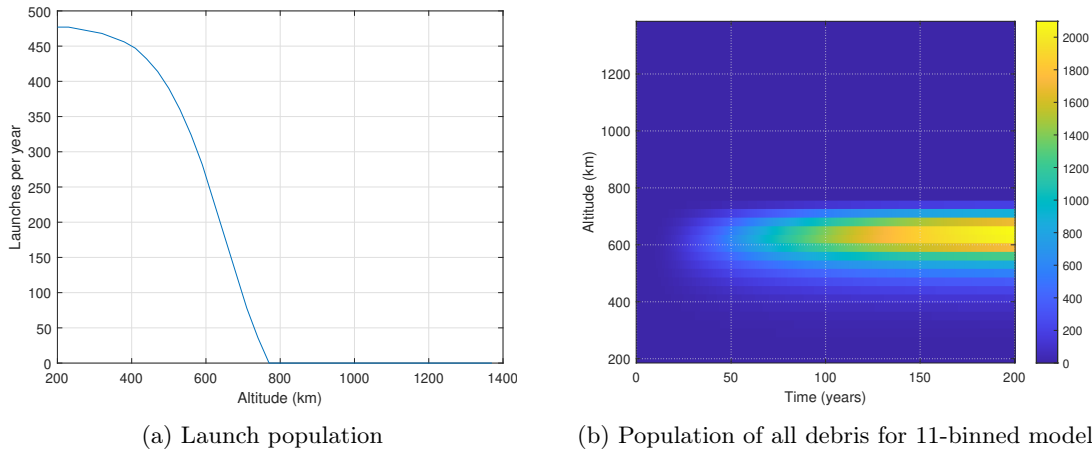
Figure 4-14: *Simple* launch case

The results comparing the various binning are shown in Fig. 4-15, where the debris mass profile at $t = 200$ years is shown along with the total debris population over time. As shown earlier, the marginal benefit of adding more bins is reduced. The error for the unbinned case can be explained by the skewness of the debris parameters. For the unbinned case, the median mass value is much higher.

## 4.5    Addition of Delta-V Dynamics from Collisions

The debris generated in a collision in orbit typically have a distribution of velocities added to them, dispersing them from the original parent objects. In a hyper-velocity catastrophic collision, the collision is much like an explosion, where the velocity is generally uniform around the object. The NASA SBM describes this delta-v distribution in a 1-D velocity derived from the area-to-mass ratio of the object. The debris with any velocity

(a) Debris mass profile at final timestep        (b) Total debris population
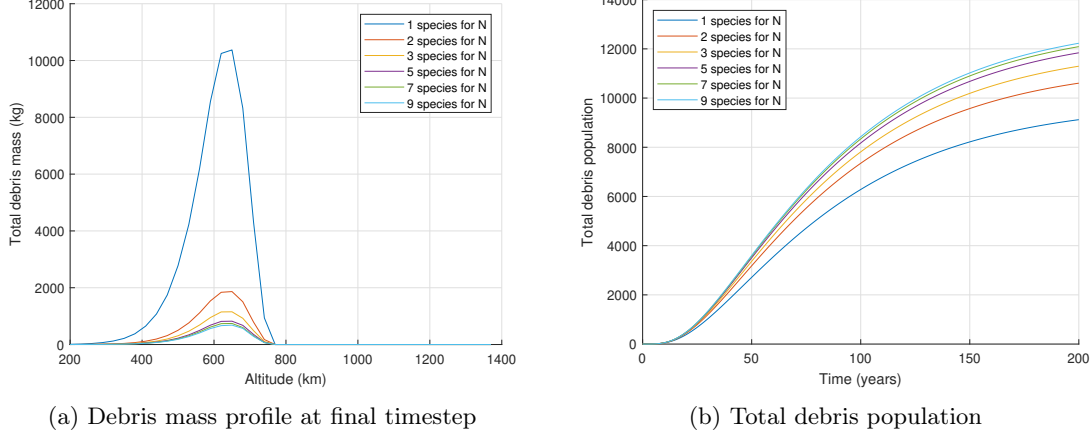
Figure 4-15: Comparison between binning amount for the debris class

added to the in-track direction would attain a higher semi-major axis, while debris with velocity added in the opposite direction would lose the semi-major axis. This change in altitude has not been added in the SSEM in the literature nor has it been present in the previous versions of MOCAT-SSEM. Without the dynamics implemented to add velocity to the debris, it was assumed that all of the created debris would stay within the altitude shell of the collision, preventing any debris from spreading into lower and higher shells. The number of debris created from collisions is described earlier in Eq. 4.10, which implicitly describes the generation of collision debris into the shell in which the collision occurs. Expanding the collision term for the debris class for a 3-species MOCAT-3 model ($N_s = 3$) for the $k$th shell yields:

$$\dot{C}_{N,k} = \sum_{i,j=1}^{N_s} \Gamma_{ij}\phi_{ij}Q_iQ_j \bigg|_k \tag{4.12}$$

$$= n_{SS}\alpha_a\phi_{SS}S_k^2 + n_{SD}\alpha\phi_{SD}S_kD_k + n_{SN}\alpha\phi_{SD}S_kN_k \tag{4.13}$$

$$+ n_{DD}\phi_{DD}D_k^2 + n_{DN}\phi_{DN}D_kN_k + n_{NN}\phi_{NN}N_k^2, \tag{4.14}$$

where the variables are defined consistently with the MC variables, with $n_{ij}$ denoting the number of debris generated from a collision between $i$ and $j$ objects, $S_k, D_k, N_k$ noting the population of $S, D, N$ in shell $k$, $\alpha_a$ the collision avoidance factor for payload-on-payload collisions, $\alpha$ the collision avoidance factor between a payload and any other object, and $\phi_{ij}$ the collision probability defined in Eq. 4.10. As noted earlier, the collision is independetly assessed for each shell, and all of the collision debris remains in the shell.

In this section, a spreading function is implemented to allow the debris from a collision in a shell to deposit the debris in another shell to introduce the Delta-V dynamics to the collision debris with the spreading function $\Gamma_{ij,mk}$, and the number of objects increased for the debris class in shell $k$ can be written as:

102

$$\dot{C}_{N,k} = \sum_{m=1}^{N_{sh}} \sum_{i,j=1}^{N_s} \Gamma_{ij,mk} \phi_{ij} Q_{i,m} Q_{j,m}, \tag{4.15}$$

where $\Gamma_{ij,mk}$ represents the expected number of debris generated per collision between object pair $i, j$ multiplied by collision probability modifiers such as $\alpha$ for objects in shell $m$ depositing in shell $k$. $N_{sh}$ denotes the number of shells, $Q_{i,m}$ denotes the pouplation of object type $i$ in shell $m$. This formulation allows for collisions from shells to affect the population of debris deposited into another shell.

The expected number of objects created from a pair of species types remains the same, so $\Gamma_{ij,mk}$ is defined such that

$$\Gamma_{ij} = \sum_{m=0}^{\infty} \Gamma_{ij,m}, \tag{4.16}$$

where the summation of $m$ from 0 to $\infty$ denotes that the sum of debris produced into all shells including those that deorbit up to reaching escape velocity. Because a number of debris from catastrophic collisions do in fact produce debris that deorbit or reach escape velocity, it is often the case that $\Gamma_{ij} > \sum_{m=1}^{N_{sh}} \Gamma_{ij,m}$.

Calculating the number of debris deposited into different shells from a collision is simplified to the average case. For a circular orbit at 200 km to raise its semi-major axis to 250 km, it takes 29.4 m/s of Delta-V, while for a circular orbit at 1950 km orbit to raise to 2000 km it takes 20.7 m/s. The average shell between 200 and 2000 km requires 24.6 m/s to raise 50 km, as shown in Fig. 4-16(a). Using this mean value, a spreading function can be calculated that allocates the debris from a collision. Using the NASA SBM and the resulting Delta-V, a collision in a typical shell will impart debris that follows the distribution shown in Fig. 4-16(b). The case shown is between two 260 kg objects resulting in a catastrophic collision, and the count is an average of 20 runs allowing for fractional counts. The highest deposition of debris is in the shell of the collision, as expected, though some objects – particularly light objects with high AMR – go below the lowest shell or above the highest shell. Larger masses with low AMR tend to gain little Delta-V and largely remain in the collision shell. This spreading function defines $\Gamma_{ij,m}$.

With this addition, the Delta-V dynamics from collisions is captured in the SSEM model. The number of equations remains the same, with more terms for each of the equations. This allows higher fidelity to be achieved at scale. In comparison to Fig. 4-3, the DV dynamics adds fidelity to the breakup dynamics as shown in the Gabbard plots in Fig. 4-17. The collision's interaction with the higher shells is clearly seen. The circular orbit assumption and altitude shell environment are present, hence the similar set of preigees and apogees and discretized periods.
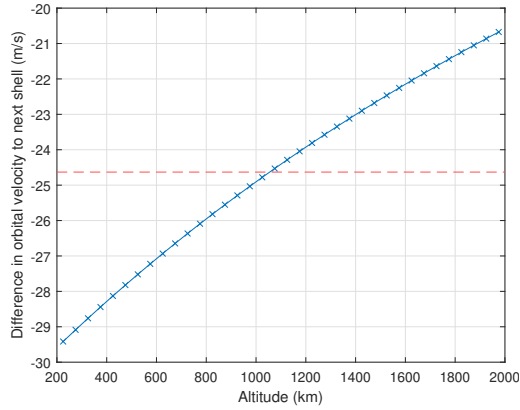
(a) Delta-V needed to change one shell
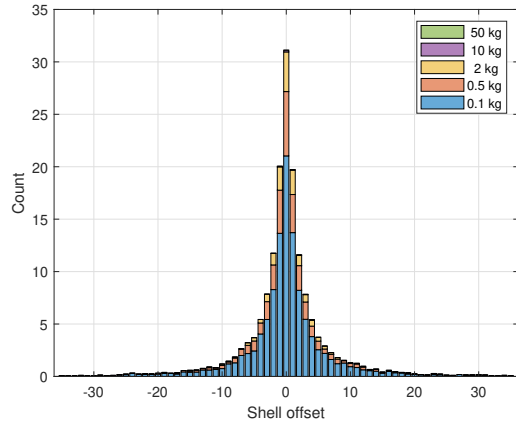
(b) Distribution of debris into neighboring shells

Figure 4-16: Delta-V dynamics applied to SSEM using a spreading function



(a) 7 Species SSEM
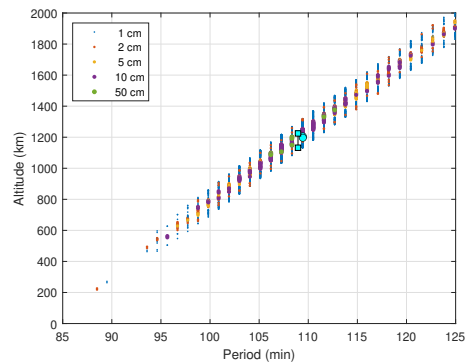
(b) SSEM with DV dynamics

Figure 4-17: Gabbard plot of debris 15 years after a collision

## 4.6  Validation of SSEM with MC using equilibrium solutions

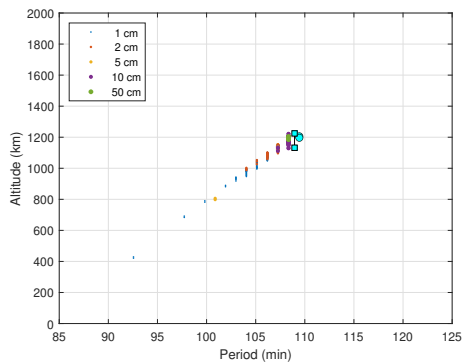SSEM formulation is useful in obtaining equilibrium solutions where, for a given launch rate and initial population, all population rate of change is zero. As described in [26], this is when

$$0 = \left[\dot{S}, \dot{D}, \dot{N}, ...\right]^T = \dot{\boldsymbol{P}} = \dot{\boldsymbol{\Lambda}} + \dot{\boldsymbol{C}}_{PMD} + \dot{\boldsymbol{F}} + \dot{\boldsymbol{C}}. \tag{4.17}$$

In [26] the SSEM model lacked the Delta-V dynamics, resulting in an equilibrium solution that allowed more launches in the higher orbits. With no mechanism to deposit debris into lower and higher orbits from the collision orbit, the higher orbits simply had to limit its own collisions and balance derelict accumulation with drag forces. With the inclusion of Delta-V collision dynamics, a dense lower orbit regime will also deposit debris into the higher orbits, accumulating debris faster. A comparison between the two equilibrium solutions is shown in Fig. 4-18.



(a) MOCAT3         (b) MOCAT3 with DV dynamics
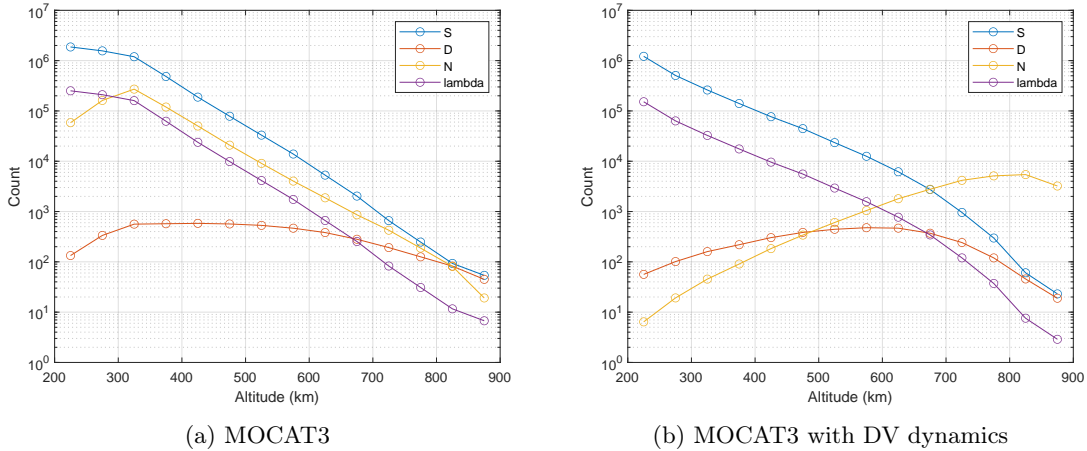
Figure 4-18: Comparison of equilibrium solutions with and without Delta-V dynamics

The equilibrium solution is run with SSEM only up to 900 km where there is some atmosphere to counteract some amount of accumulation. The comparison makes it clear how the accumulation of debris at higher orbits is the expected equilibrium. The launch rate difference is also seen, where the amount of payloads launched into the higher orbits is markedly lower. However, an overall increase in capacity is seen, with a higher total number of launches for MOCAT3-DV. Previously, all debris was generated and deposited in the same shell, which meant a rapid growth in collisions, which scales as $\propto N^2$ within the shell. With the spreading factor, the number of debris generated per collision is spread amongst neighboring shells, with some objects being removed from the simulation immediately or very quickly. Linear scale plots are shown in Figs. A.13 in the Appendix.

For comparison to MC runs using these equilibrium solutions, care must be taken in assigning the type of object, namely, for the debris class. In MC simulations, debris sizes down to $L_C$ will be created, whereas in SSEM there may only be one debris size. How to bin when counting the population is explored by comparing

the MC runs using the equilibrium solution launch rate and initial condition.



(a) Linear plot        (b) Log plot
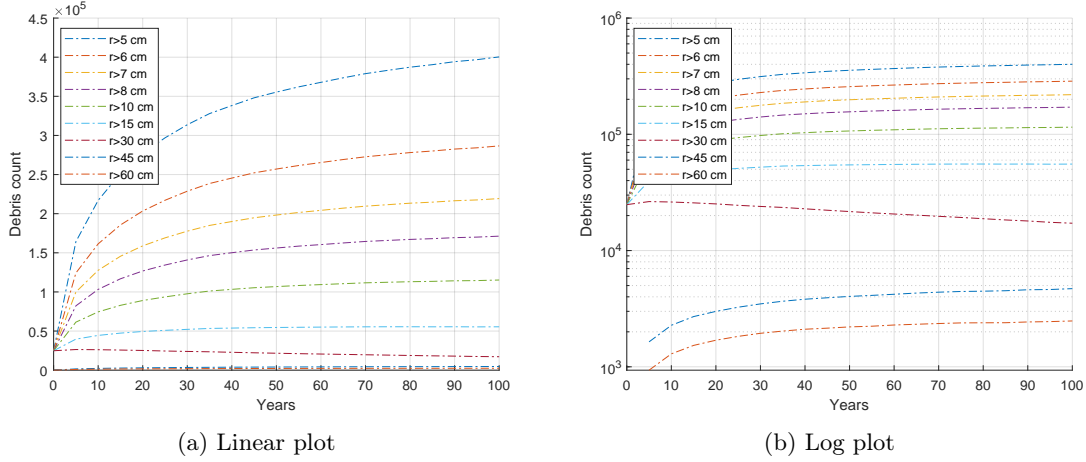
Figure 4-19: Debris Count from MC runs vs SSEM for equilibrum solution

The size of the debris class objects in MOCAT3-DV was 40 cm. The debris object count from the MC run with $L_C = 10$ cm is shown in Fig. 4-19, where the simulation was also limited to altitudes between 200 and 900 km. The plots show the evolution of the debris count depending on the smallest debris to count, ranging from $r > 5$ cm to $r > 60$ cm. This shows a near-equilibrium at $r > 40$ cm, not deviating far from the original equilibrium solution of 24833.62 total debris objects at 40 cm. The number of debris between the SSEM debris size and $L_C$ dominates the number of objects; however, the equilibrium solution is found when looking at the appropriate radius and larger.

Additional analysis will need to be done with multibinned model and the Delta-V dynamics and finding the optimal population binning to translate the equilibrium solution from SSEM to MC. However, the models show good agreement, and the additional improvements to SSEM have shown to be important in producing a higher-fidelity model with mass conservation and collision debris dynamics.

# Chapter 5

# Conclusion

## 5.1 Summary

As access to space is becoming easier and with the accelerated pace of launches into LEO, it is imperative to be able to model the future space environment and understand the various inputs that can shape the future. This thesis presents a novel evolutionary model called MOCAT-MC which is described and validated. Various future scenarios and historical scenarios are analyzed using the tool.

MOCAT-MC efficiently models the evolution of the orbital population that is characterized by dynamics such as launches, collisions, explosions, deorbits, and more. This Monte Carlo tools is flexible in its modeling fidelity with several options for the propagator, initial simulation population, and launch profiles. A sampling-based collision model is used and its sensitivity to input parameters is explored. This tool can be used to model the effect various future launches scenario to the orbital population evolution, and help answer key questions around LEO orbital capacity and sustainable usage of the space environment. The efficiency of this model is able to extend analysis to small lethal non-trackable objects, which is an important enabler in understanding the future LEO environment.

The comparatively simpler SSEM model is explored in this thesis as well, and its fidelity increased through novel addition of binning and collision dynamics. Though lower fidelity than MC, these SSEM models compute the long-term future environment in seconds and allows for optimization to find high capacity equilibrium solutions. Several challenges with the extendibility and validity of this model are identified and the exploration of options to increase its fidelity. This model has been used by several economic and policy studies, and is continuing to improve its usability.

In summary, the main contributions and findings of this thesis include the following:

- Development of an open-source MC-based evolutionary orbital population model that can simulate tens of millions of orbital objects on a single-thread. This allows for Lethal Non-Trackable objects to be analyzed, where the inclusion of such small objects leads to a much increase in non-catastrophic

collisions and to a lesser degree catastrophic collisions.

- Demonstration that analytical propagation can be used to scale MC simulations

- Analysis of future constellation traffic as filed with ITU and FCC, reaching more than 80,000 operational satellites in LEO from the filed constellations alone, where the contribution from higher orbit satellites are shown to be much more long-lasting compared despite fewer launches.

- Increased fidelity of the Source-Sink Evolutionary Model (SSEM) through the use of multi-binned objects and inclusion of the Delta-V dynamics to SSEM formulation allowing for shell-to-shell interactivity in debris deposition, where the model shows a closer match to the MC models.

We currently live in an inflection point in terms of amount of investment and number of objects launched into space. It is very possible that more objects will be launched in the next few years than was launched previously. The analogous period with global warming would be the industrial age, and the summer of 2020 for the COVID pandemic. It is imperative then that stakeholders, such as policy makers and the interested public, be able to use open models for which the assumptions are clearly laid out with realistic parameters. MOCAT was produced with such vision in mind to understand the future space environment and sustainability.

## 5.2 Future work

The models described in this thesis, as well as the analysis, are limited in scope. Future work for the MOCAT-MC model includes expansion of the model capability such as deterministic collision modeling and semi-analytical propagators. Other fragmentation models and the ability to seed the initial population with existing debris density models would also allow for a higher-fidelity initial population. The addition of these modules will allow even more flexibility in trading fidelity for computational cost, so that the appropriate fidelity can be used for the desired analysis. Additional analysis using the tool can include the long-term effect of different policies and one-off events such as geomagnetic storms, the relative PMD levels at various densities and altitudes, and actuarial analysis for satellite operators in various debris environments. Though LNT objects were included, the collision effect from these objects are static - even collisions with low specific energy renders an active payload into a derelict or debris objects. This effect could be tuned such that a more realistic effect such as probabilistic creation of a derelict object can be modeled.

The fidelity of the SSEM model can increase with eccentricity and inclination binning, though at a much higher compuatational cost. Other layers of optimization can be added, along with continued validation against MC and ML models, especially in finding equilibrium solutions which can aid in orbital capacity analysis. The model can be used to measure the effect of federal and economic policies on space debris generation and gaming between multiple actors to explore the multi-polar future environement as well.

# Appendix

## A    Variability in B* in TLEs

A snapshot of the B* values from TLEs from January 2023 is shown in this figure. The B* value is a fitted parameter, hence the non-physical negative values for a large number of objects.
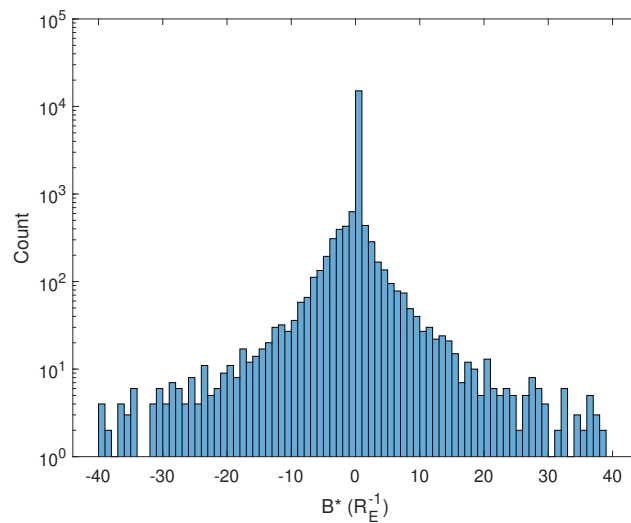


Figure A.1: Distribution B* values from TLEs (Jan 2023)

## B    Resampling for mass and radius of objects

Fig. A.2 compares the different methods for resampling the physical parameters of the missing objects.

(a) Payload        (b) Rocket Body        (c) Debris
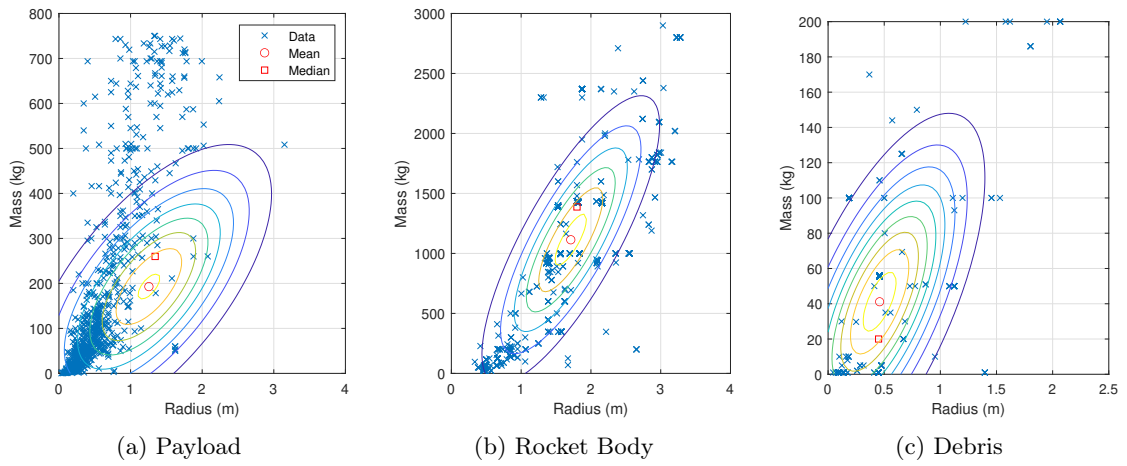
Figure A.2: Parameter resampling for various object classes

## C  *No Future Launch* scenarios

The data used for the *No Future Launches* and *Extrapolated* scenarios with January 2023 epoch are described here. Table A.1 shows the breakdown of each object as described by DISCOS, where MRO represents Mission Related Objects, FD represents Fragmentation Debris, and D represents Debris as defined by ESA [34].

Figure A.3 shows the altitude distribution of the objects at the beginning of the epoch. The total number of objects at the start of the epoch is 18065. In this figure, all objects not considered *Payload* or *Rocket Body* are considered to be part of the *All Debris* class. The large contribution from Starlink since 2019 in the 500 km altitude bin is notable.

Table A.1: Breakdown of object type in the initial population for January 2023

| Payload | Payload MRO | Payload Frag. Debris | Payload Debris | Rocket Body |
|---|---|---|---|---|
| 7866 | 233 | 5573 | 95 | 971 |

| Rocket Body MRO | Rocket Frag. Debris | Rocket Debris | Other Debris | Uknown |
|---|---|---|---|---|
| 609 | 2808 | 25 | 253 | 1 |



Figure A.3: Semi-major axis of objects used for initial population at Jan 1, 2023
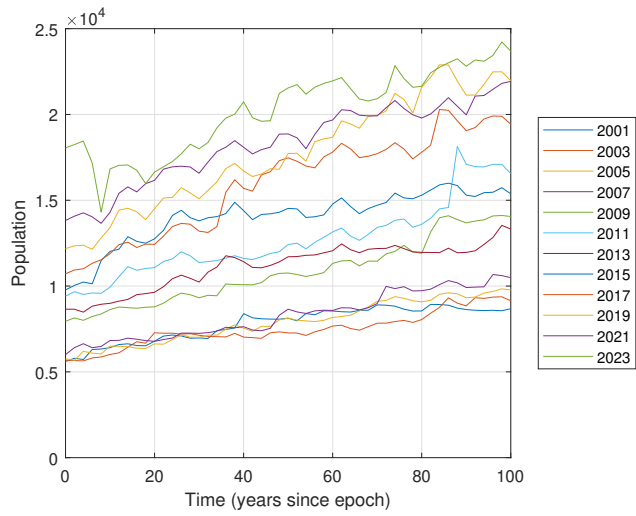
Figure A.4: Total population for No Future Launches cases with varying epochs



(a) Payload

(b) Derelict

(c) Debris

(d) Rocket body
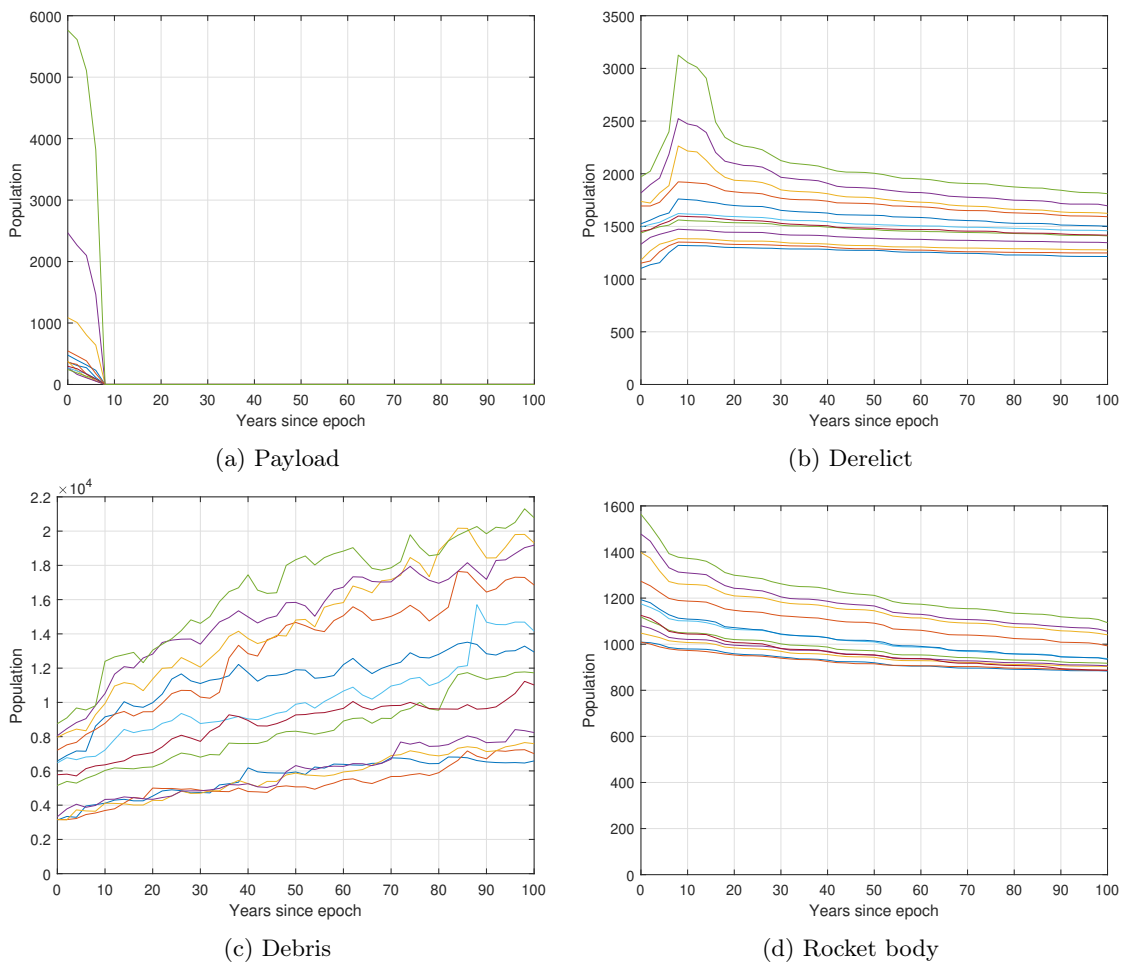
Figure A.5: Number of objects per object type for the No Future Launch cases with varying epochs

# D    Megaconstellation future traffic model

Table A.2 describes the future megaconstellation modeled in this work compiled from various sources including [106] as of March 2023. *Total num* column denotes the final operational constellation size without spares, *Start Year* and *Finish Year* denotes the start and end of the ramp-up phase to get to the final operational number per constellation. Some constellations are missing some information such as the launch year and physical attributes. Launch dates were estimated for the purposes of the scenarios as shown in Fig. A.7, and the physical attributes were set equal to the Starlink constellation.

Table A.2: Modeled future traffic for megaconstellations

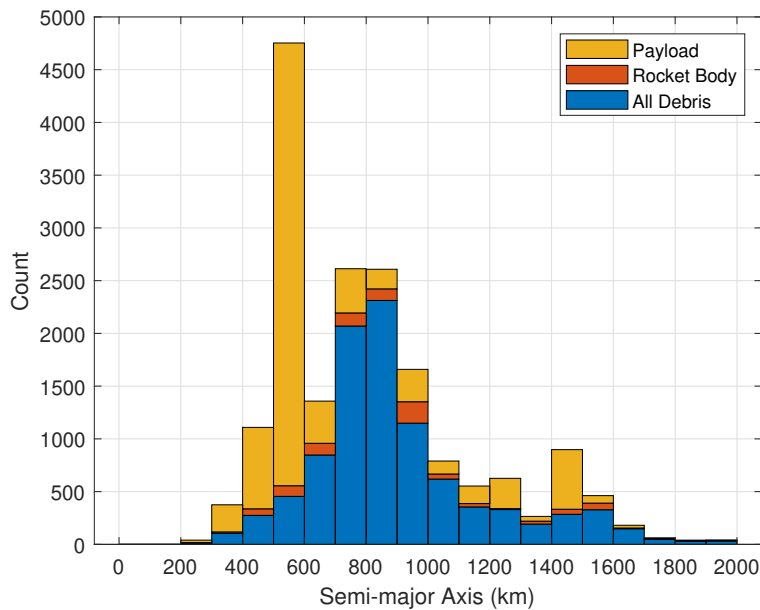| Constellation | Alt (km) | Inc (deg) | Total Num | Start Year | Finish Year | Mass (kg) | Radius (m) |
|---|---|---|---|---|---|---|---|
| Starlink | 550 | 53 | 1584 | 2018 | 2027 | 260 | 2.0 |
| Starlink | 570 | 70 | 720 | 2018 | 2027 | 260 | 2.0 |
| Starlink | 560 | 97.6 | 348 | 2018 | 2027 | 260 | 2.0 |
| Starlink | 540 | 53.2 | 1584 | 2018 | 2027 | 260 | 2.0 |
| Starlink | 560 | 97.6 | 172 | 2018 | 2027 | 260 | 2.0 |
| Starlink2A | 530 | 43 | 2500 | 2023 | 2031 | 800 | 2.0 |
| Starlink2A | 525 | 53 | 2500 | 2023 | 2031 | 800 | 2.0 |
| Starlink2A | 535 | 33 | 2500 | 2023 | 2031 | 800 | 2.0 |
| Starlink2 | 340 | 53 | 5280 | 2023 | 2031 | 1250 | 4.0 |
| Starlink2 | 345 | 46 | 5280 | 2023 | 2031 | 1250 | 4.0 |
| Starlink2 | 350 | 38 | 5280 | 2023 | 2031 | 1250 | 4.0 |
| Starlink2 | 360 | 96.9 | 3600 | 2023 | 2031 | 1250 | 4.0 |
| Starlink2 | 530 | 43 | 860 | 2023 | 2031 | 1250 | 4.0 |
| Starlink2 | 525 | 53 | 860 | 2023 | 2031 | 1250 | 4.0 |
| Starlink2 | 535 | 33 | 860 | 2023 | 2031 | 1250 | 4.0 |
| Starlink2 | 604 | 148 | 144 | 2023 | 2031 | 1250 | 4.0 |
| Starlink2 | 614 | 115.7 | 324 | 2023 | 2031 | 1250 | 4.0 |
| OneWeb | 1200 | 87.9 | 588 | 2019 | 2023 | 150 | 0.5 |
| OneWeb | 1200 | 55 | 128 | 2019 | 2023 | 150 | 0.5 |
| OneWeb | 1200 | 87.9 | 1764 | 2025 | 2028 | 150 | 0.5 |
| OneWeb | 1200 | 40 | 2304 | 2025 | 2028 | 150 | 0.5 |
| OneWeb | 1200 | 55 | 2304 | 2025 | 2028 | 150 | 0.5 |
| Kuiper | 590 | 33 | 782 | 2024 | 2029 | 700 | 1.5 |
| Kuiper | 590 | 30 | 2 | 2024 | 2029 | 700 | 1.5 |
| Kuiper | 610 | 42 | 1292 | 2024 | 2029 | 700 | 1.5 |
| Kuiper | 630 | 51.9 | 1156 | 2024 | 2029 | 700 | 1.5 |

**Table A.2 Continued:** Modeled future traffic for megaconstellations

| Constellation | Alt (km) | Inc (deg) | Total Num | Start Year | Finish Year | Mass (kg) | Radius (m) |
|---|---|---|---|---|---|---|---|
| Guanwang | 590 | 85.0 | 480 | 2035 | 2055 | - | - |
| Guanwang | 600 | 50.0 | 2000 | 2035 | 2055 | - | - |
| Guanwang | 508 | 60.0 | 3600 | 2035 | 2055 | - | - |
| Guanwang | 1145 | 30.0 | 1728 | 2035 | 2055 | - | - |
| Guanwang | 1145 | 40.0 | 1728 | 2035 | 2055 | - | - |
| Guanwang | 1145 | 50.0 | 1728 | 2035 | 2055 | - | - |
| Guanwang | 1145 | 60.0 | 1728 | 2035 | 2055 | - | - |
| Yinhe | 511 | 63.5 | 1000 | - | - | 230 | 0.7 |
| Hanwha | 500 | 97.5 | 2000 | 2025 | 2035 | - | - |
| Lynk | 500 | 97.5 | 2000 | - | - | 125 | 0.5 |
| Astra | 700 | 0 | 40 | - | - | 500 | - |
| Astra | 690 | 98.0 | 504 | - | - | 500 | - |
| Astra | 700 | 55.0 | 1792 | - | - | 500 | - |
| Astra | 380 | 97.0 | 2240 | - | - | 500 | - |
| Astra | 390 | 30.0 | 4896 | - | - | 500 | - |
| Astra | 400 | 55.0 | 4148 | - | - | 500 | - |
| Boeing | 1056 | 54.0 | 132 | 2025 | 2030 | - | - |
| Telesat | 1015 | 99.0 | 78 | 2023 | - | - | - |
| Telesat | 1325 | 50.9 | 220 | 2023 | - | - | - |
| Telesat | 1015 | 99.0 | 351 | 2023 | - | - | - |
| Telesat | 1325 | 50.9 | 1320 | 2023 | - | - | - |
| HVNET | 1150 | 55.0 | 1440 | - | - | - | - |
| SpinLaunch | 830 | 55.0 | 1190 | - | - | 150 | - |
| Globalstar3 | 485 | 55.0 | 1260 | - | - | - | - |
| Globalstar3 | 515 | 70.0 | 100 | - | - | - | - |
| Globalstar3 | 600 | 55.0 | 900 | - | - | - | - |
| Globalstar3 | 620 | 98.0 | 100 | - | - | - | - |
| Globalstar3 | 700 | 55.0 | 720 | - | - | - | - |

Fig. A.6 shows the unifed launch population per time broken into individual constellation planes. The constellation name denotes the altitude in km and inclination in degrees in the parenthesis. Note that *Kuiper (590/30)* includes just 2 operational satellites.

Fig. A.8 shows the population of active satellite growth for each constellation in a log scale for comparison. The black dashed line shows the total number of constellation. The vertical red dashed line notes the year 2023. Data preceding this line is from actual launch data, showing population from Starlink and OneWeb. The population modeled after 2023 is modeled from the information from Table A.2.
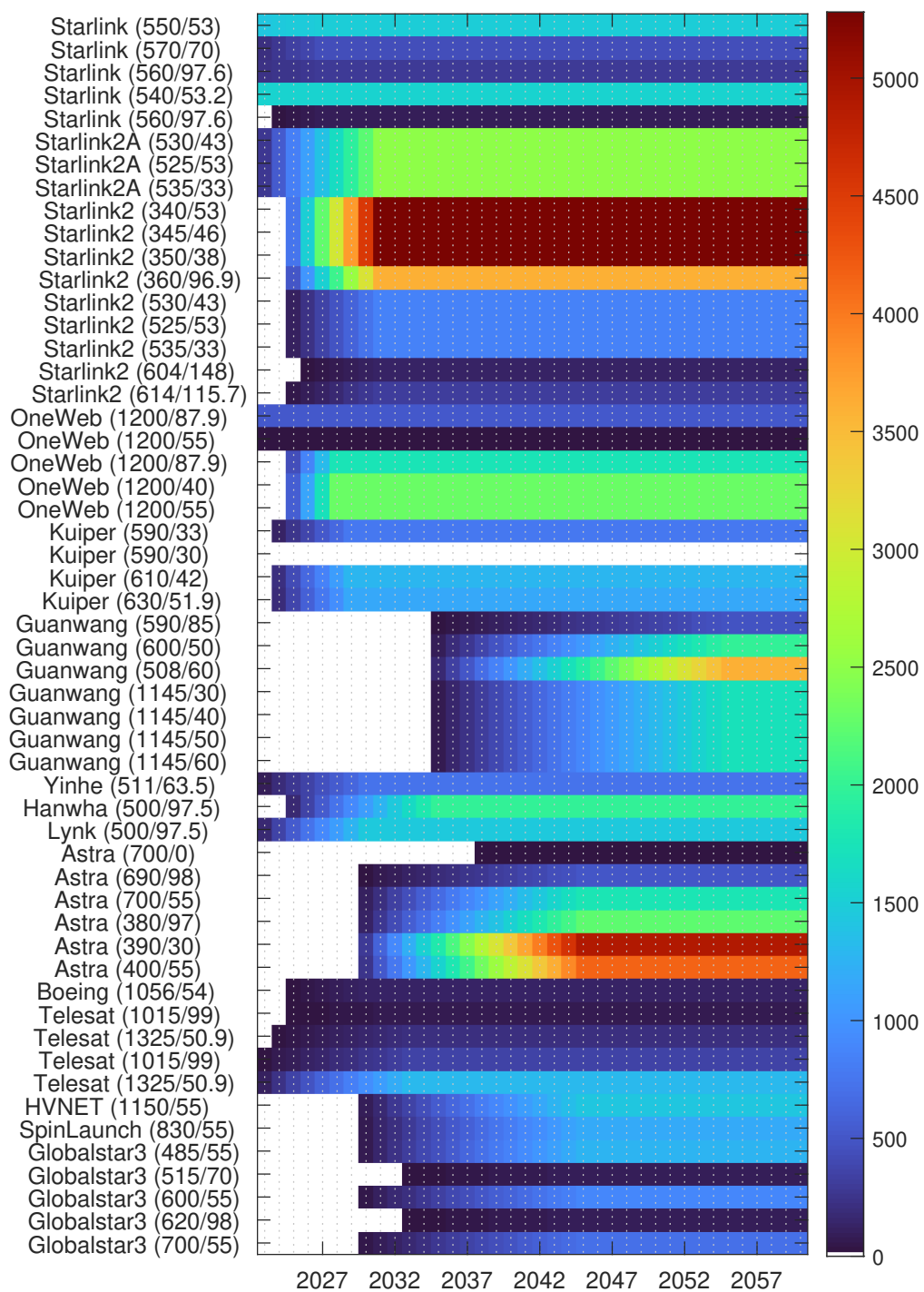
Figure A.6: Megaconstellation population assumption

115
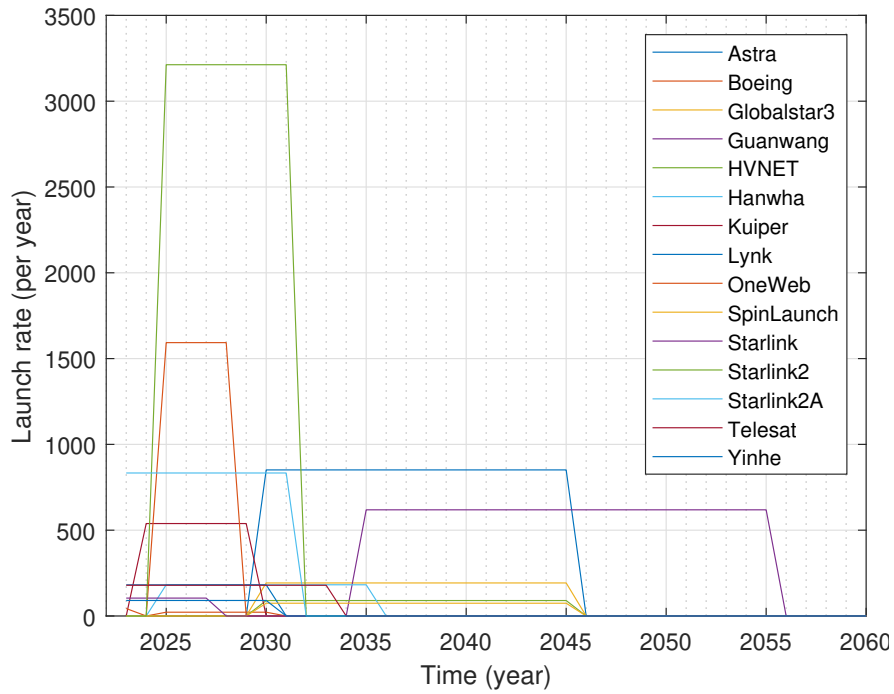
Figure A.7: Assumed future megaconstellation launch rate during ramp-up phase
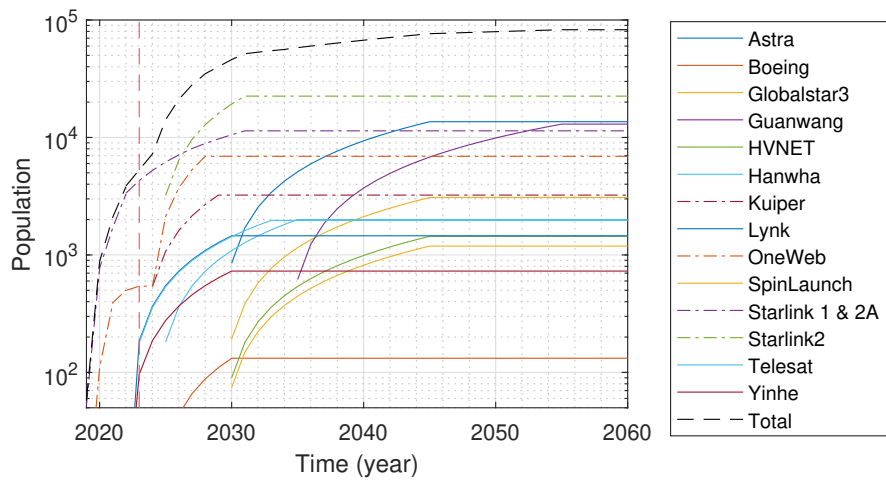


Figure A.8: Future megaconstellation launch model

116

# E Megaconstellation future traffic model results



(a) Starlink (v1, 1.5), Kuiper, OneWeb      (b) Starlink (v1, 1.5, 2), Kuiper, OneWeb
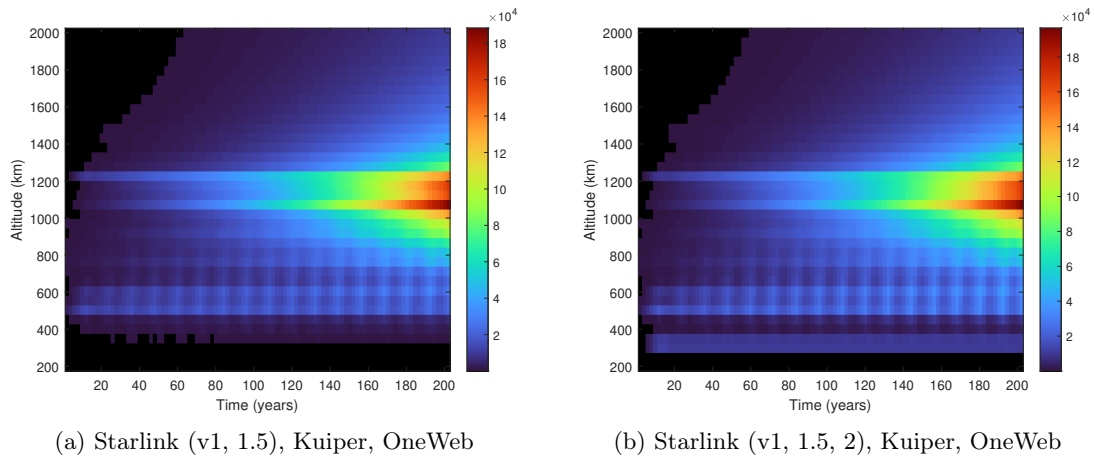
Figure A.9: Total population per altitude for future launches



(a) Population      (b) Collisions

Figure A.10: Population and collisions statistics for megaconstellation launches limited to < 600 km (total 59336 operational). Altitude bin of 50 km, time bin of 1 year.

(a) Population            (b) Collisions
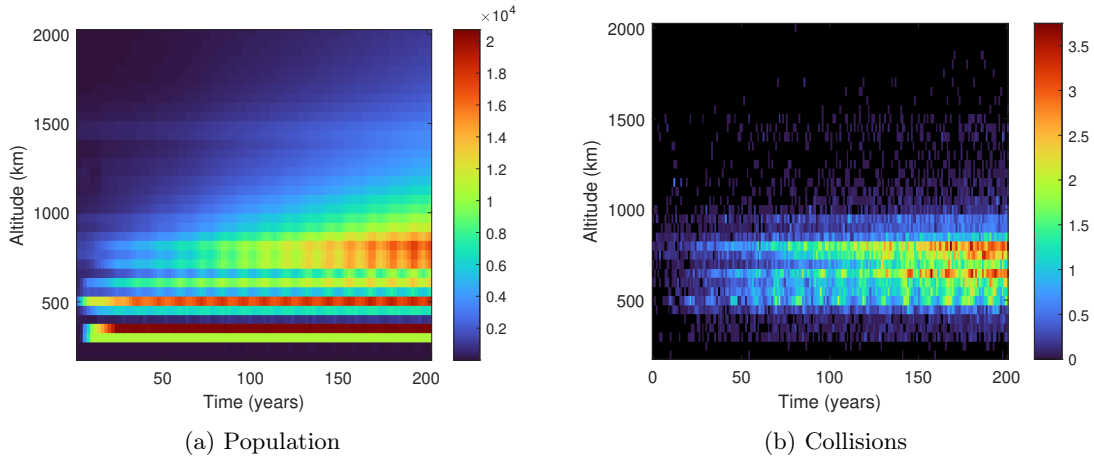
Figure A.11: Population and collisions statistics for megaconstellation launches limited to < 900 km (total 66598 operational). Altitude bin of 50 km, time bin of 1 year.



(a) < 600 km megaconstellation scenario      (b) < 900 km megaconstellation scenario
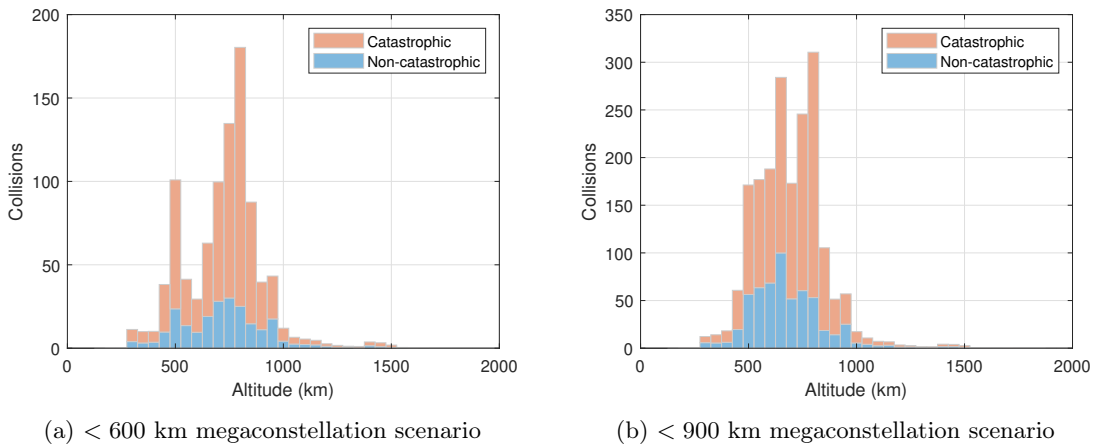
Figure A.12: Cumulative catastrophic vs non-catastrophic collisions for the altitude limited megaconstellation scenarios over a 200-year scenario. Altitude bin of 50 km.

## F  Equilibrium solution comparison

Equilibrium solutions are introduced in Sec. 4.6. An overall increase in the capacity is seen, with a higher total number of launches for MOCAT3-DV. Figures A.13 show the linear plot zoomed in to show the difference between the MOCAT3 and MOCAT3-DV solutions. Allowing for DV dynamics changes the SSEM equilibrium solution such that more debris is allowed to accumulate at the higher altitudes. At equilibrium, these populations will slowly deorbit into the lower shells where they are more quickly removed from orbit.



(a) MOCAT3
(b) MOCAT3 with DV dynamics
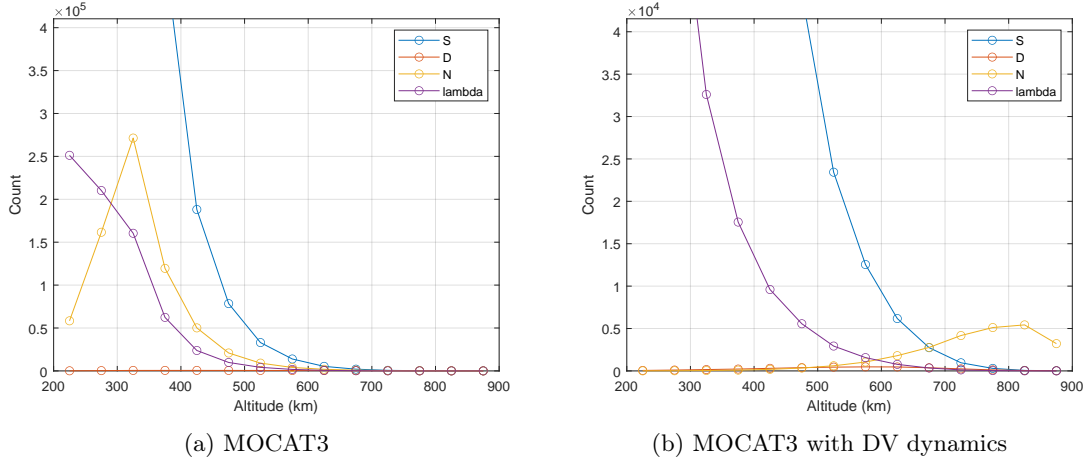
Figure A.13: Comparison of equilibrium solutions with and without Delta-V dynamics

## G  Mass conservation from SSEM debris binning

Mass conservation error and its relation to binning introduced in Sec. 4.4.3 is expanded in this section. Strictly speaking, any number of debris classes would exhibit mass conservation if the mean value of the mass is used as the representative debris class. This extends to unbinned class,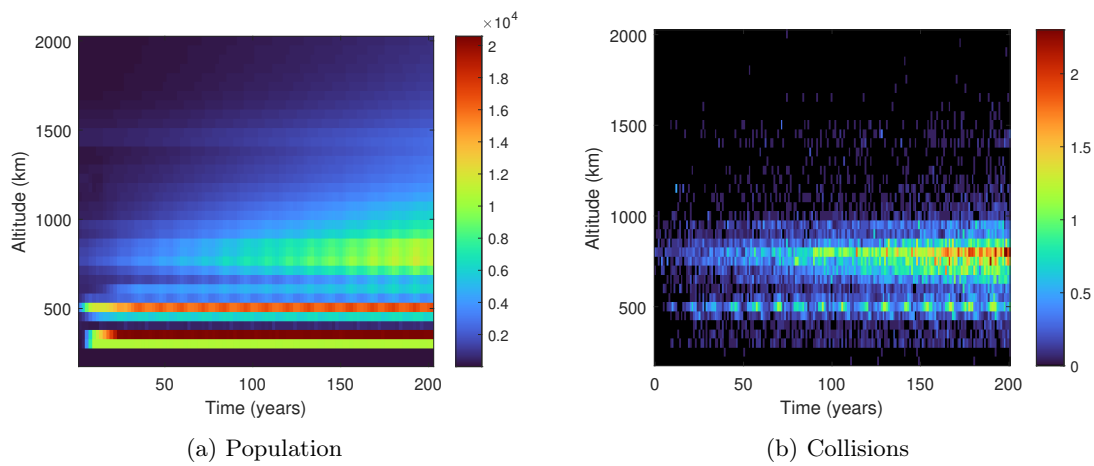 which is equivalent to binning into one class. This would mean that given a minimum $L_C$ used for the SSEM simulation, a collision between representative objects (such as payload and derelict) would produce a certain number of debris following the NASA SBM formulation. Using the mean mass value and summing the number of objects would mathematically produce the valid amount of mass produced from the colliding pair of parent objects. However, the representative mass and size would not be a realistic debris as the mean value is skewed by the power law distribution that contains more objects in the smaller regime within any size-binned debris class, as well as skew heavier due to the log-normal distribution of the AMR.

Figure A.14 shows the mass and density distribution of the resulting debris after ten catastrophic collisions between two 260 kg payloads with minimum $L_C = 10$ cm. The effect of binning is shown with the dotted red lines to show the bin edges, and the four different methods to calculate the representative mass and characteristic length for the bin using either means or medians. When the mean value is used for both the mass and length for each bin, it is often the case that the resulting definition for the binned species is too

dense. The skewness resulting from the power-law distribution shows that the mean value may not be the best representation for the debris class. Also note the increasing debris density for the smaller debris objects – this is noted in [49] as a "deficiency" in the NASA SBM that will be corrected in the future for very small objects less than 1 mm.
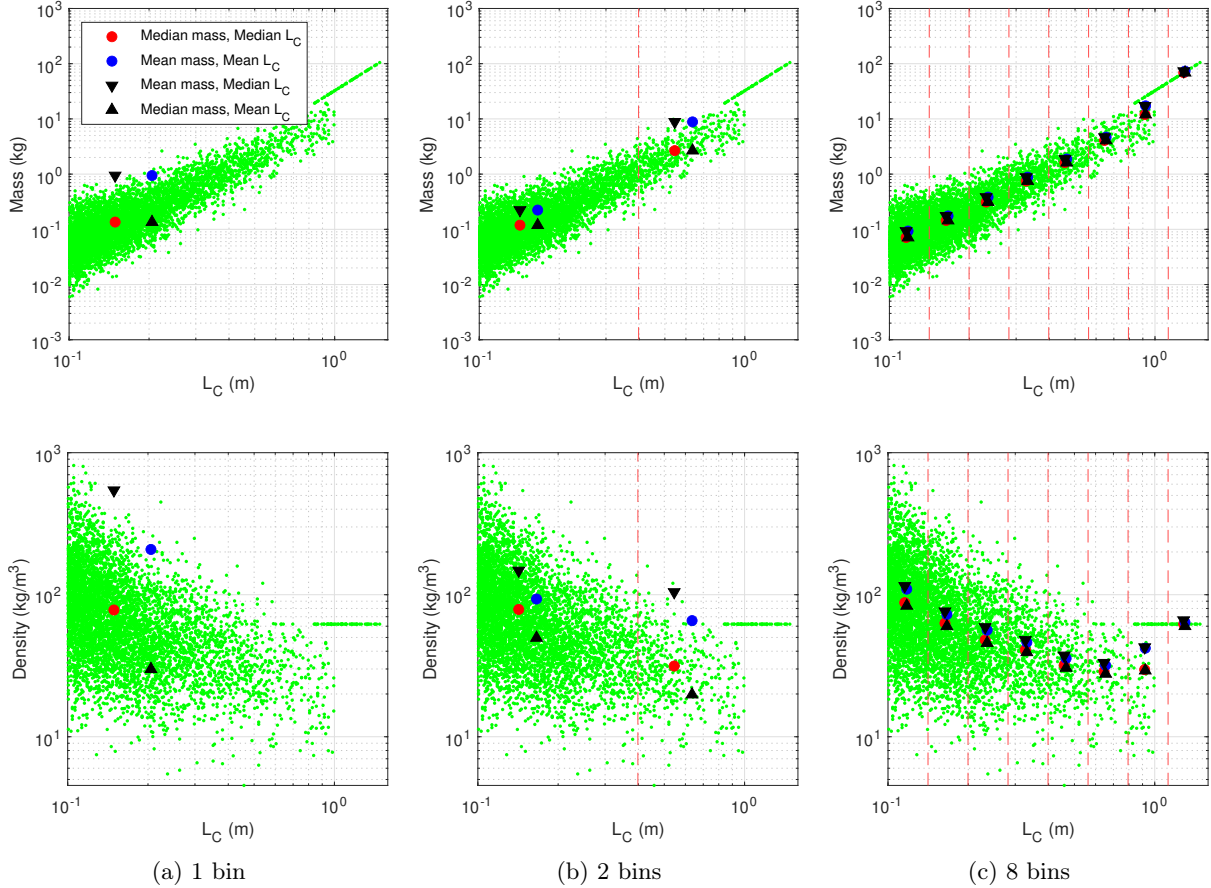


Figure A.14: Mass and density distribution for SSEM debris class binning with minimum $L_C = 10$ cm

Though the use of median values may be more representative of a typical debris within the debris species, there is a limitation to the mass-conservation property per collision, as seen from Sec. 4.4.3. This is further explored in Fig. A.15 by comparing the reduction in error as the number of bin increases. This adds a few more cases to Fig. 4-13. As expected, the mean values of mass produces no error, however, the values tend to represent debris with greater density than is seen in the debris population.

Note that the mass error shows that the total debris mass in SSEM is always less than the total mass of the parent objects. Though the smaller debris tend to be higher density, they are quite small volumetrically. Thus, the total mass contribution of the smaller objects is low. Representing any debris species will skew the mass towards the smaller objects, and thus the total mass of the SSEM debris class being less than the parent objects total mass.

A similar distribution is seen when the minimum $L_C = 1$ cm. In this case, two collisions between the

Figure A.15: Error in mass conservation from binning - 10 cm case

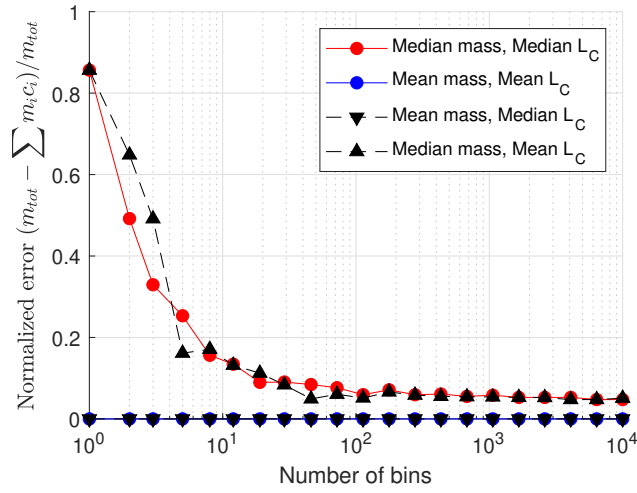same 260 kg objects are binned and shown in Figs. A.16 and A.17.
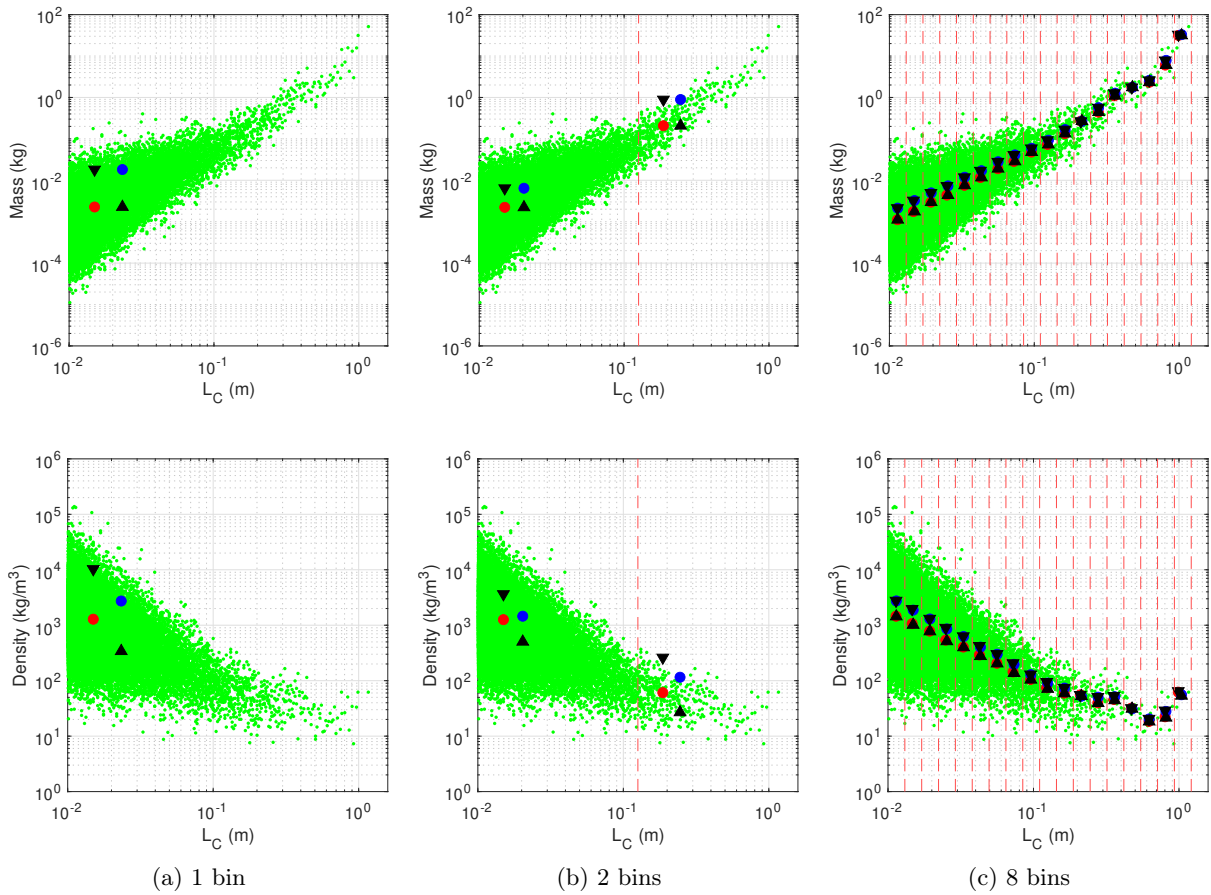


(a) 1 bin

(b) 2 bins

(c) 8 bins

Figure A.16: Mass and density distribution for SSEM debris class binning with minimum $L_C = 1$ cm
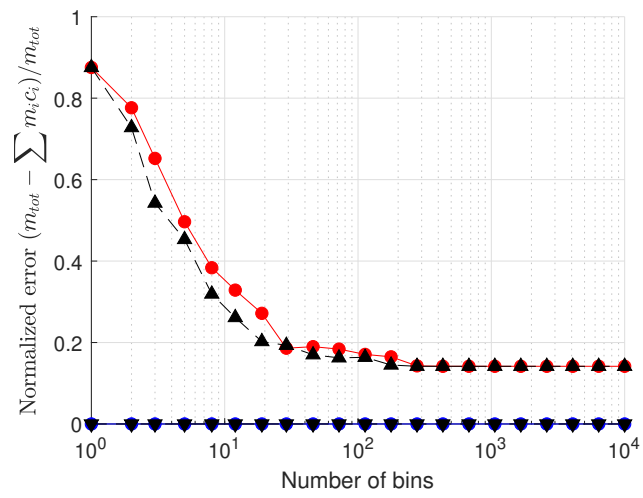
Figure A.17: Error in mass conservation from binning - 1 cm case

# H MOCAT-MC Subroutines

## NASA Standard Breakup Model Implementation

Algorithm 1 outlines the major steps involved in simulating space debris generation following a collision according to the NASA Standard Breakup Model. It involves:

- Calculation of collision specific energy to determine collision type (catastrophic or non-catastrophic).

- Generating debris pieces based on a power-law distribution, tailored to the collision type.

- Adding large fragments if necessary to ensure mass conservation.

- Assigning generated debris to the two original objects based on size and mass.

- Creating the final debris objects with specific orbital parameters.

---

**Algorithm 1** NASA Standard Breakup Model

---

1: **function** COLLISIONSBM($ep$, $p1$, $p2$, $param$, $LB$)
2:     **Ensure** $p1$ is larger than $p2$
3:     $dv \leftarrow$ CalculateRelativeVelocity($p1.velocity$, $p2.velocity$)
4:     $catastrophRatio \leftarrow$ CalculateCatastrophicRatio($p1.mass$, $p2.mass$, $dv$)
5:     **if** $catastrophRatio < 40$ **then**
6:         $M \leftarrow p2.mass \cdot dv^2$
7:         $isCatastrophic \leftarrow$ False
8:     **else**
9:         $M \leftarrow p1.mass + p2.mass$
10:         $isCatastrophic \leftarrow$ True
11:     **end if**
12:     $numDebris \leftarrow$ CalculateDebrisNumber($M$, $LB$)
13:     $debrisSizes \leftarrow$ SampleDebrisSizes($LB$, $numDebris$, $p1.radius$)
14:     $debrisMasses \leftarrow$ CalculateDebrisMasses($debrisSizes$, $p1.objectClass$)
15:     **if** Sum($debrisMasses$) $< M$ **then**
16:         **if** $isCatastrophic$ **then**
17:             AddLargeFragments($debrisSizes$, $debrisMasses$, $M$, $p1$, $p2$)
18:         **else**
19:             AddSingleLargeFragment($debrisSizes$, $debrisMasses$, $M$, $p1$)
20:         **end if**
21:     **end if**
22:     $debrisVelocities \leftarrow$ CalculateDebrisVelocities($debrisMasses$, $Am$, $dv$)
23:     $[frag1, frag2] \leftarrow$ AssignDebris($debrisSizes$, $debrisMasses$, $p1$, $p2$)
24:     ValidateMassBudget($frag1$, $frag2$, $p1$, $p2$)
25:     $[debris1, debris2] \leftarrow$ CreateDebris($frag1$, $frag2$, $p1$, $p2$)
26:     **return** $debris1$, $debris2$, $isCatastrophic$
27: **end function**

---

## Cube Method Implmentation

Algorithm 2 describes the Cube method as implemented in MOCAT-MC, from filtering out objects above the altitude limit, discretizing the 3D space into a grid of cubes, identifying which objects fall into the same

cube, and finally, if requested, creating pairs of these objects to potentially check for collisions or proximity within that cube. Cube resolution that determines the size of the cube is an input parameter denoted as *res*.

---
**Algorithm 2** Cube method
---
1: **function** DETERMINEOBJECTSINSAMECUBE($X$, *res*, *collision_alt_limit*)
2:      **for each** object in $X$ **do**
3:          **if** any position of object $>$ *collision_alt_limit* **then**
4:              Invalidate object
5:          **end if**
6:      **end for**
7:      **for each** valid object position in $X$ **do**
8:          Assign discrete cube index for each dimension by flooring the position divided by *res*
9:      **end for**
10:     Adjust all indices to be positive by adding this maximum value plus offset
11:     **for each** object's discrete position **do**
12:         Calculate a unique identifier ($X\_idx$) for the cube it occupies
13:     **end for**
14:     Find duplicated identifiers
15:     **if** duplicates exist **then**
16:         **for each** set of objects in the same cube **do**
17:             Generate pairs of indices of these objects
18:         **end for**
19:         Store these pairs as the *result*
20:     **else**
21:         Return empty set
22:     **end if**
23:     **return** *result*
24: **end function**
---

# I MOCAT-SSEM Subroutines

---

**Algorithm 3** MOCAT3 Simulation Process

---

1: **function** MOCAT3(inputs)
2:     **Define Scenario Properties**
3:     Define initial conditions, simulation parameters, and species definitions.
4:     **Generate Species Pairs**
5:     Use `generate_species_pairs` to create pairs of species for simulation interactions.
6:     For MOCAT3 specific scenarios, use `make_collision_pairs_MOCAT3`.
7:     Alternatively, for SBM models within MOCAT3, use `make_collision_pairs_SBM`.
8:     **Prepare Debris Bins**
9:     Initialize bins for tracking debris by size, altitude, and other characteristics.
10:     **For each Simulation Time Step do**
11:     **For each Pair of Species do**
12:     Determine if collision occurs based on scenario properties.
13:     **If Collision Detected then**
14:     **Calculate Collision Outcome using** `EVOLVEbinsDV`
15:     Input masses, radii, relative velocity (`dv`), and bin distributions.
16:     Determine if the collision is catastrophic.
17:     Distribute resulting debris into bins.
18:     **Calculate Drag Effects for each species at each altitude shell**
19:     Adjust bin distributions based on drag decay models.
20:     Update Scenario Properties based on outcomes.
21:     **Collect and Analyze Results**
22:     Aggregate data on debris populations, collision frequencies, and drag effects.
23:     Analyze trends in debris evolution.
24:     **End MOCAT3 Simulation**
25: **end function**

---

**Algorithm 4** MOCAT-SSEM Simulation Process

1: **Setup MOCAT-SSEM Simulation**
2: **Define Scenario Properties**
3:     Define simulation parameters (simulation length, time step, altitude shells, solver etc).
4:     Define species definitions ($S, D, N$, etc).
5: **Generate Species Pairs**
6:     **for each** pair of objects within each altitude bin **do**
7:         Calculate collision cross section probability
8:         Calculate number of debris created from SBM
9:         Calculate spreading function to deposit into neighboring shells
10:     **end for**
11: **Create ODEs**
12:     Add in launch and drag effects to ODEs
13:     Create coupled equations for each species for each altitude bin
14: **Solve systems of equations**
15:     Propagate with given input parameters such as initial population and launch rate $\lambda$
16: **Collect and Analyze Results**
17:     Aggregate evolution of debris populations, collision frequencies, and drag effects.
18:     Analyze debris evolution.
19: **End Simulation**

# Bibliography

[1] International Risk Governance Center Collision risk from space debris.

[2] Kessler, Cour-Palais - 1978 - Collision frequency of artificial satellites The creation of a debris belt.

[3] Models of the earth's upper atmosphere (CIRA-2012), 7 2012.

[4] ITU e-submission of satellite network filings - AETHER-C, 12 2021.

[5] ITU e-submission of satellite network filings - CINNAMON-937, 9 2021.

[6] Space situational awareness market size, share, trend, forecast, & industry analysis – 2022-2028. *Stratview Research*, 2023(SRAD234), 2021.

[7] Space innovation: Mitigation of orbital debris in the new space age [press release], 9 2022.

[8] Space industry statement in support of international commitments not to conduct destructive anti-satellite testing, 3 2024.

[9] L Acedo. Kinematics effects of atmospheric friction in spacecraft flybys, 2017.

[10] J. R. Alarcón Rodríguez, F. Martínez Fadrique, and H. Klinkrad. Collision Risk Assessment with a 'Smart Sieve' Method. volume 486 of *ESA Special Publication*, page 159, August 2002.

[11] David Arnas, Miles Lifson, Richard Linares, and Martín E. Avendaño. Definition of Low Earth Orbit slotting architectures using 2D lattice flower constellations. *Advances in Space Research*, 67(11):3696–3711, 6 2021.

[12] B. Bastida Virgili, J.C. Dolado, H.G. Lewis, J. Radtke, H. Krag, B. Revelin, C. Cazaux, C. Colombo, R. Crowther, and M. Metz. Risk to space sustainability from large constellations of satellites. *Acta Astronautica*, 126:154–162, 2016. Space Flight Safety.

[13] Pierre Bernhard, Marc Deschamps, and Georges Zaccour. Large satellite constellations and space debris: Exploratory analysis of strategic management of the space commons. *European Journal of Operational Research*, 4 2022.

[14] T.D. Bess. Mass distribution of orbiting man-made space debris, 12 1975.

[15] Karl D. Bilimoria and Rogier A. Krieger. Slot architecture for separating satellites in Sun-synchronous orbits. *AIAA SPACE Conference and Exposition 2011*, 2011.

[16] C. Bombardelli, E. M. Alessi, A. Rossi, and G. B. Valsecchi. Environmental effect of space debris repositioning. *Advances in Space Research*, 1(60):28–37, 7 2017.

[17] Bruce Bowman, W Kent Tobiska, Frank Marcos, Cheryl Huang, Chin Lin, and William Burke. A new empirical thermospheric density model jb2008 using new solar and geomagnetic indices. page 6438, 2008.

[18] Bruce R Bowman. True satellite ballistic coefficient determination for hasdm. *Astrodynamics Specialist Conference and Exhibit*, 8 2002.

[19] Andrew M. Bradley and Lawrence M. Wein. Space debris: Assessing risk and responsibility. *Advances in Space Research*, 43(9):1372–1390, 5 2009.

[20] Vitali Braun, Stijn Lemmens, Benedikt Reihs, Holger Krag, and Andre Horstmann. Analysis of breakup events. 04 2017.

[21] PJ Cefola, Z Folcik, R Di-Costanzo, N Bernard, S Setty, and JFS Juan. Revisiting the dsst standalone orbit propagator. *Advances in the Astronautical Sciences*, 152:2891–2914, 2014.

[22] V. A. Chobotov. Classification of orbits with regard to collision hazard in space. *Journal of Spacecraft and Rockets*, 20(5):484–490, 1983.

[23] Thomas J Colvin, John Karcz, and Grace Wusk. Cost and benefit analysis of orbital debris remediation. *NASA Office of Technology, Policy, and Strategy*, 2023.

[24] Alessandro Cordelli. The Proliferation of Orbiting Fragments: A Simple Mathematical Model. *Science & Global Security*, 2(4):365–378, 11 1991.

[25] Andrea D'Ambrosio, Miles Lifson, Daniel Jang, Celina Pasiecznik, and Richard Linares. Projected orbital demand and leo environmental capacity. *Advanced Maui Optical and Space Surveillance Technologies (AMOS) Conference*, 2022.

[26] Andrea D'Ambrosio, Miles Lifson, and Richard Linares. The capacity of low earth orbit computed using source-sink modeling. *arXiv*, 2022.

[27] Andrea D'Ambrosio, Simone Servadio, Peng Mun Siew, Daniel Jang, Miles Lifson, and Richard Linares. Analysis of the leo orbital capacity via probabilistic evolutionary model. *AAS/AIAA Astrodynamics Specialist Conference*, 8 2022.

[28] Lamberto Dell'Elce, Maarten Arnst, and Gaëtan Kerschen. Probabilistic assessment of the lifetime of low-earth-orbit spacecraft: Uncertainty characterization. *Journal of Guidance, Control, and Dynamics*, 38(5):900–912, 2015.

[29] Paul Diaz, Pol Mesalles Ripoll, Matthew Duncan, Mike Lindsay, Toby Harris, and Hugh G Lewis. Data-driven lifetime risk assessment and mitigation planning for large-scale satellite constellations. *The Journal of the Astronautical Sciences*, 70(4):21, 2023.

[30] JC Dolado-perez, Romain Di Costanzo, and Bruno Revelin. Introducing Medee-a New Orbital Debris Evolutionary Model. pages 22–25, Darmstadt, Germany, 4 2013.

[31] Jakub Drmola and Tomas Hubik. Kessler syndrome: System dynamics model. *Space Policy*, 44-45:29–39, 8 2018.

[32] Ch Durin, J. C. Mandeville, and J. M. Perrin. Active detection of micrometeoroids and space debris SODAD-2 experiment on SAC-D satellite. *Advances in Space Research*, 69(10):3856–3863, 5 2022.

[33] A. D'Ambrosio, S. Servadio, P. M. Siew, D. Jang, M. Lifson, and R. Linares. Analysis of the leo orbital capacity via probabilistic evolutionary model. 2022.

[34] ESA Space Debris Office. ESA annual space environment report, 4 2022.

[35] ESA Space Debris Office. ESA annual space environment report, 9 2023.

[36] Executive Office of the President. National space traffic management policy. *Presidential Document*, 2018-13521:28969–28976, 6 2018.

[37] FCC. Space innovation IB docket no. 22-271 mitigation of orbital debris in the new space age. Docket No: 22-271, 18-313, 12 2022.

[38] David Finkleman, Daniel L Oltrogge, Anthony Faulds, and Joseph Gerber. Analysis of the response of a space surveillance network to orbital debris events. San Diego, CA, 2008. American Astronautical Society.

[39] Emilio Frazzoli, Giovanni B. Palmerini, and Filippo Graziani. Debris cloud evolution: Mathematical modelling and application to satellite constellation design. *Acta Astronautica*, 39(6):439–445, 9 1996.

[40] Stefan Frey and Camilla Colombo. Transformation of satellite breakup distribution for probabilistic orbital collision hazard analysis. *Journal of Guidance, Control, and Dynamics*, 44:88–105, 2021.

[41] Eric R George. A high performance conjunction analysis technique for cluster and multi-core computers. *AMOS*, 2011.

[42] Adrian V. Gheorghe and Daniel E. Yuchnovicz. The space infrastructure vulnerability cadastre: Orbital debris critical loads. *International Journal of Disaster Risk Science*, 6(4):359–371, 12 2015.

[43] Houman Hakima and M Reza Emami. Assessment of active methods for removal of LEO debris. *Acta Astronautica*, 144:225–243, 2018.

[44] Doyle T. Hall. Expected Collision Rates for Tracked Satellites. *Journal of Spacecraft and Rockets*, 58(3):715–728, 1 2021.

[45] William B. Heard. Dispersion of ensembles of non-interacting particles. *Astrophysics and Space Science*, 43(1):63–82, 8 1976.

[46] Matthew D Hejduk. Satellite Conjunction Assessment Risk Analysis for "Dilution Satellite Conjunction Assessment Risk Analysis for "Dilution Region" Events: Issues and Operational Approaches Region" Events: Issues and Operational Approaches. 2 2019.

[47] G.A. Henning, M.E. Sorge, G.E. Peterson, A.B. Jenkin, D. Mains, and J.P. McVey. Parameterizing large constellation post-mission disposal success to predict the impact to future space environment. *Journal of Space Safety Engineering*, 7(3):171–177, 2020. Space Debris: The State of Art.

[48] Caleb Henry. Spacex submits paperwork for 30,000 more starlink satellites. *Space News*, 15:2019, 2019.

[49] André Horstmann, Sebastian Hesselbach, Carsten Wiedemann, Sven Flegel, Michael Oswald, and Holger Krag. Enhancement of S/C fragmentation and environment evolution models. *European Space Agency*, 8 2020.

[50] D. Jang, A. D'Ambrosio, M. Lifson, C. Pasiecznik, and R. Linares. Stability of the leo environment as a dynamical system. 2022.

[51] Daniel Jang and Richard Linares. System-Level Risk Assessment of the Low Earth Orbit Environment. Austin, TX, 3 2022.

[52] JASON report. The Impacts of Large Constellations of Satellites. 2020.

[53] JFSCC. Launch Conjunction Assessment Handbook - 18 SPCS Process for Launch Conjunction Assessment.

[54] Christopher D. Johnson. Handbook for new actors in space, 2017.

[55] N. L. Johnson, P. H. Krisko, J. C. Liou, and P. D. Anz-Meador. NASA's new breakup model of evolve 4.0. *Advances in Space Research*, 28:1377–1384, 1 2001.

[56] Christopher Kebschull, Jonas Radtke, and Holger Krag. Deriving a priority list based on the environmental criticality. 2014.

[57] Christopher Kebschull, Philipp Scheidemann, Sebastian Hesselbach, Jonas Radtke, Vitali Braun, H. Krag, and Enrico Stoll. Simulation of the space debris environment in LEO using a simplified approach. *Advances in Space Research*, 59(1):166–180, 1 2017.

[58] T S Kelso. Analysis of the Iridium 33-Cosmos 2251 Collision. 2009.

[59] Donald J Kessler and Phillip D Anz-Meador. Critical Number of Spacecraft in Low Earth Orbit: Using Satellite Fragmentation Data to Evaluate the Stability of the Orbital Debris Environment. 2001.

[60] Donald J. Kessler and Burton G. Cour-Palais. Collision frequency of artificial satellites: The creation of a debris belt. *J Geophys Res*, 83:2637–2646, 1978.

[61] Donald J Kessler, Nicholas L Johnson, J.-C Liou, and Mark Matney. The Kessler Syndrome: Implications to Future Space operations. *33rd Annual Aas Guidance and Control Conference*, 2010.

[62] H. Klinkrad. DISCOS - ESA's database and information system characterising objects in space. *Advances in Space Research*, 11(12):43–52, 1 1991.

[63] H Klinkrad. *Space Debris: Models and Risk Analysis*. Springer Berlin Heidelberg, 2006.

[64] Holger Krag, Stijn Lemmens, and F Letizia. Space traffic management through the control of the space environment's capacity. *5th European Workshop on Space Debris Modeling and Remediation*, 2018.

[65] Clement G. Lee, Martin A. Slade, Joseph S. Jao, and Nereida Rodriguez-Alvarez. Micro-meteoroid and orbital debris radar from goldstone radar observations. *Journal of Space Safety Engineering*, 7(3):242–248, 2020. Space Debris: The State of Art.

[66] Francesca Letizia. Extension of the density approach for debris cloud propagation. *Journal of Guidance, Control, and Dynamics*, 41(12):2650–2656, 9 2018.

[67] Francesca Letizia, Camilla Colombo, Hugh Lewis, and Holger Krag. Extending the ECOB space debris index with fragmentation risk estimation. *European Space Agency (ESA)*, 4 2017.

[68] Francesca Letizia, Camilla Colombo, and Hugh G. Lewis. Analytical model for the propagation of small-debris-object clouds after fragmentations. *Journal of Guidance, Control, and Dynamics*, 38(8):1478–1491, 3 2015.

[69] Francesca Letizia, Camilla Colombo, Hugh G. Lewis, and Holger Krag. Assessment of breakup severity on operational satellites. *Advances in Space Research*, 58(7):1255–1274, 10 2016.

[70] Francesca Letizia, Camilla Colombo, Hugh G. Lewis, and Holger Krag. Development of a Debris Index. *Astrophysics and Space Science Proceedings*, 52:191–206, 2018.

[71] Francesca Letizia, Stijn Lemmens, Benjamin Bastida Virgili, and Holger Krag. Application of a debris index for global evaluation of mitigation strategies. *Acta Astronautica*, 161:348–362, 2019.

[72] Francesca Letizia, Stijn Lemmens, and Holger Krag. Environment capacity as an early mission design driver. *Acta Astronautica*, 173:320–332, 2020.

[73] Francesca Letizia, Stijn Lemmens, Danielle Wood, Minoo Rathnasabapathy, Miles Lifson, Riley Stiendl, Moriba Jah, Nikolai Khlystov, and Maksim Soshkin. Contribution from SSA data to the definition of a Space Sustainability Rating. 2020.

[74] H. G. Lewis, J Radtke, A Rossi, J Beck, M Oswald, P Anderson, B Bastida Virgili, and H Krag. Sensitivity of the Space Debris Environment to Large Constellations and Small Satellites. *7th European Conference on Space Debris*, 2017.

[75] H. G. Lewis, G. G. Swinerd, R. J. Newland, and A. Saunders. The fast debris evolution model. *Advances in Space Research*, 44:568–578, 9 2009.

[76] Hugh Lewis, Graham Swinerd, Niel Williams, and Gavin Gittins. Damage: a dedicated geo debris model framework. *3rd European Conference on Space Debris*, pages 373–378, 3 2001.

[77] Hugh G Lewis. Understanding long-term orbital debris population dynamics. *First Int'l. Orbital Debris Conf.*, 2019.

[78] Hugh G Lewis, Samuel Diserens, Timothy Maclay, and J P Sheehan. Limitations of the cube method for assessing large constellations. *First International Orbital Debris Conference*, 2019.

[79] Hugh G. Lewis and Nathan Marsh. Deep Time Analysis of Space Debris and Space Sustainability. page 153, April 2021.

[80] Hugh G. Lewis, Arrun Saunders, Graham Swinerd, and Rebecca J. Newland. Effect of thermospheric contraction on remediation of the near-earth space debris environment. *Journal of Geophysical Research: Space Physics*, 116, 2011.

[81] Hugh G Lewis, Graham G Swinerd, Rebecca J Newland, and Arrun Saunders. Active Removal Study for On-Orbit Debris Using DAMAGE. 2009.

[82] Hugh G Lewis, Emily Wymer, and Tara Landmark. The Use of Stress Tests to Evaluate Space Debris Mitigation Measures. pages 20–23, 2021.

[83] M. Lifson, D. Jang, C. Pasiecznik, and R. Linares. MOCAT-SSEM: A source-sink evolutionary model for space debris environment evolutionary modeling. *9th Annual Space Traffic Management Conference*, 2023.

[84] Miles Lifson, David Arnas, Martin Avendaño, and Richard Linares. A Method for Generating Closely Packed Orbital Shells and the Implication on Orbital Capacity. *AIAA Scitech 2023 Forum*, 2022.

[85] Miles Lifson, Andrea D'Ambrosio, David Arnas, and Richard Linares. How many satellites can we fit in low earth orbit?: Capacity integrating risk-based and intrinsic methods. *AAS/AIAA Astrodynamics Specialist Conference*, 2022.

[86] Miles Lifson, Daniel Jang, and Richard Linares. Space Environmental Governance and Decision Support using Source-Sink Evolutionary Environmental Models. Maui, HI, 2023. Maui Economic Development Board.

[87] J. C. Liou. Collision activities in the future orbital debris environment. *Advances in Space Research*, 38:2102–2106, 2006.

[88] J. C. Liou. An active debris removal parametric study for LEO environment remediation. *Advances in Space Research*, 47(11):1865–1876, 6 2011.

[89] J. C. Liou, D. T. Hall, P. H. Krisko, and J. N. Opiela. LEGEND – a three-dimensional LEO-to-GEO debris evolutionary model. *Advances in Space Research*, 34:981–986, 1 2004.

[90] J. C. Liou, N. L. Johnson, and N. M. Hill. Controlling the growth of future LEO debris populations with active debris removal. *Acta Astronautica*, 66(5-6):648–653, 3 2010.

[91] J.-C Liou and Nicholas Johnson. A leo satellite postmission disposal study using legend. *Acta Astronautica*, 57:324–329, 07 2005.

[92] J. C. Liou, Don J Kessler, Mark Matney, and Gene Stansbery. A new approach to evaluate collision probabilities among asteroids, comets, and kuiper belt objects. *Lunar and Planetary Science XXXIV*, 2003.

[93] J.-C. Liou and P. Krisko. An Update on the Effectiveness of Postmission Disposal in LEO. 2013.

[94] J.C. Liou, Ak Anilkumar, B Bastida Virgili, T Hanada, H Krag, H Lewis, MXJ Raj, MM Rao, A Rossi, and RK Sharma. Stability of the future leo environment - an iadc comparison study. *Proc. 6th European Conference on Space Debris*, 2013.

[95] Alfred J Lotka. Analytical note on certain rhythmic relations in organic systems. *Proceedings of the National Academy of Sciences*, 6(7):410–415, 1920.

[96] Arthur Lue. The all-versus-all low earth orbit conjunction problem. *AMOS*, 2011.

[97] Ya zhong Luo and Zhen Yang. A review of uncertainty propagation in orbital mechanics. *Progress in Aerospace Sciences*, 89:23–39, 2 2017.

[98] M. Madi and O. Sokolova. *Space Debris Peril: Pathways to Opportunities*. CRC Press, 2021.

[99] A. Manis, M. Matney, A. Vavrin, J. H. Seago, D. Gates, P. Anz-Meador, T. Kennedy, Cowardin Heather, and Y. L. Xu. NASA Orbital Debris Engineering Model (ORDEM) 3.1 Model Process. NASA Technical Publication, April 2022.

[100] C E Martin, J E Cheese, and H Klinkrad. Space debris environment analysis with DELTA 2.0. *55th International Astronautical Congress*, 2012.

[101] Vladimir Martinusi, Lamberto Dell'Elce, and Gaëtan Kerschen. Analytic propagation of near-circular satellite orbits in the atmosphere of an oblate planet. *Celestial Mechanics and Dynamical Astronomy*, 123:85–103, 9 2015.

[102] M. Matney, A. Manis, P. Anz-Meador, D. Gates, J. H. Seago, A. Vavrin, and Y. L. Xu. The NASA Orbital Debris Engineering Model 3.1: Development, Verification, and Validation. volume 2109 of *LPI Contributions*, page 6134, December 2019.

[103] J. A.M. McDonnell, S. P. Deshpande, D. H. Niblett, M. J. Neish, and P. J. Newman. The near Earth space impact environment — An LDEF overview. *Advances in Space Research*, 13(8):87–101, 8 1993.

[104] Joanathan McDowell. Jonathan McDowell on Twitter: "Time for a look at the OneWeb constellation, which now has 396 satellites in orbit. https://t.co/UyGPPet3Pd" / Twitter, 1 2022.

[105] Jonathan McDowell. Jonathan McDowell on Twitter: "Recent Starlink launches are using plane-drift to share sats from a launch among even more orbit planes. This also increases the amount of time sats spend in orbit raising. Here is the launch from Feb 4, with 23% of sats still not at final altitude after over 4 months https://t.co/XdrZbboB3E" / Twitter, 6 2021.

[106] Jonathan McDowell. *Jonathan's Space Report*. Jonathan McDowell, 2023.

[107] Darren McKnight and Gary Lorenzen. Collision matrix for low earth orbit satellites. *Journal of Spacecraft and Rockets*, 26(2):90–94, 1989.

[108] Darren McKnight, Rachel Witner, Francesca Letizia, Stijn Lemmens, Luciano Anselmo, Carmen Pardini, Alessandro Rossi, Chris Kunstadter, Satomi Kawamoto, Vladimir Aslanov, Juan Carlos Dolado Perez, Vincent Ruch, Hugh Lewis, Mike Nicolls, Liu Jing, Shen Dan, Wang Dongfang, Andrey Baranov, and Dmitriy Grishko. Identifying the 50 statistically-most-concerning derelict objects in LEO. *Acta Astronautica*, 181:282–291, 4 2021.

[109] Lieutenant Colonel Daniel Moomey, Rachael Falcon, and Arbab Khan. Trending and analysis of payload vs. all low earth conjunction data messages below 1000 km, from 2016 through 2021. *Journal of Space Safety Engineering*, 10(2):217–230, 2023.

[110] James Murray and Timothy Kennedy. Haystack ultra-wideband satellite imaging radar measurements of the orbital debris environment: 2020, 2022.

[111] San Luis Obispo and Connor D Noyes. Characterization of the Effects of a Sun-Synchronous Orbit Slot Architecture on the Earth's Orbital Debris Environment. *Master's Theses*, 6 2013.

[112] Carmen Pardini and Luciano Anselmo. Characterization of abandoned rocket body families for active removal. *Acta Astronautica*, 126:243–257, 9 2016.

[113] Carmen Pardini and Luciano Anselmo. Evaluating the environmental criticality of massive objects in LEO for debris mitigation and remediation. *Acta Astronautica*, 145:51–75, 4 2018.

[114] Celina Pasiecznik, Andrea D'ambrosio, Daniel Jang, and Richard Linares. A dynamical systems analysis of the effects of the launch rate distribution on the stability of a source-sink orbital debris model. *International Astronautical Congress*, 2022.

[115] Tereza Pultarova. SpaceX Starlink satellites had to make 25,000 collision-avoidance maneuvers in just 6 months — and it will only get worse. `https://www.space.com/starlink-satellite-conjunction-increase-threatens-space-sustainability`, 2023. Accessed: 2023-07-07.

[116] Jonas Radtke, Sven Mueller, Volker Schaus, and Enrico Stoll. LUCA2 - An enhanced long-term utility for collision analysis | ESA Proceedings Database. 2017.

[117] Akhil Rao and Francesca Letizia. An Integrated Debris Environment Assessment Model.

[118] Akhil Rao, Mark Moretto, Marcus Holzinger, Daniel Kaffine, and Brian Weeden. Opus: An integrated assessment model for satellites and orbital debris, 2023.

[119] Akhil Rao, Giacomo Rondina, Dan Kaffine, Jon Hughes, Martin Boileau, Miles Kimball, Alessandro Peri, Matt Burgess, Sami Dakhlia, Sébastien Rouillon, Martin Abel, David Munro, and Derek Lemoine. Open access to orbit and runaway space debris growth. 2022.

[120] Albert Reuther, Jeremy Kepner, Chansup Byun, Siddharth Samsi, William Arcand, David Bestor, Bill Bergeron, Vijay Gadepally, Michael Houle, Matthew Hubbell, Michael Jones, Anna Klein, Lauren Milechin, Julia Mullen, Andrew Prout, Antonio Rosa, Charles Yee, and Peter Michaleas. Interactive Supercomputing on 40,000 Cores for Machine Learning and Data Analysis. *2018 IEEE High Performance Extreme Computing Conference, HPEC 2018*, 11 2018.

[121] Aaron J. Rosengren, Despoina K. Skoulidou, Kleomenis Tsiganis, and George Voyatzis. Dynamical cartography of earth satellite orbits. *Advances in Space Research*, 63:443–460, 1 2019.

[122] A. Rossi, H. Lewis, A. White, L. Anselmo, C. Pardini, H. Krag, and B. Bastida Virgili. Analysis of the consequences of fragmentations in low and geostationary orbits. *Advances in Space Research*, 57(8):1652–1663, 4 2016.

[123] A. Rossi, G. B. Valsecchi, and E. M. Alessi. The criticality of spacecraft index. *Advances in Space Research*, 56:449–460, 8 2015.

[124] Sébastien Rouillon. A Physico-Economic Model of Low Earth Orbit Management. *Environmental and Resource Economics*, 77(4):695–723, 12 2020.

[125] V Ruch, R Serra, P Omaly, and J C Dolado Perez. Decoupled Analysis of the Effect of Past and Future Space Activity on the Orbital Environment. *8th European Conference on Space Debris*, pages 20–23, 2021.

[126] Simone Servadio, Daniel Jang, and Richard Linares. Threat level estimation from possible break-up events in leo. page 1065, 2024.

[127] Simone Servadio, Nihal Simha, Davide Gusmini, Daniel Jang, Theodore St. Francis, Andrea D'Ambrosio, Giovanni Lavezzi, and Richard Linares. Risk index for the optimal ranking of active debris removal targets. *Journal of Spacecraft and Rockets*, 0(0):1–14, 0.

[128] G L Somma, Colombo C, and Lewis H G. A Statistical LEO Model to Investigate Adaptable Debris Control Strategies.

[129] Gian Luigi Somma. Adaptive remediation of the space debris environment using feedback control, 7 2019.

[130] Marlon E. Sorge and Deanna L. Mains. Impact fragmentation model improvements. *AIAA/AAS Astrodynamics Specialist Conference*, 8 2014.

[131] Space Safety Coalition. Best practices for the sustainability of space operations, 9 2019.

[132] SpaceX. Updates, 2 2022.

[133] SpaceX, OneWeb, and Iridium. Satellite orbital safety best practices, 9 2022.

[134] Gene Stansbery, Mark Matney, J C Liou, and Dave Whitlock. A Comparison of Catastrophic On-Orbit Collisions. 2008.

[135] S. Y. Su and D. J. Kessler. Contribution of explosion and future collision fragments to the orbital debris environment. *Advances in Space Research*, 5(2):25–34, 1985.

[136] David Talent. Analytical model for orbital debris environmental management. 4 1990.

[137] David L. Talent. Analytic model for orbital debris environmental management. *Journal of Spacecraft and Rockets*, 29:508–513, 1992.

[138] David L Talent. An assessment of the impact of the january 2007 chinese asat test on the leo environment. 9 2007.

[139] W Kent Tobiska, B Bowman, and S Dave Bouwer. Solar and geomagnetic indices for the jb2008 thermosphere density model. *Contract*, 19628(03-C):0076, 2008.

[140] Valeria Trozzi, Camilla Colombo, and Mirko Trisolini. Analysis of possible definitions of the space environment capacity to pursue long-term sustainability of space activities. *72 nd International Astronautical Congress (IAC)*, pages 25–29, 2021.

[141] United Nations. Destructive direct-ascent anti-satellite missile testing : resolution / adopted by the general assembly, 12 2022.

[142] David Vallado, Paul Crawford, Ricahrd Hujsak, and T.S. Kelso. Revisiting spacetrack report #3. *AIAA/AAS Astrodynamics Specialist Conference and Exhibit*, 2006.

[143] David A. Vallado. *Fundamentals of Astrodynamics and Applications*. Microcosm Press, 5 edition, 7 2022.

[144] B Bastida Virgili. Delta (debris environment long-term analysis). *6th International Conference on Astrodynamics Tools and Techniques (ICATT)*, 2016.

[145] Vito Volterra. Fluctuations in the abundance of a species considered mathematically. *Nature*, 118(2972):558–560, 1926.

[146] Xiao Wei Wang and Jing Liu. An introduction to a new space debris evolution model: Solem. *Advances in Astronomy*, 2019, 2019.

[147] B. Weeden and K. Shortt. Development of an architecture of sun-synchronous orbital slots to minimize conjunctions. *SpaceOps 2008 Conference*, 2008.

[148] Brian Weeden. 2009 iridium-cosmos collision fact sheet, 2010.

[149] Brian Weeden. Anti-satellite Tests in Space— The Case of China. 2013.

[150] Adam E. White and Hugh G. Lewis. An adaptive strategy for active debris removal. *Advances in Space Research*, 53(8):1195–1206, 4 2014.

[151] Adam E. White and Hugh G. Lewis. The many futures of active debris removal. *Acta Astronautica*, 95(1):189–197, 2 2014.